THE DESIGN OF A PHASED ARRAY MICROSTRIP ANTENNA FOR USE ON A REMOTELY PILOTED VEHICLE

by

© **Thomas Edward Ollevier**

A Thesis
Submitted to the Faculty of Graduate Studies
In Partial Fulfillment of the Requirements
For the Degree of Master of Science

University of Manitoba
Department of Electrical Engineering
Winnipeg, Manitoba
Canada

October 1988

ISBN 0-315-47831-4

THE DESIGN OF A PHASED ARRAY MICROSTRIP ANTENNA FOR USE ON A REMOTELY PILOTED VEHICLE

by

THOMAS EDWARD OLLEVIER

A thesis submitted to the Faculty of Graduate Studies of the University of Manitoba in partial fulfillment of the requirements of the degree of

MASTER OF SCIENCE

Abstract

The design of a microstrip array antenna is examined from analytical and experimental viewpoints.

The behavior of individual circular patch microstrip elements is analyzed with respect to radiation pattern and input impedance. The elements are arranged in three different array configurations whose performances are presented. The first configuration is a 2×8 array constructed from elements operating in the TM_{11} mode. This configuration is used as a baseline with which the performance of the other two configurations are compared. The second configuration is a 2×10 array constructed from TM_{11} mode elements. The third configuration is a 2×8 array constructed from hybrid elements operating in both the TM_{11} and TM_{21} modes. The hybrid element was utilized to investigate the feasibility of lowering the sidelobes of the array at high scan angles from broadside.

Several of the hybrid elements were constructed and tested both individually and in an array of 3 elements. The experimental measurements agreed well with the theoretical results.

Acknowledgements

I would like to express my appreciation to Dr. L. Shafai and Prof. E. Bridges for their guidance during my studies and during the preparation of this thesis.

I would also like to thank Brad Tabachnik for his advice on setting up instrumentation for the experimental measurements and for assistance in recording the patterns of the test elements in the anechoic chamber.

Lastly I would like to thank the Government of Canada for providing the financial support and time necessary to complete this project.

Contents

List of Figures

List of Tables

Chapter 1

Introduction

1.1 Background

Remotely piloted vehicles (RPVs) are unmanned aircraft that are controlled from a remote location, and which carry a payload into areas which it would not be safe or economical to do so otherwise. The military uses RPVs to carry out missions where the risks of using a manned aircraft are unacceptable or to augment the capabilities of manned aircraft. RPVs have been used as decoys [1], and deliberate targets to nullify enemy surface to air missile systems and to acquire data on the performance of new anti-aircraft systems. RPVs have also been used as platforms for jammers, data link relay equipment, and surveillance sensors. Some examples of surveillance sensors are video cameras, forward looking infrared cameras, and synthetic aperture radars. RPVs also have potential civilian uses such as border patrol, forest fire detection, mineral exploration, mapping, and as platforms for remote data relays.

The military expenditures on RPVs are estimated to be 12.5 billion dollars US [2] for the 10 year period from 1984-94. The RPV airframes cost on the order of $40,000 while the mission payload can cost from 500,000 to 2 million dollars. It is imperative that reliable communications be maintained with

these vehicles. The vehicles require dependable secure downlinks to transmit payload data and vehicle status data. RPVs require compact medium to high gain antennas to transmit this information. These antennas may be complex and relatively expensive if necessitated by operational demands.

Less sophisticated antenna designs are required during the development of RPV control systems and payloads. These antennas have to provide the gain required to obtain reliable payload data but compromises can be made in their electrical performance, such as allowing higher sidelobe levels. Compromises can also be made in the mechanical specifications of the antenna such as ruggedness, size and weight. The antenna described in this thesis is designed to be used during the design stage of an RPV video sensor payload. The basic design of the antenna could be refined such that the antenna could be used in a hostile environment, however those modifications have not been considered here. The antenna considered here consists of circular microstrip patch antennas arranged in an electronically steered array to obtain a lightweight conformal antenna.

1.2 Microstrip Antennas

In a paper presenting an overview of microstrip antenna technology Carver and Mink [3] presented the following history of the theoretical and experimental research which had been carried out in the area of microstrip antenna design. The paper covered the period from the middle 1950's to 1981, starting with the work done by Deschamps[4] and Gutton and Baissinot[5] on radiation from microstrip discontinuities. From that time until the early 1970's work in the area was not widely published. Munson[6] patented a microstrip antenna in 1973 and published a paper on conformal microstrip antennas and arrays[7] in 1974. Munson's work in developing conformal antennas for use on rockets and missiles demonstrated the feasibility of utilizing microstrip antennas on

aerial vehicles. Since the early 1970's many papers on microstrip antennas have appeared in the literature.

Microstrip antennas are ideally suited for use on aerial vehicles due to their low profile and the possibility of making them conformal. Numerous papers have been published on the use of microstrip antennas as elements in arrays. Sanford [8] demonstrated the feasibility of using an L-band microstrip phased array on an aircraft for aircraft to satellite communications. Yee and Furlong [9] designed and fabricated a lightweight fuselage integrated phased array for an RPV. Microstrip antennas have been utilized as elements for the SEASAT and SIR-A satellite arrays [10]. A number of papers have also been written on the use of microstrip elements in arrays for use with the MSAT communication system [11] [12].

Microstrip antennas fall into three main categories; patch antennas, travelling wave antennas and microstrip slot antennas [13]. The microstrip element chosen for use in this project is a microstrip patch antenna. A microstrip patch antenna consists of a patch of conducting material separated from a ground plane by a sheet of dielectric as shown in Figure 1.1. The patches can be of any shape however regular geometric shapes are preferred due to the difficulty of analyzing or predicting the performance of arbitrarily shaped patches. Typical microstrip antenna patches are circular, rectangular, elliptical, or annular in shape. The antennas are usually fabricated on a special microstrip laminate which has a uniform dielectric constant and a low loss tangent. Some typical microstrip laminate materials are alumina and PTFE (Polytetrafluoroethylene). The substrate material is copper clad and can be processed by using standard printed circuit board techniques. This keeps fabrication costs down while at the same time a consistent product is produced.

Microstrip antennas are lightweight and relatively thin compared to many other types of antennas. They can be integrated into an aerial vehicle in such

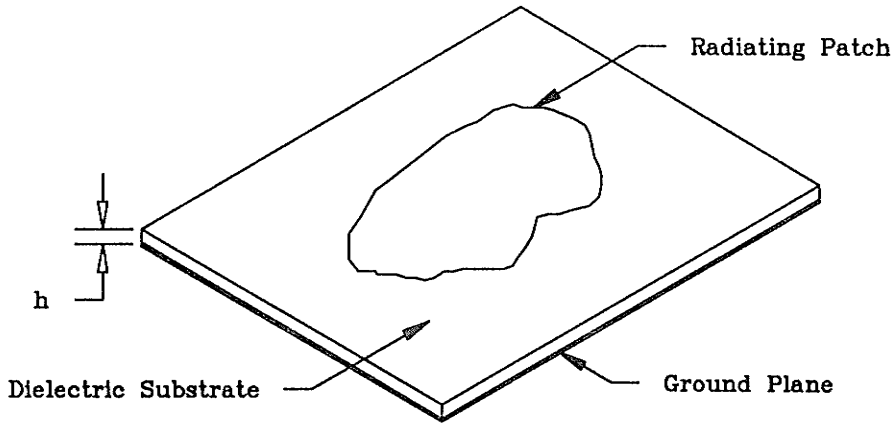

Figure 1.1: Simple Microstrip Patch Antenna

a manner that the aerodynamics of the vehicle are relatively undisturbed. Microstrip antennas can provide linear or circular polarizations by proper choice of feed locations. Because of their planar nature feed lines and discrete microstrip components can be integrated into the design of the backplane of the antenna. In this manner a complete array with all of its associated control electronics can be built in a single low profile antenna unit.

Microstrip antennas also have disadvantages, with their low bandwidth being one of the areas of concern. Microstrip antennas are inherently low bandwidth devices with bandwidths of only a few percent in their simplest form. The antennas typically radiate into a hemisphere so that a number of elements are required to obtain 360 degree coverage. As the gain required from the antenna increases the losses also increase due to the added feed lines, power splitters and other discrete microwave components. The performance of the antenna tends to be less than optimal in the endfire directions thus limiting the usefulness of the antenna in some applications.

1.3 Scope of Thesis

Chapter 2 presents a review of some of the different types of antennas which have been utilized on RPVs. The performance specifications of an antenna used on an RPV for a video downlink antenna are then presented.

Chapter 3 consists of a detailed analysis of circular patch microstrip antennas. Microstrip elements operating in the TM_{11}, TM_{21}, or combined $TM_{11} + TM_{21}$ modes are examined. Equations are derived describing the radiation patterns of elements radiating either linear or circularly polarized waves. Equations are also presented describing the polarization and directivity of the resulting microstrip antennas.

Chapter 4 contains background material on array theory and mutual impedance effects on elements in an array. Three array configurations are described and theoretical performance data is presented. The feed networks required by the various configurations are described along with the theory required to control the steering of the arrays.

Chapter 5 contains descriptions of the elements that were designed and constructed to experimentally verify the operation of the dual mode $TM_{11} + TM_{21}$ microstrip elements. The radiation patterns of the individual elements and an array consisting of three elements are presented.

Chapter 6 consists of conclusions based on the work presented in the earlier chapters of the thesis and contains proposals for further work to be undertaken to improve the construction and performance of the arrays presented.

Chapter 2

RPV Antenna Requirements

2.1 Literature Survey

RPVs require antennas for use in transmitting and receiving widely diverse types of data. The antennas may be utilized to transmit and receive communications data ranging from narrow band telemetry and command and control data to wideband spread spectrum signals. RPV sensors such as synthetic aperture radars (SAR) or electronic support measures (ESM) receivers may utilize antennas to acquire data for processing. In other operational roles antennas may also be used to transmit jamming signals over large bandwidths.

The antenna examined in this thesis is used to transmit the output of a video sensor from an RPV to the ground control station. The antenna is designed for use in a research and development environment and as such does not have to meet many of the stringent electrical and mechanical specifications of an operational antenna. The bandwidth of the antenna can be substantially narrower than that of an operational antenna that would possibly have to handle spread spectrum encoded data. The sidelobes can be higher than would be desirable in an operational environment where jamming and interception of the downlink data were of concern.

Many types of antennas have been considered for use on RPVs, in a study by Foster and Williams [14] approximately twenty different antenna configurations were detailed. The antennas examined included the following types:

- monopole
- notch
- slot
- printed dipole
- printed patch
- cavity backed spiral
- helix
- polyrod
- horns
- reflectors
- arrays
- travelling wave
- and lens antennas.

Low gain antennas have the advantage of having radiation patterns which are close to omnidirectional. Low gain antennas are suitable only for short range use as the transmitters on board an RPV are limited in their output power. The single element medium to high gain antennas have relatively small beamwidths when compared to the low gain antennas. In order to use these antennas they must be mounted on the vehicle in such a fashion that they can

be mechanically steered to point at the ground control station. This makes these antennas bulky and unaerodynamic. This type of antenna is better suited for use as a sensor antenna on an RPV such as part of an airborne radar system where the operational requirements dictate their use. Array antennas have relatively high gain and have the capability of being steered electronically. The arrays can be steered by using phase shifters or frequency sensitive feed networks. Phase shifters utilizing PIN diodes introduce losses in the feed system which reduce the efficiency of the antenna system. Frequency scanned arrays are less complex electrically but the transmit and receive electronics have to be more complex to cope with the data signal. The data signal has to dynamically change in frequency to compensate for fluctuations in the antenna steering angle caused by changes in vehicle attitude.

An operational RPV video link antenna should meet the specifications shown in Table 2.1. For the purpose of this thesis a less demanding set of requirements has been utilized. The antenna under consideration in this thesis is designed to be used in a research and development environment where the antenna performance is of secondary importance to the control of the RPV and the performance of the sensor package. In this environment the antenna can have a lower gain and the sidelobes can be higher. The antenna does not have to be steered over a full 360° in azimuth.

The basic requirement for the array in this application is to provide coverage over as large an azimuth angle as possible with the gain being approximately $16dB$ as calculated in Appendix A. This antenna can be used as the foundation for the design of a more complex antenna which would be suitable for use in a hostile environment.

The RPVs which have been flown in Canada have been equipped with simple antenna systems consisting of monopole or microstrip slot antennas. These antennas have provided basic transmission capability but have restricted the

Frequency	E-Band
Bandwidth	10%
Beamwidth	5° Azimuth 5° Elevation
Steering Angle	360° Azimuth ±45° Elevation
Gain	$30dB$
Polarization	Circular
Impedance	50 Ohm

Table 2.1: RPV Video Link Antenna Specifications

range and operating attitudes of the RPVs. These restrictions have been overcome temporarily by using higher power transmitters and by mounting more than one antenna on the vehicle and remotely switching between the antennas to obtain the best signal at the ground control station. The capabilities of the onboard navigation and control systems have advanced to the stage where the operational ranges of the RPVs now exceed the video downlink range. To accommodate the longer ranges it is necessary to develop an antenna system which has the gain required to provide a reliable video downlink signal. To reduce the complexity of the design it is necessary to steer the antenna in azimuth only and to provide a fixed wide beamwidth elevation pattern.

The azimuth beamwidth in conjunction with the allowable ripple in the resulting composite pattern will determine the number of control bits required by the phase shifters. Compromises may be made at this stage to facilitate the fabrication of the antenna. The beamwidth of the antenna tends to spread out at high steering angles from broadside. This effect may result in a reduction in the number of phase shifter control bits required by the system.

The RPV will require at least two arrays with one unit located on each

side of the vehicle to provide the nearly 360° coverage required. The RPV will have blind spots in the forward and rearward directions, however, the effect of these blind spots can be lessened through proper choice of flight profile.

2.2 Choice of Antenna

At the frequency of 2360 MHz required for this application, the physical dimensions of a mechanically steered antenna would be unmanageable. The use of an electronically steered antenna consisting of an array of relatively low gain antenna elements is practical. The available low gain elements consist of monopole, slot, printed dipole, or patch antenna elements. Physically the antenna best suited for use on an RPV is the microstrip patch. Microstrip antennas can be made conformal to the body of the RPV. A conformal antenna is desirable as aerodynamically the antenna should not affect the performance of the vehicle. Microstrip antennas are also relatively thin and therefore use very little of the internal volume, if any, of the RPV. The elements are easily fabricated and the entire array including the feed network can be built as a complete assembly. Microstrip elements are relatively narrow bandwidth devices, however, the bandwidth available is suitable for this requirement. Circular polarization is available from microstrip patch antennas through the choice of patch shape and/or feed arrangements.

Chapter 3

Analysis of the Circular Patch Microstrip Antenna

3.1 Introduction

The construction of a circular patch microstrip antenna is shown in Figure 3.1. The antenna consists of a circular patch of conductor separated from a ground plane by a dielectric substrate. The dielectric substrate typically has a dielectric constant, ϵ_r, of between 2 and 10. The patch can be fed by a microstrip line or by a feed probe.

Many approaches to the problem of mathematically analyzing the operation of circular patch microstrip antennas have been reported. The following methods are described by Bahl and Bhartia [13];

- cavity model
- cavity model with feed source
- modal expansion model
- wire grid model

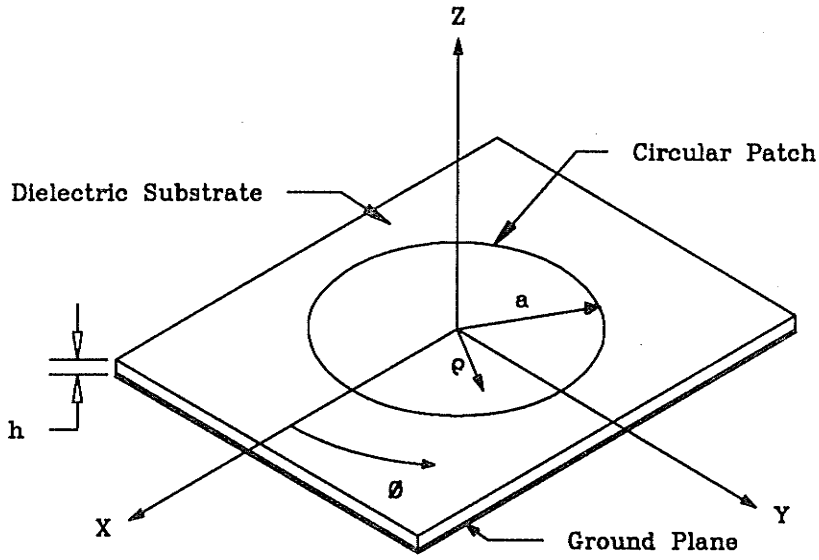

Figure 3.1: Circular patch microstrip antenna

- Green's function method.

The cavity model is simple to use, while still being useful in predicting the performance of a circular patch microstrip antenna. The simplest cavity model assumes that the source can be represented by a magnetic current alone. Shafai et al. [12] have improved on this model by assuming that both electric and magnetic currents act as sources. The improved cavity model assumes that these currents are located at the physical aperture of the antenna instead of at the air dielectric interface as in the simple cavity model.

3.2 Cavity Model Analysis

The simple cavity model method assumes that the microstrip antenna can be modeled as an ideal cavity bounded by electric walls on the top and bottom, and by a magnetic wall on the periphery. The improved cavity model assumes that the aperture of the antenna has a finite admittance. This effect leads to the addition of an electric current source at the aperture. The total electric

field is the sum of the individual fields due to the electric and magnetic sources.

The cavity model assumes that the electric field within the antenna has only a z-component. If the substrate is electrically thin, $h \ll \lambda$, the electric field is assumed not to vary in the z-direction and the component of the current normal to the edge of the patch is assumed to be zero. For simplicity the time variation, $e^{j\omega t}$, has been suppressed in the following analysis.

The boundary value problem for the cavity model with no excitation is given by:

$$(\nabla^2 + k^2)\bar{E} = 0 \tag{3.1}$$

for

$$\begin{aligned} 0 &< \rho < a \\ 0 &< \phi < 2\pi \\ 0 &< z < h \end{aligned}$$

where $\bar{E} = E_z\hat{z}$ and $k = \omega\sqrt{\mu\epsilon}$

Using the separation of variables technique [15] the following general solution to the wave equation is obtained,

$$E_z = [C_1 J_n(k_{nm}\rho) + C_2 Y_n(k_{nm}\rho)][C_3 \cos n\phi + C_4 \sin n\phi] \tag{3.2}$$

where C_1—C_4 are constants.

As the solution must be valid at $\rho = 0$, then $C_2 = 0$ as $Y_n(0)$ is equal to infinity and the solution becomes unbounded. If the solution is to be symmetric about $\phi = 0$ then C_4 is also equal to zero. The solution has now been simplified to

$$E_z = C J_n(k_{nm}\rho)\cos n\phi \tag{3.3}$$

where C is a constant.

The magnetic wall at $\rho = a$ imposes the boundary condition, $\hat{n} \times \bar{H} = 0$ where

$$\bar{H} = -\frac{1}{j\omega\mu}(\nabla \times \bar{E}) \tag{3.4}$$

Mode (n,m)	Root $k_{nm}a$
0,1	0
1,1	1.84118
2,1	3.05424
0,2	3.83171
3,1	4.20119

Table 3.1: Roots of $J_n'(k_{nm}a) = 0$

This constraint results in

$$\frac{\partial E_z}{\partial \rho} = 0 \tag{3.5}$$

at $\rho = a$. Combining equations 3.3 and 3.5 yields the following eigenvalue equation,

$$J_n'(k_{nm}a) = 0 \tag{3.6}$$

Equation 3.6 indicates that the solution is valid at the zeros of the Bessel function of order n. These zeros define the operating modes, TM_{nm}, of the circular microstrip patch antenna. Table 3.1 lists the zeros of the first few operational modes [13].

3.3 Linear Radiation Patterns

The radiation pattern of a circular microstrip patch antenna can be found by using vector potential functions [16]. The far-field radiation due to an electric current source $\bar{J}$ can be found by first evaluating the magnetic vector potential $\bar{A}$ given by

$$\bar{A} = \frac{\mu}{4\pi} \iiint_V \bar{J} \frac{e^{-jkR}}{R} dv' \tag{3.7}$$

where R is the distance from any point on the source to the observation point. The θ and ϕ components of the radiated $\bar{E}$-fields due to the electric current

source can then be obtained from

$$E_\theta \simeq -j\omega A_\theta \tag{3.8}$$

$$E_\phi \simeq -j\omega A_\phi \tag{3.9}$$

Similarly the far-field radiation due to a magnetic current source $\bar{M}$ can be found by evaluating the electric vector potential $\bar{F}$ given by

$$\bar{F} = \frac{\varepsilon}{4\pi} \iiint_V \bar{M} \frac{e^{-jkR}}{R} dv' \tag{3.10}$$

The θ and ϕ components of the radiated $\bar{E}$-fields due to the magnetic current source are then obtained from

$$E_\theta \simeq -j\omega\eta F_\phi \tag{3.11}$$

$$E_\phi \simeq +j\omega\eta F_\theta \tag{3.12}$$

The required magnetic and electric surface currents are obtained as follows. The antenna is first modeled as a cavity with a magnetic surface current on the periphery, $\rho = a$, given by

$$\begin{aligned} \bar{I}_a^m &= 2\bar{E} \times \hat{n} \\ &= 2E_z \hat{z} \times \hat{\rho} \\ &= 2E_z \hat{\phi} \end{aligned} \tag{3.13}$$

where E_z is obtained from Equation 3.3 and $\hat{n}$ is a unit vector normal to the magnetic wall. The antenna is then modeled as a cavity with an electric surface current on the periphery given by

$$\begin{aligned} \bar{I}_a^e &= 2\hat{n} \times \bar{H} \\ &= 2\hat{\rho} \times H_\phi \hat{\phi} \\ &= 2H_\phi \hat{z} \end{aligned} \tag{3.14}$$

The magnetic field, H_ϕ, at $\rho = a$ is given by

$$H_\phi = -y_a E_z \tag{3.15}$$

where y_a is the wall admittance of the patch antenna. The factor of 2 arises in the above equations as the antennas are assumed to be mounted on an infinite ground plane. By using image theory the radiated fields in the upper hemisphere can be obtained by using an equivalent source consisting of real and imaginary sources. Equations 3.13 and 3.14 are substituted into Equations 3.7 and 3.10 as shown in Appendix B and the θ and ϕ components of the magnetic and electric vector potentials are found to be

$$A_\theta = j^n \mu a h y_a E_a \frac{e^{-jkr}}{r} J_n(ka\sin\theta)\sin\theta\cos n\phi \tag{3.16}$$

$$F_\theta = j^{n-1} \varepsilon a h \frac{E_a}{2} \frac{e^{-jkr}}{r} (J_{n-1}(ka\sin\theta) - J_{n+1}(ka\sin\theta))\cos n\phi \tag{3.17}$$

$$F_\phi = j^{n-1} \varepsilon a h \frac{E_a}{2} \frac{e^{-jkr}}{r} (J_{n-1}(ka\sin\theta) + J_{n+1}(ka\sin\theta))\cos\theta\sin n\phi \tag{3.18}$$

Using Equations 3.8, 3.9, and 3.11 the far-field radiated $\bar{E}$-fields are found to be

$$E_\theta^e = -j^{n+1} k a h y_a \eta E_a \frac{e^{-jkr}}{r} J_n(ka\sin\theta)\sin\theta\cos n\phi \tag{3.19}$$

$$E_\theta^m = j^n k a h \frac{E_a}{2} \frac{e^{-jkr}}{r} (J_{n+1}(ka\sin\theta) - J_{n-1}(ka\sin\theta))\cos n\phi \tag{3.20}$$

$$E_\phi^m = j^n k a h \frac{E_a}{2} \frac{e^{-jkr}}{r} (J_{n+1}(ka\sin\theta) + J_{n-1}(ka\sin\theta))\cos\theta\sin n\phi \tag{3.21}$$

3.4 Circular Radiation Patterns

To obtain acceptable performance from an antenna mounted on an RPV it is desirable that the signal is not degraded by the relative attitude of the

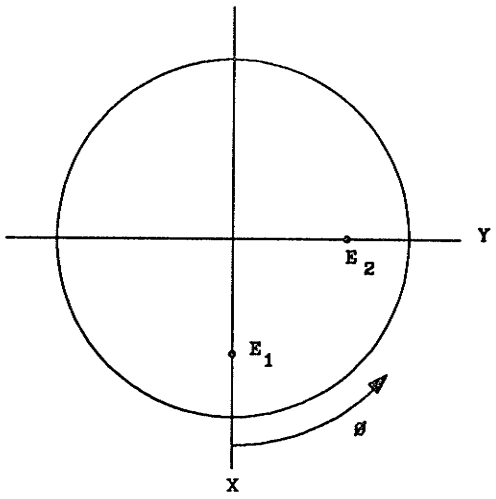

Figure 3.2: TM_{11} Feed Arrangement for Circular Polarization

RPV antenna to the ground station antenna. If the RPV antenna is circularly polarized the effect of polarization mismatch at the receiving antenna is minimized. A circular microstrip patch antenna can be designed to radiate circularly polarized radiation through the proper choice of feed locations and feed phase relationships. When a circular patch microstrip antenna operating in the TM_{11} mode is fed as shown in Figure 3.2 with $E_2 = jE_1$ the radiation will be circularly polarized. To simplify the equations in the following sections let

$$C = kh\frac{e^{-jkr}}{r} \tag{3.22}$$

The linear far-field components of the radiation pattern are then given by

$$E_\theta^e = -j^{n+1}Ca_n y_{an}\eta E_a J_n(ka_n \sin\theta)\sin\theta\cos n\phi \tag{3.23}$$

$$E_\theta^m = j^n Ca_n\frac{E_a}{2}(J_{n+1}(ka_n\sin\theta) - J_{n-1}(ka_n\sin\theta))\cos n\phi \tag{3.24}$$

$$E_\phi^m = j^n Ca_n\frac{E_a}{2}(J_{n+1}(ka_n\sin\theta) + J_{n-1}(ka_n\sin\theta))\cos\theta\sin n\phi \tag{3.25}$$

where a_n and y_{an} are the radius and aperture wall admittances respectively of an element operating in the TM_{n1} mode. The real part of the wall admittance

as given by Shafai et al. [12] is

$$\mathcal{R}(y_{an}) = \frac{ah}{2\pi\omega\mu}\int_0^{2\pi}\frac{\cos n\alpha}{r^3}[(1+\cos^2\frac{\alpha}{2})(\sin kr - kr\cos kr) - k^2r^2\sin^2\frac{\alpha}{2}\sin kr]d\alpha \tag{3.26}$$

where $r = 2a\sin\frac{\alpha}{2}$. The imaginary part of the wall admittance is given by [12]

$$\mathcal{I}(y_{an}) = \omega\varepsilon_0\varepsilon_r\Delta a(1 - \frac{n^2}{k^2a_e^2}) \tag{3.27}$$

where $\Delta a = (a_e - a)$ and

$$\Delta a_e = a(1+\Delta)^{\frac{1}{2}} \tag{3.28}$$

$$\Delta = \frac{2h}{\pi\varepsilon_r a}[\ln(\frac{a}{2h}) + 1.41\varepsilon_r + 1.77 + \frac{h}{a}(0.268\varepsilon_r + 1.65)] \tag{3.29}$$

The actual radius of the circular patch microstrip antenna is given by a while a_e is an equivalent radius which takes into account the effects of the fringe fields on the periphery of the patch.

The total E_θ and E_ϕ fields are given by

$$E_\theta = E_\theta^e + E_\theta^m \tag{3.30}$$

$$E_\phi = E_\phi^m \tag{3.31}$$

The circular polarization far-field patterns of the TM_{11} and TM_{21} modes are presented in the following sections.

3.4.1 TM_{11} Mode

Referring to Figure 3.2 for TM_{11} mode operation the E_θ^e component due to E_1 is given by

$$E_{\theta 1}^{eE1} = a_1 y_{a1} E_{a1}\eta J_1(ka\sin\theta)\sin\theta\cos\phi \tag{3.32}$$

while the E_θ^e component due to E_2 is given by

$$\begin{aligned} E_{\theta 1}^{eE2} &= a_1 y_{a1} E_{a2}\eta J_1(ka\sin\theta)\sin\theta\cos(\phi - 90) \\ &= a_1 y_{a1} E_{a2}\eta J_1(ka\sin\theta)\sin\theta\sin\phi \end{aligned} \tag{3.33}$$

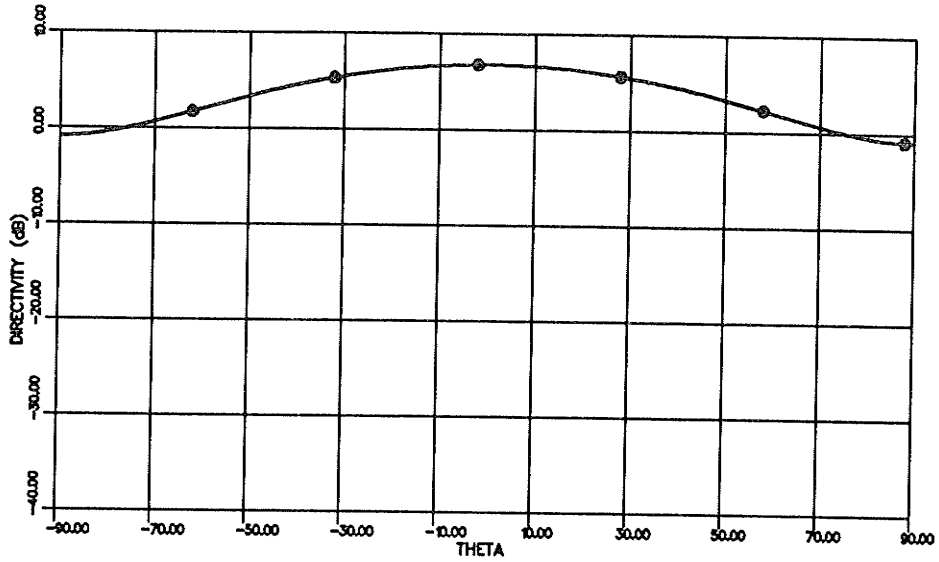

Figure 3.3: TM_{11} Mode Copolar Radiation Pattern

The total E_θ^e field due to E_1 and E_2 is given by

$$\begin{aligned} E_{\theta 1}^{eT} &= E_\theta^{eE1} + E_\theta^{eE2} \\ &= Ca_1 y_{a1} \eta J_1(ka \sin\theta) \sin\theta (E_{a1} \cos\phi + E_{a2} \sin\phi) \end{aligned} \tag{3.34}$$

if $E_2 = jE_1$ then

$$\begin{aligned} E_{\theta 1}^{eT} &= Ca_1 y_{a1} \eta J_1(ka \sin\theta) \sin\theta E_{a1} (\cos\phi + j \sin\phi) \\ &= CE_{a1} a_1 y_{a1} \eta J_1(ka \sin\theta) \sin\theta e^{j\phi} \end{aligned} \tag{3.35}$$

In a similar fashion the total E_θ^m and E_ϕ^m fields due to E_1 and E_2 are given by

$$E_{\theta 1}^{mT} = jCa_1 \frac{E_{a1}}{2} (J_2(ka_1 \sin\theta) - J_0(Ka_1 \sin\theta)) e^{j\phi} \tag{3.36}$$

$$E_{\phi 1}^{mT} = Ca_1 \frac{E_{a1}}{2} (J_2(ka_1 \sin\theta) + J_0(Ka_1 \sin\theta)) \cos\theta e^{j\phi} \tag{3.37}$$

The far-field patterns of the TM_{11} mode are shown in Figure 3.3.

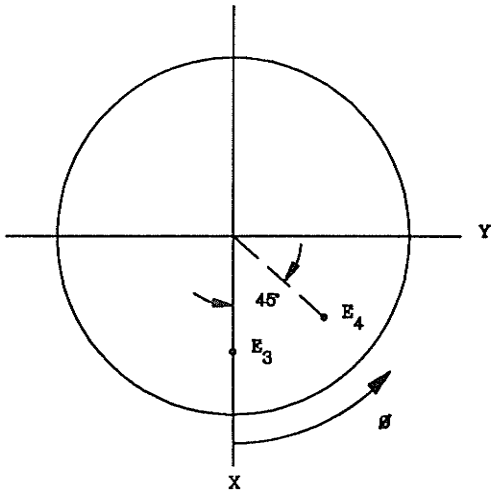

Figure 3.4: TM_{21} Feed Arrangement for Circular Polarization

3.4.2 TM_{21} Mode

When a circular patch microstrip antenna operating in the TM_{21} mode is fed as shown in Figure 3.4 the radiation will be circularly polarized. The far-field patterns of the TM_{21} mode are derived in a similar fashion to those of the TM_{11} mode and are given by ($E_4 = jE_3$)

$$E_{\theta 2}^{eT} = jCE_{a3}a_2 y_{a2}\eta J_2(ka_2 \sin\theta)\sin\theta e^{j2\phi} \quad (3.38)$$

$$E_{\theta 2}^{mT} = -Ca_2\frac{E_{a3}}{2}(J_3(ka_2 \sin\theta) - J_1(Ka_2 \sin\theta))e^{j2\phi} \quad (3.39)$$

$$E_{\phi 2}^{mT} = jCa_2\frac{E_{a3}}{2}(J_3(ka_2 \sin\theta) + J_1(Ka_2 \sin\theta))\cos\theta e^{j2\phi} \quad (3.40)$$

The far-field patterns of the TM_{21} mode are shown in Figure 3.5.

3.4.3 Combined TM_{11} and TM_{21} Mode

The far field pattern can be shaped by combining the patterns of the TM_{11} and TM_{21} modes by stacking elements as shown in Figure 3.6. The resulting

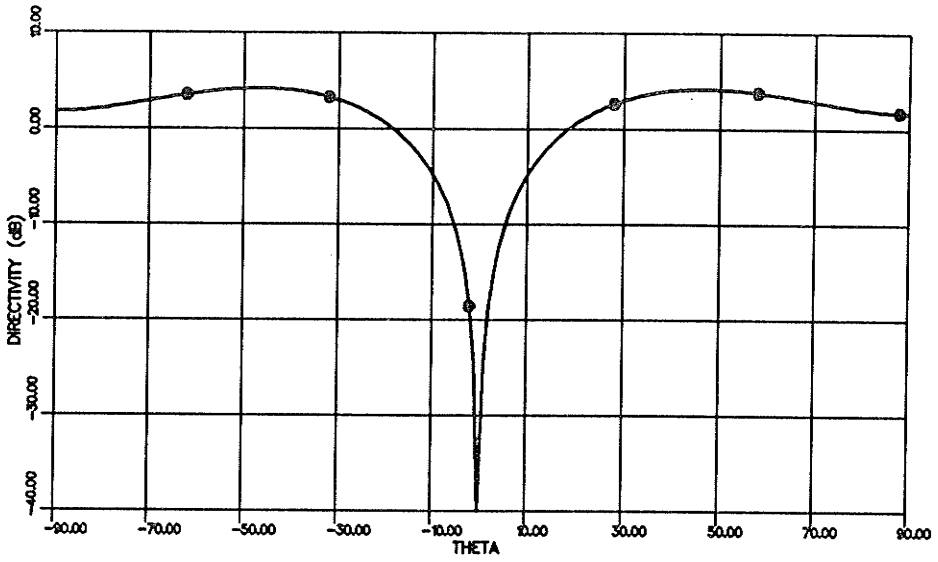

Figure 3.5: TM_{21} Mode Copolar Radiation Pattern

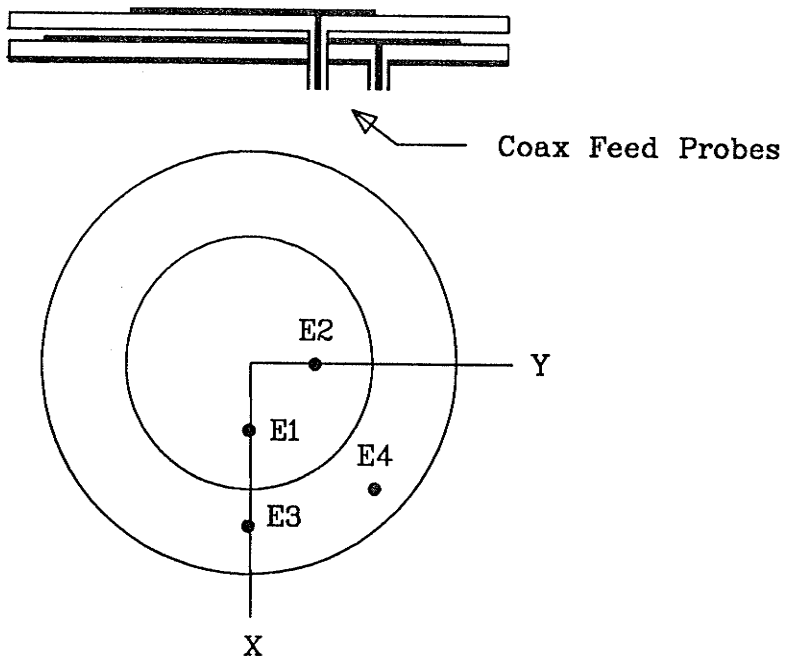

Figure 3.6: Construction of a Dual Mode (TM_{11} and TM_{21}) Element

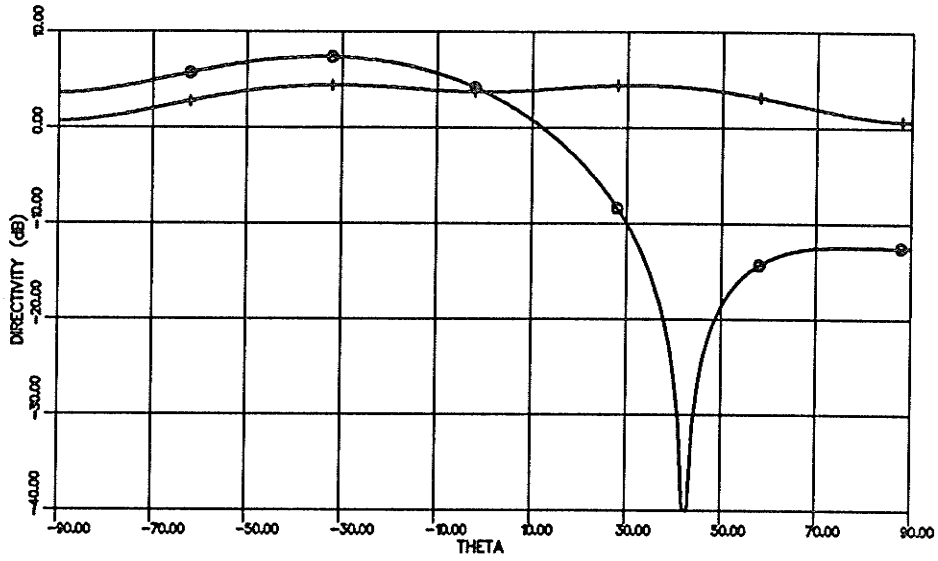

Figure 3.7: Far-field Pattern of a Dual Mode (TM_{11} and TM_{21}) Element + $\phi = 0°$ *plane*, ∘ $\phi = 90°$ *plane*

far-field pattern is given by ($E_3 = E_1$)

$$E^{eT}_{\theta 12} = C\eta E_1 \sin\theta (a_1 y_{a1} J_1(ka_1 \sin\theta) e^{j\phi} + ja_2 y_{a2} J_2(ka_2 \sin\theta) e^{j2\phi}) \quad (3.41)$$

$$E^{mT}_{\theta 12} = jC\frac{E_1}{2}(a_1(J_2(ka_1 \sin\theta) - J_0(Ka_1 \sin\theta))e^{j\phi} + ja_2(J_3(ka_2 \sin\theta) - J_1(Ka_2 \sin\theta))e^{j2\phi}) \quad (3.42)$$

$$E^{mT}_{\phi 12} = C\frac{E_1}{2}\cos\theta(a_1(J_2(ka_1 \sin\theta) + J_0(Ka_1 \sin\theta))e^{j\phi} + ja_2(J_3(ka_2 \sin\theta) + J_1(Ka_2 \sin\theta))e^{j2\phi}) \quad (3.43)$$

and the far-field pattern is shown in Figure 3.7.

3.5 Polarization and Directivity

3.5.1 Circular Polarization

In the far field the spherical wave has only θ and ϕ components and can be represented by [17]

$$\bar{E} = (E_\theta \hat{\theta} + E_\phi \hat{\phi}) e^{j\omega t} \tag{3.44}$$

This can be rewritten as

$$\begin{aligned} \bar{E} &= E_\theta(\hat{\theta} + \rho_L \hat{\phi}) \\ \rho_L &= \frac{E_\phi}{E_\theta} \end{aligned} \tag{3.45}$$

where ρ_L is the linear polarization ratio which is a complex constant. In general Equation 3.45 represents an elliptically polarized wave which includes the special cases of linear and circular polarization. If $\rho_L = e^{\pm j\frac{\pi}{2}}$ then the wave is circularly polarized.

The tilt of the ellipse is given by τ as shown in Figure 3.8. The axial ratio (AR) is defined as

$$\begin{aligned} AR &= \frac{major\ axis}{minor\ axis} \\ &= \frac{OA}{OB} \end{aligned}$$

where

$$1 \leq AR \leq \infty \tag{3.46}$$

If the polarization of the receiving antenna does not match that of the transmitting antenna there is a polarization mismatch and maximum power is not transferred. When the transmit and receive antennas both have the same polarization and alignment maximum power will be transferred. If the antennas are both circularly polarized and have the same sense of polarization, either right hand or left hand, then maximum power will be transmitted independent of their rotational alignment. Circularly polarized antennas are required for

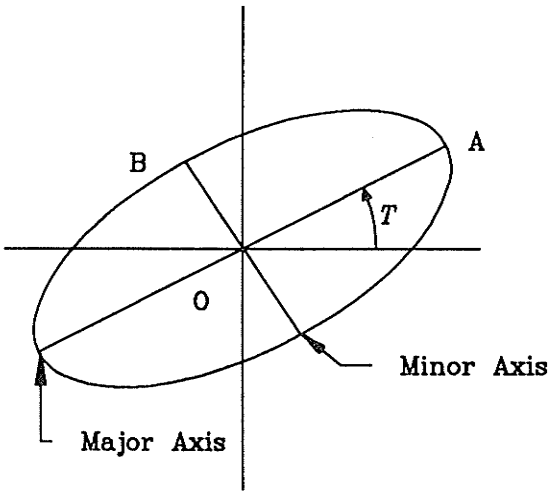

Figure 3.8: Polarization Ellipse

an RPV data link as the antennas are not fixed in space and the relative angles between the antennas vary.

Right and left hand circular polarization can be defined in terms of linear components by two unit vectors given by

$$\hat{R} = \frac{1}{\sqrt{2}}(\hat{\theta} - j\hat{\phi})$$
$$\hat{L} = \frac{1}{\sqrt{2}}(\hat{\theta} + j\hat{\phi})$$

These vectors are used to define copolar and cross-polar components respectively for a nominally right hand polarized wave. The right hand copolar component of a spherical wave is given by

$$E_{co} = \hat{R}^* \cdot \bar{E} \tag{3.47}$$

and the cross-polar component is given by

$$E_x = \hat{L}^* \cdot \bar{E} \tag{3.48}$$

If the E_θ and E_ϕ components of a spherical wave are represented by

$$\bar{E}_\theta = f(\theta)e^{j\phi}\hat{\theta} \tag{3.49}$$

$$\bar{E}_\phi = -jg(\theta)e^{j\phi}\hat{\phi} \tag{3.50}$$

and

$$\begin{aligned}\bar{E}_T &= \bar{E}_\theta + \bar{E}_\phi \\ &= [f(\theta)\hat{\theta} - jg(\theta)\hat{\phi}]e^{j\phi}\end{aligned} \tag{3.51}$$

then the right hand copolar component is given by

$$\begin{aligned}E_{co} &= \frac{1}{\sqrt{2}}(\hat{\theta} + j\hat{\phi}) \cdot [f(\theta)\hat{\theta} - jg(\theta)\hat{\phi}]e^{j\phi} \\ &= \frac{1}{\sqrt{2}}(|f(\theta)| + j|g(\theta)|)e^{j\phi}\end{aligned} \tag{3.52}$$

or in a slightly different form as [12]

$$\begin{aligned}E_{co} &= \frac{(\hat{\theta} + j\hat{\phi})}{\sqrt{2}} \cdot \bar{E} \\ &= \frac{(\hat{\theta} + j\hat{\phi})}{\sqrt{2}} E_1(\theta, \phi)\end{aligned} \tag{3.53}$$

and

$$\begin{aligned}E_x &= \frac{(\hat{\theta} + j\hat{\phi})}{\sqrt{2}} \cdot \bar{E} \\ &= \frac{(\hat{\theta} + j\hat{\phi})}{\sqrt{2}} E_2(\theta, \phi)\end{aligned} \tag{3.54}$$

where the amplitudes of E_1 and E_2 are given by

$$|E_1| = \frac{1}{\sqrt{2}}\{|f(\theta)|^2 + |g(\theta)|^2 + 2|f(\theta)||g(\theta)|\cos(\theta_f - \theta_g)\}^{\frac{1}{2}} \tag{3.55}$$

$$|E_2| = \frac{1}{\sqrt{2}}\{|f(\theta)|^2 + |g(\theta)|^2 - 2|f(\theta)||g(\theta)|\cos(\theta_f - \theta_g)\}^{\frac{1}{2}} \tag{3.56}$$

The gain patterns for copolar and cross-polar radiation components are given by

$$G_{co}(\theta, \phi) = \frac{4\pi r^2 |E_1(\theta, \phi)|^2}{120\pi \cdot 2P_t} \tag{3.57}$$

$$G_x(\theta, \phi) = \frac{4\pi r^2 |E_2(\theta, \phi)|^2}{120\pi \cdot 2P_t} \tag{3.58}$$

where P_t represents the total power radiated by the antenna due to a single input.

3.5.2 Directivity

The directivity of an antenna is a measure of the intensity of the radiation in the direction of the maximum to the overall average radiation intensity. Therefore directivity is given by [18]

$$Directivity = \frac{maximum\ radiation\ intensity}{average\ radiation\ intensity} = \frac{U_{max}}{U_0} \tag{3.59}$$

The average radiation intensity is given by

$$U_0 = \frac{1}{4\pi r^2}\int_0^{2\pi}\int_0^{\pi} P(\theta,\phi) r^2 \sin^2\theta d\theta d\phi \tag{3.60}$$

which is the total radiated power divided by the area of a unit sphere.

$$\begin{aligned} P(\theta,\phi) &= \frac{1}{2}\mathcal{R}\{\bar{E}\times\bar{H}\} \\ &= \frac{1}{2}\mathcal{R}\{E_\theta H_\phi^* - E_\phi H_\theta^*\} \\ &= \frac{1}{2\eta}(|E_\theta(\theta,\phi)|^2 + |E_\phi(\theta,\phi)|^2) \end{aligned} \tag{3.61}$$

where $\eta = 120\pi$ is the intrinsic impedance of free space and $E_\theta = \eta H_\phi$ and $E_\phi = -\eta H_\theta$ in the far field. The directivity of the antenna is therefore given by,

$$D(\theta,\phi) = \frac{4\pi(|E_\theta(\theta,\phi)|^2 + |E_\phi(\theta,\phi)|^2)}{\int_0^{2\pi}\int_0^{\pi} P(\theta,\phi)\sin\theta d\theta d\phi} \tag{3.62}$$

The numerical results in the rest of this report are based on the following approximation of Equation 3.62

$$D(\theta,\phi) = \frac{4\pi[|E_\theta(\theta,\phi)|^2 + |E_\phi(\theta,\phi)|^2]}{\sum_{m=1}^{\frac{360}{\Delta\theta}}\sum_{n=1}^{\frac{180}{\Delta\phi}}[|E_\theta(m\Delta\theta,n\Delta\phi)|^2 + |E_\phi(m\Delta\theta,n\Delta\phi)|^2]\sin(m\Delta\theta)\Delta\theta\Delta\phi} \tag{3.63}$$

The gain and directivity of an antenna are related to one another by the efficiency of the antenna. Directivity can be obtained from radiation magnitude

plots while gain is obtained experimentally in order to find the losses in the antenna and the feed network.

3.6 Impedance

It is important to know the input impedance characteristics of an antenna to enable proper matching of the antenna to the feed source. The amount of power reflected by the antenna is related to how well the impedance of the antenna is matched to the impedance of the source. The input impedance of an antenna is defined as the ratio of the voltage to the current at the input terminals of the antenna with no load attached. The maximum power is transferred to the antenna when the source and the antenna are conjugate matched, that is when

$$\begin{aligned} R_S &= R_A \\ X_S &= -X_A \end{aligned}$$

Where R_S and R_A are the resistances of the source and antenna, respectively, and X_S and X_A are the reactances of the source and antenna, respectively.

The admittance of a circular microstrip patch antenna is given by [12]

$$Y_a = \frac{\pi a}{h}[\frac{J_n(k_{nm}a)}{J_n(k_{nm}c)}]^2 y_a \tag{3.64}$$

where y_a is the self admittance of the patch as given by Equations 3.26 and 3.27 and Y_a is the admittance of the patch when it is fed at a. The input resistance of the circular patch microstrip antenna can be matched to the source by properly choosing the feed point such that

$$\frac{1}{R_S} = \frac{\pi a}{h}[\frac{J_n(k_{nm}a)}{J_n(k_{nm}c)}]^2 \mathcal{R}(ya) \tag{3.65}$$

The results of these equations are not exact and the final values may have to be obtained experimentally. In experimental work by Antoszkiewicz et al. [19]

the input impedance was shown to change noticeably when the size of the ground plane was varied. This effect is of concern here as the design equations assume an infinite ground plane. In the case of the stacked elements used here the size of the ground plane of the top element is determined by the size of the bottom element.

The above equations do not include the effect of the probe reactance on the input impedance of the antenna. Nor do they include the effect on the impedance of individual elements in the array due to mutual coupling between elements in the array.

Chapter 4

Array Design

4.1 Introduction

The microstrip patch elements analyzed in the previous Chapter have relatively wide radiation patterns with correspondingly low directivities. If a number of these elements are operated together in unison the result is an array antenna. The individual elements used in an array antenna are used to replace a single large antenna which has greater directivity. Array antennas can be made to alter the pointing angle of their main lobe through the proper choice of excitation phasing. The overall pattern of an array antenna can be modified by changing the geometric configuration of the array, the spacing of the elements, the relative excitation in terms of amplitude and phase of the individual elements and the radiation pattern of the basic element used in the array.

A two dimensional planar array as shown in Figure 4.1 was used to model the RPV antenna under study. The antenna has 2 elements in the x-direction and 8 or 10 elements in the y-direction. The electric field radiation pattern of an array is given by

$$E_{array} = (E_{single\ element})(AF) \tag{4.1}$$

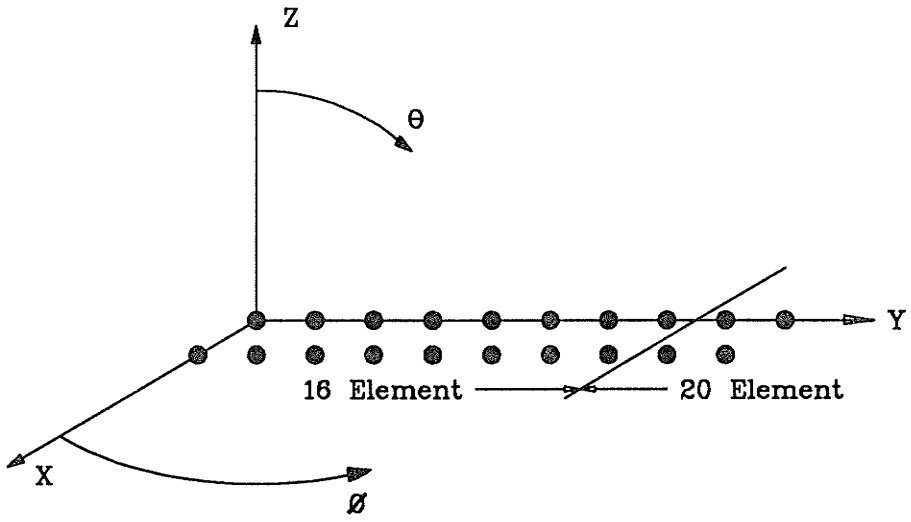

Figure 4.1: Two dimensional planar array

where $E_{single\ element}$ is the far field radiation pattern of a single element located at the origin and AF is the array factor. The array factor of a uniformly excited array is given by

$$AF = I_0 \sum_{m=1}^{M} e^{(m-1)(kd_x \sin\theta\cos\phi+\beta_x)} \sum_{n=1}^{N} e^{(n-1)(kd_y \sin\theta\sin\phi+\beta_y)} \tag{4.2}$$

where d_x and d_y are the seperations of the elements in the x and y-directions, respectively, β_x and β_y are the relative phases between the elements in the x and y-directions, respectively, and M and N are the number of elements in the x and y-directions, respectively. By varying β_x and β_y the main lobe of the array can be steered to the desired location. The main beam can be pointed in the $\theta = \theta_0$ and $\phi = \phi_0$ direction by making the progressive phase shifts between elements in the x and y directions equal to

$$\beta_x = -kd_x \sin\theta_0 \cos\phi_0 \tag{4.3}$$

$$\beta_y = -kd_y \sin\theta_0 \sin\phi_0 \tag{4.4}$$

The resulting main beam position may not be exactly in the $\theta = \theta_0$, $\phi = \phi_0$

direction due to the pattern of the individual element used and the effect of mutual coupling between elements in the array.

4.2 Mutual Coupling

When individual antenna elements are utilized in close proximity to each other as in the case of an array the current distribution within the individual elements may be changed. The change in current distribution alters the radiation pattern and input impedance of the individual elements. The input impedance of an array element is dependent on the self impedance of the element in the absence of other elements or surroundings as well as the mutual coupling between the element and its operational environment. In order to accurately control the performance of an array it is necessary to know the active impedance of the individual elements in the array so that their excitation can be adjusted in phase and amplitude as required to obtain the desired pattern. Shafai et al. [12] has analyzed the effect of mutual coupling between circular microstrip patch antennas with the following results;

- Mutual admittance varies with the separation distance in a fashion similar to a damped oscillation.
- E-plane coupling is stronger than H-plane coupling

An estimate of the performance of an array can be still obtained even if the effects of mutual coupling are neglected.

4.3 Evaluated Arrays

Three different planar array configurations of 16 and 20 elements in 2×8 and 2×10 configurations were examined. In two of the configurations the centre to centre spacing between the elements was varied. The separations were

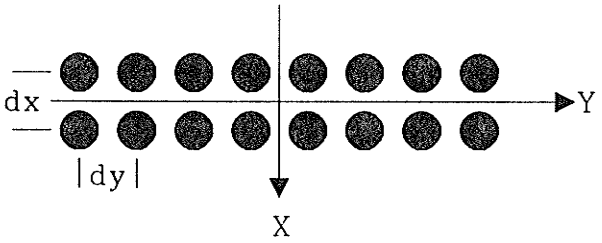

Figure 4.2: TM_{11} mode 2 × 8 array configuration

varied between the minimal acceptable spacing dictated by mutual coupling effects and 1λ. The minimum separations were chosen to be $.5\lambda$ for the TM_{11} mode elements and $.7\lambda$ for the TM_{21} mode elements. These separations left slightly more than $.1\lambda$ separation between the edges of the patches. In all of the cases examined the elements were assumed to be uniformly excited and radiation pattern calculations were carried out at ten degree increments in the commanded pointing angle.

4.3.1 TM_{11} Configuration

The TM_{11} mode 2×8 array configuration is shown in Figure 4.2. Figures 4.3 to 4.11 show the radiation pattern of the array as it is steered from $\theta = 0°$ *to* $80°$ in the $\phi = 270°$ direction when the element centre to centre spacing is $.5\lambda$. The arrays described in this thesis can be steered in both the $\phi = 90°$ or $\phi = 270°$ directions, and reference to one direction will imply similar results in the other direction.

When the array is steered to broadside ($\theta = 0°$) the first sidelobes are approximately $13.5dB$ down from the main lobe which is consistent with a figure of $13.3dB$ for the array factor of a uniform line source. As previously noted when the array is commanded to point in a particular direction the

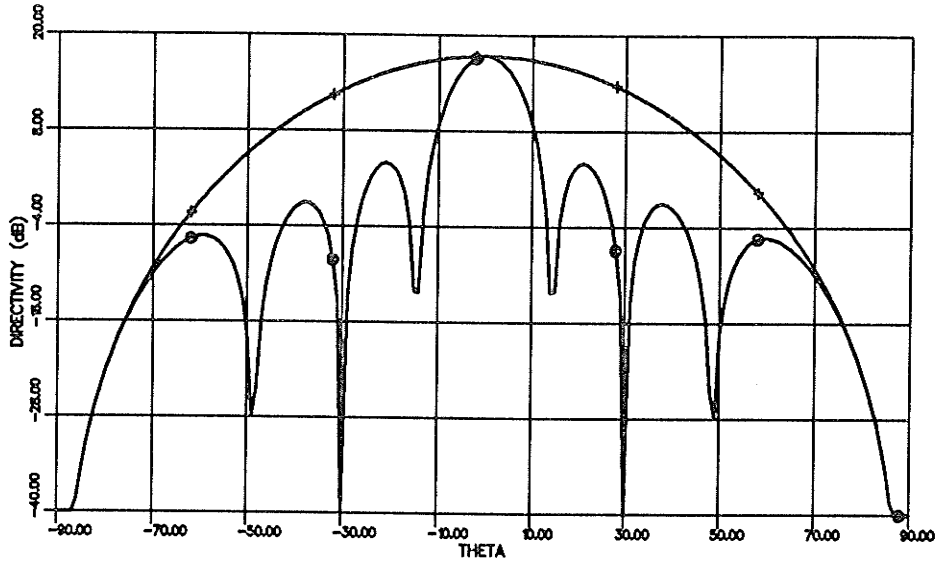

Figure 4.3: TM_{11} mode 2×8 array scanned to $\phi = 270°$ and $\theta = 0°$ ($+$ $\phi = 0°$ *plane*, $\circ$ $\phi = 90°$ *plane*)

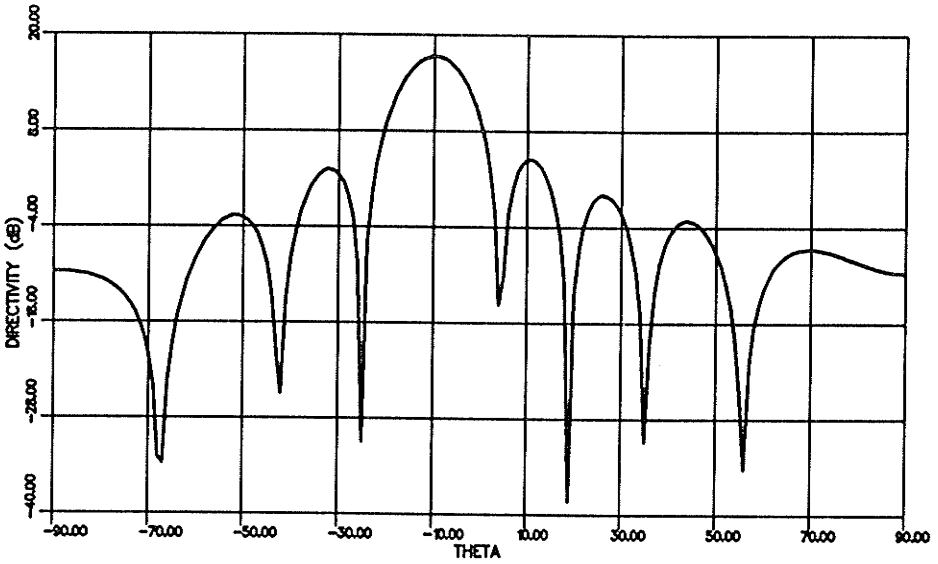

Figure 4.4: TM_{11} mode 2×8 array scanned to $\phi = 270°$ and $\theta = 10°$ ($\phi = 90°$ *plane*)

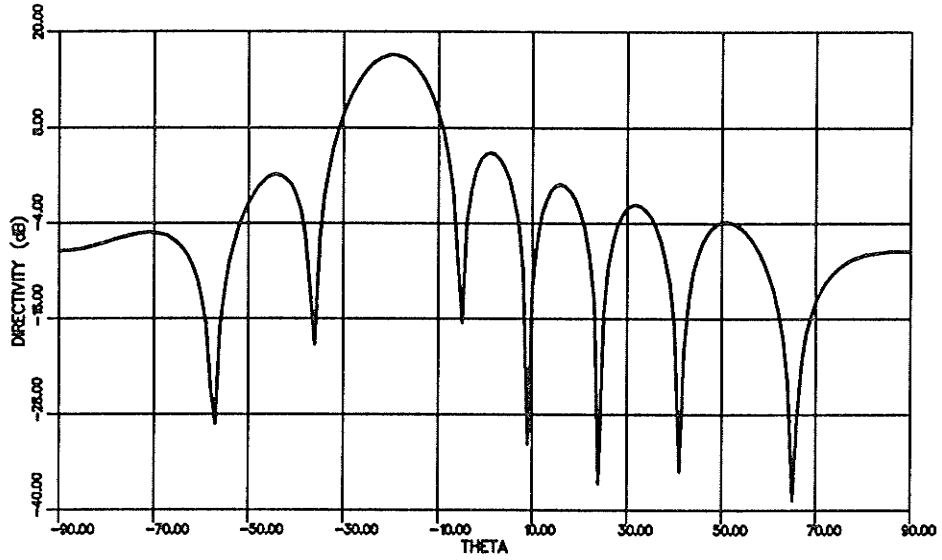

Figure 4.5: TM_{11} mode 2×8 array scanned to $\phi = 270°$ and $\theta = 20°$ ($\phi = 90°$ *plane*)

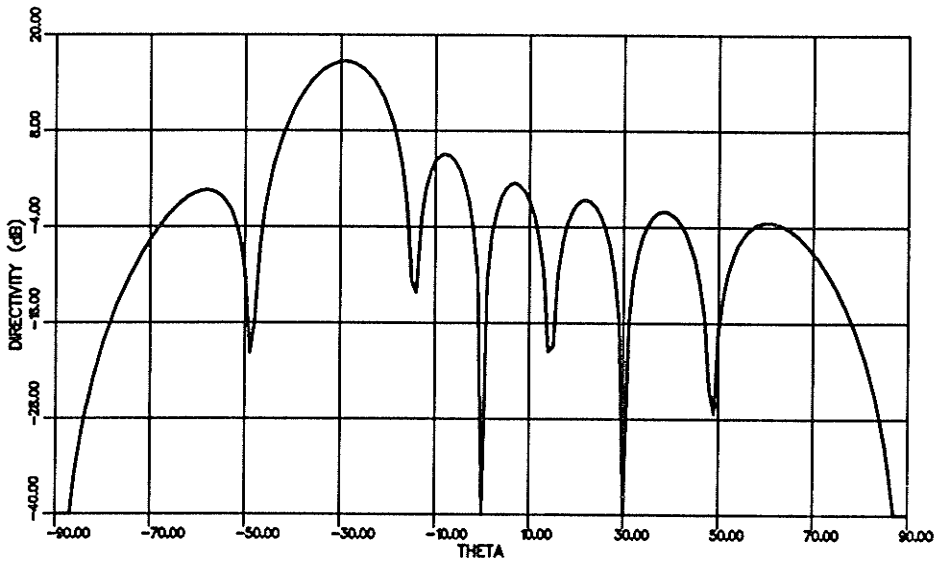

Figure 4.6: TM_{11} mode 2×8 array scanned to $\phi = 270°$ and $\theta = 30°$ ($\phi = 90°$ *plane*)

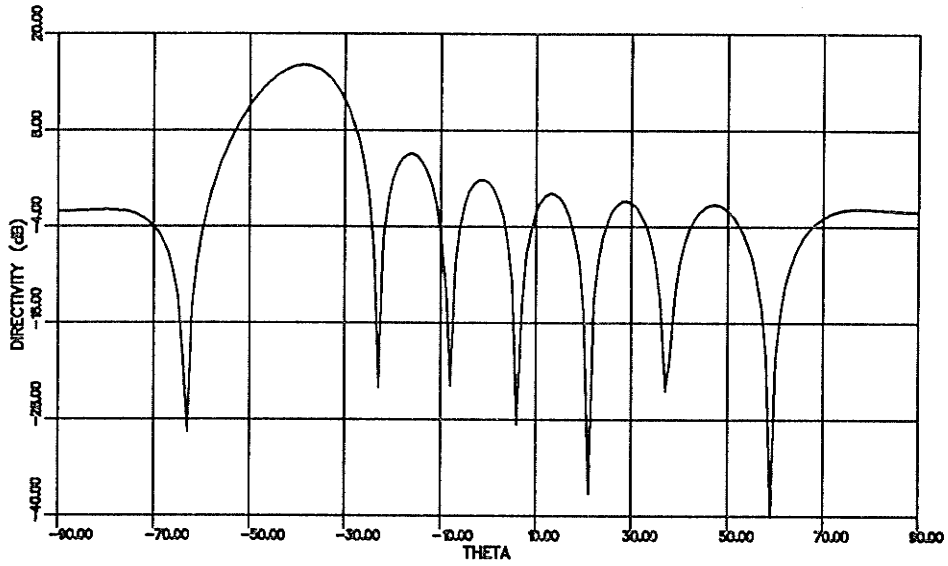

Figure 4.7: TM_{11} mode 2×8 array scanned to $\phi = 270°$ and $\theta = 40°$ ($\phi = 90°$ *plane*)

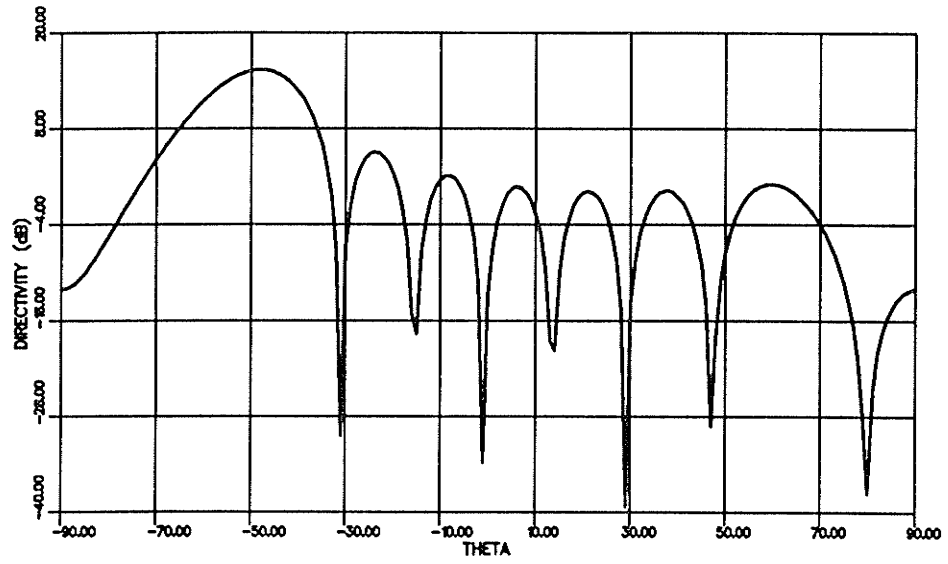

Figure 4.8: TM_{11} mode 2×8 array scanned to $\phi = 270°$ and $\theta = 50°$ ($\phi = 90°$ *plane*)

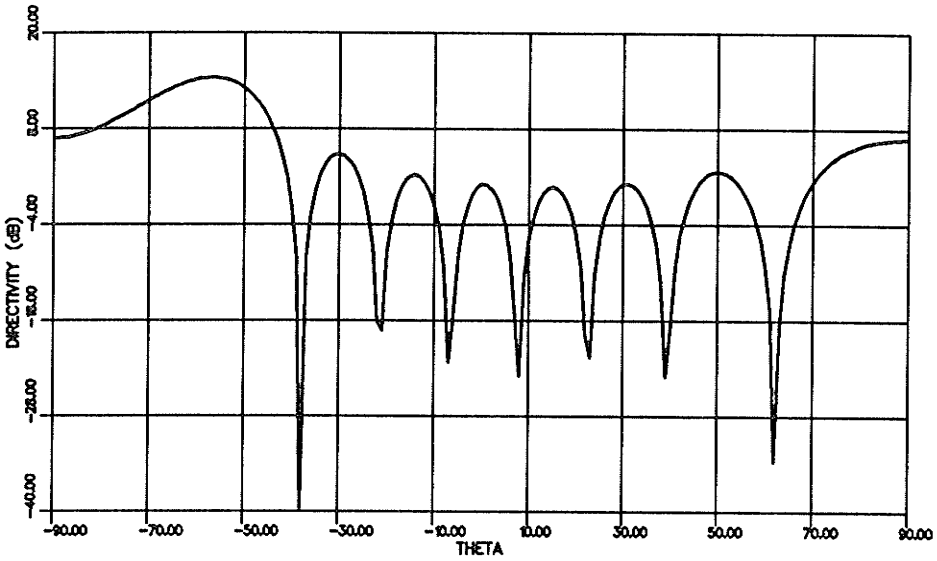

Figure 4.9: TM_{11} mode 2×8 array scanned to $\phi = 270°$ and $\theta = 60°$ ($\phi = 90°$ *plane*)

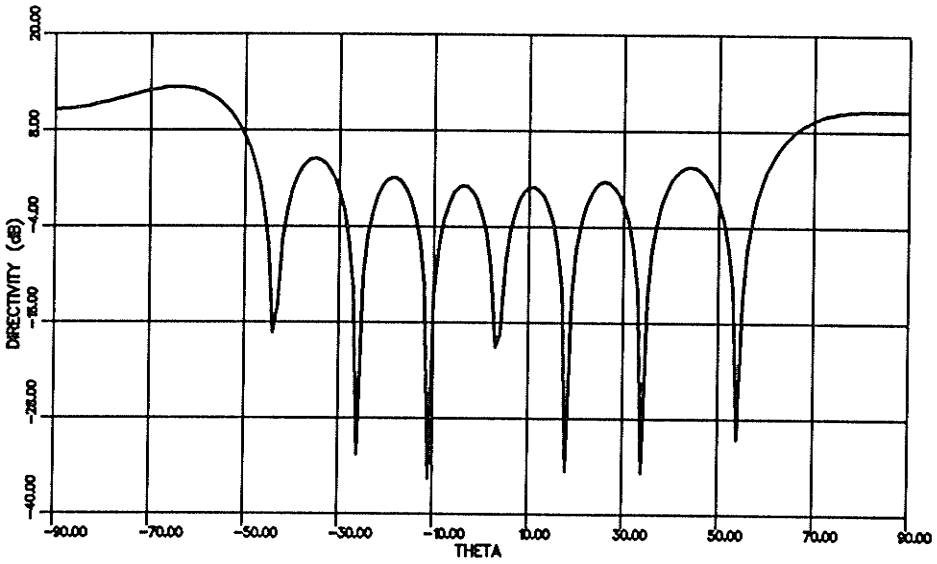

Figure 4.10: TM_{11} mode 2×8 array scanned to $\phi = 270°$ and $\theta = 70°$ ($\phi = 90°$ *plane*)

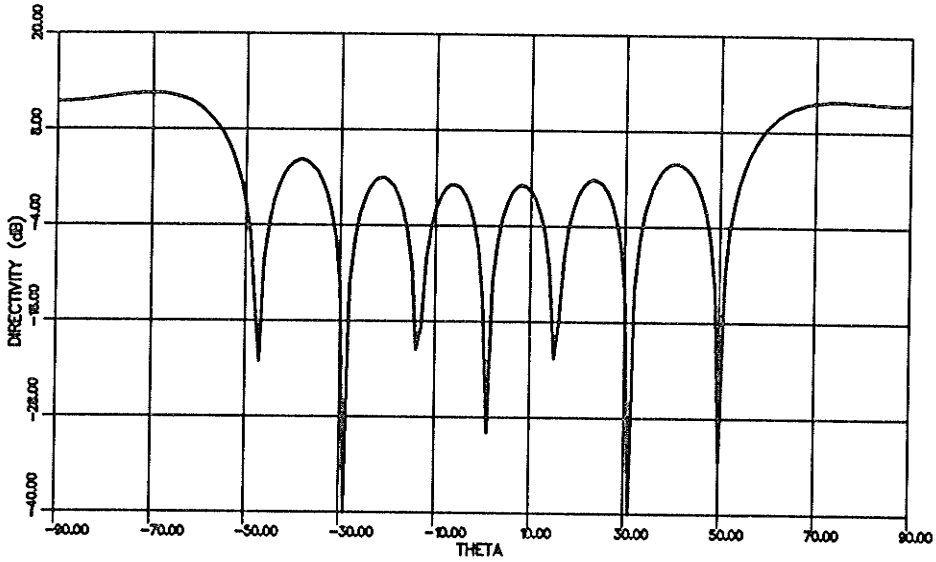

Figure 4.11: TM_{11} mode 2×8 array scanned to $\phi = 270°$ and $\theta = 80°$ ($\phi = 90°$ *plane*)

main lobe may not point in that exact direction. This effect is illustrated in Figure 4.12 where the actual pointing direction of the main lobe is plotted against the commanded direction. As the beam is scanned from broadside the gain goes down as shown in Figure 4.13. At scan angles larger than 60° from broadside in the $\phi = 90/270°$ plane a grating lobe appears which eventually becomes as large as the main lobe of the array as the array is steered to the endfire direction (90° from broadside). As the separation between the elements is increased the effective aperture of the array is increased and the directivity of the array increases correspondingly. This trend reverses as the element separation approaches 1λ as grating lobes appear in the radiation pattern and the directivity of the main beam is decreased. Figures 4.14 to 4.18 show the relationship between commanded and actual scan angles for configurations with spacings of .6 *to* 1.0 λ.

Figures 4.19 to 4.23 show the effect of command angle on the directivity of the main lobe and on the highest sidelobe. As the inter-element spacing is

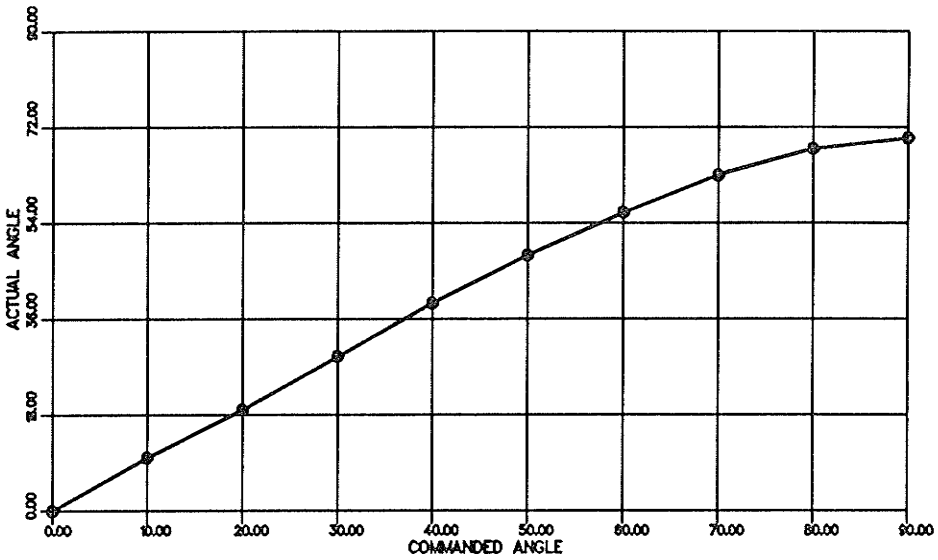

Figure 4.12: Actual versus commanded steering angle for a TM_{11} mode array with $dx = dy = .5\lambda$

increased the grating lobes occur at lower commanded scan angles and tend to be larger than the main lobe at commanded angles close to endfire.

4.3.2 TM_{11} *and* TM_{21} Configuration

The combined TM_{11} and TM_{21} mode 2×8 array configuration is the same as that of the TM_{11} configuration except for the use of the dual mode elements. The radiation patterns of an array with an inter-element spacing of $.7\lambda$ for commanded angles of $\theta = 0°$ *to* $80°$ are shown in Figures 4.24 to 4.32. The gain of the array at broadside is similar to that of a similarly sized TM_{11} mode array. As the commanded scan angle increases the sidelobes increase in magnitude, however they never reach the same magnitude as the main lobe as is the case in the TM_{11} array.

The array has its maximum directivity when steered to approximately 20° from broadside. This is due to the pattern shaping induced by the individual dual mode elements which have their maximum directivity at 32° from

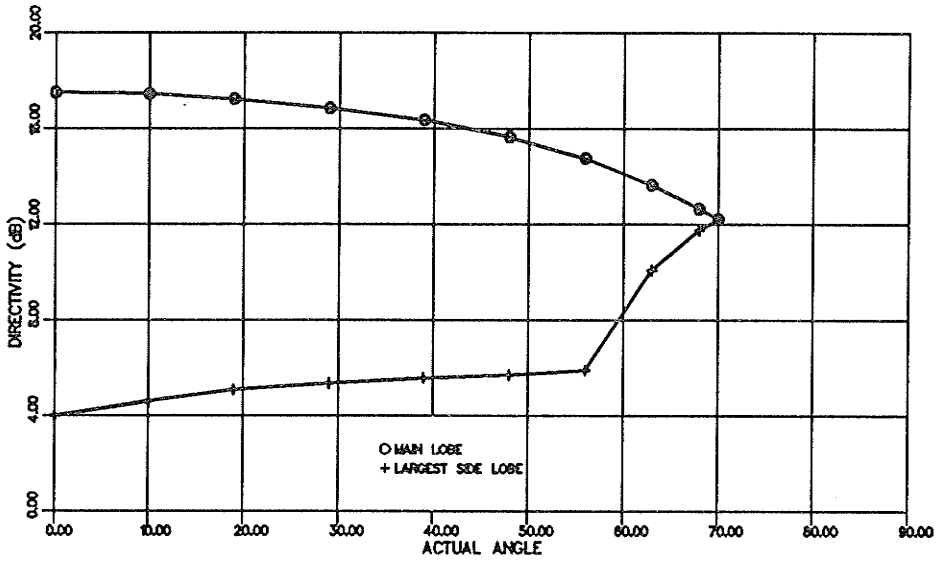

Figure 4.13: Gain versus actual steering angle for a TM_{11} mode array with $dx = dy = .5\lambda$

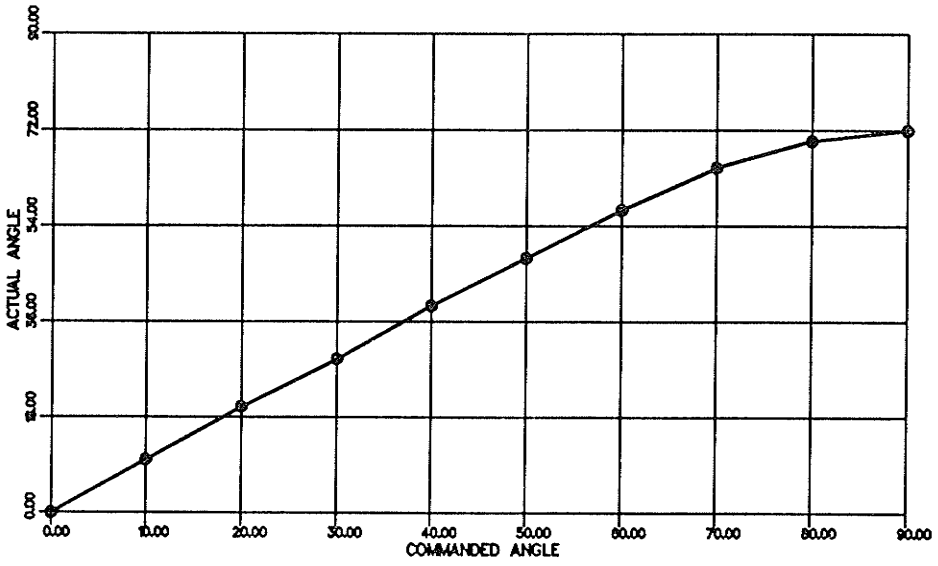

Figure 4.14: Actual versus commanded steering angle for a TM_{11} mode array with $dx = .5\lambda$, $dy = .6\lambda$

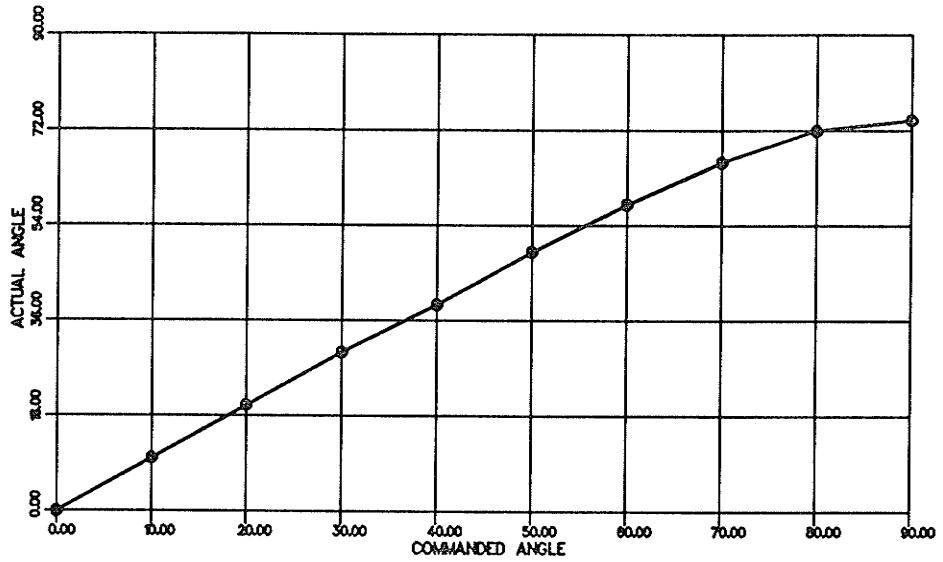

Figure 4.15: Actual versus commanded steering angle for a TM_{11} mode array with $dx = .5\lambda$, $dy = .7\lambda$

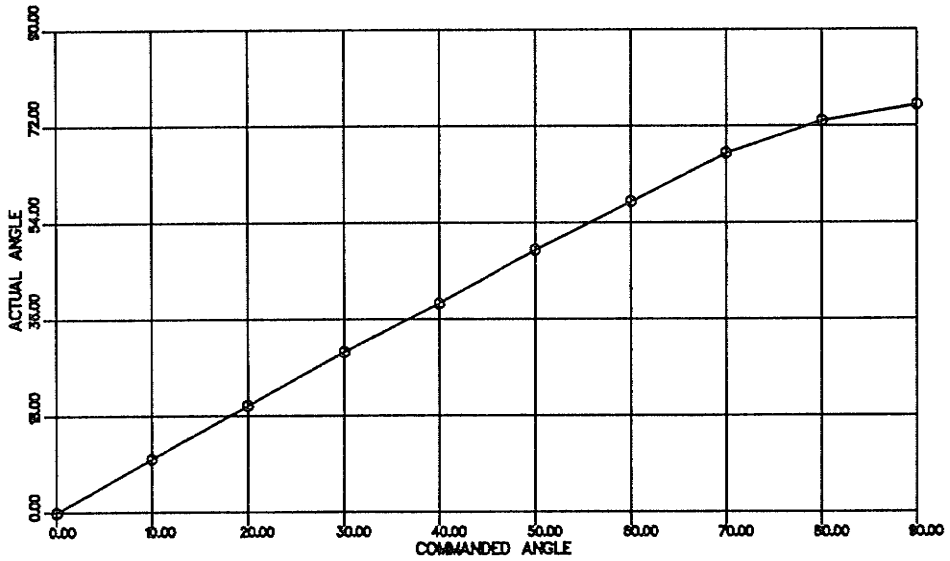

Figure 4.16: Actual versus commanded steering angle for a TM_{11} mode array with $dx = .5\lambda$, $dy = .8\lambda$

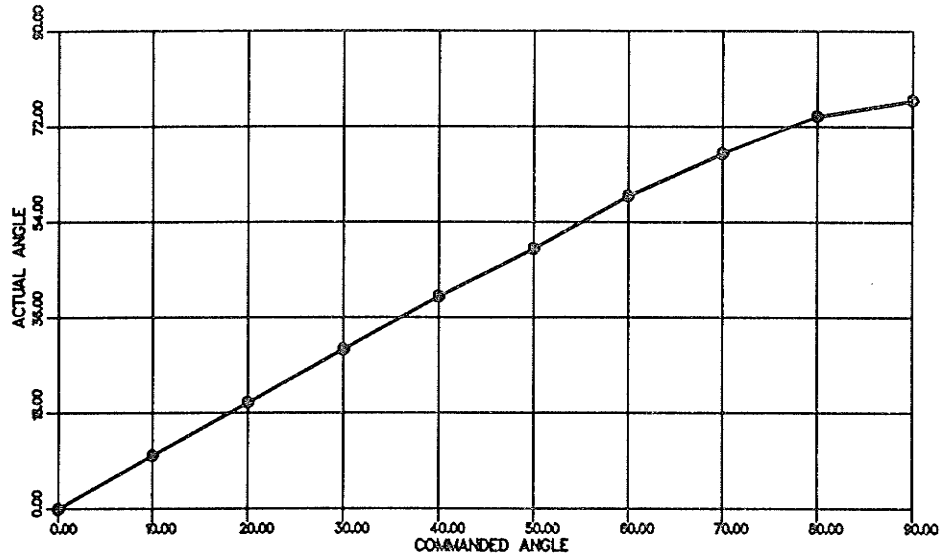

Figure 4.17: Actual versus commanded steering angle for a TM_{11} mode array with $dx = .5\lambda$, $dy = .9\lambda$

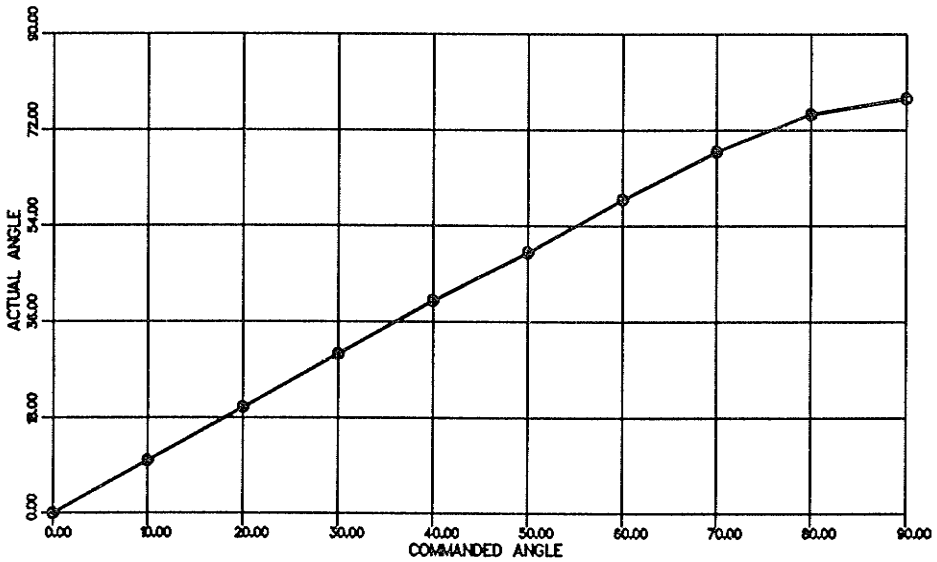

Figure 4.18: Actual versus commanded steering angle for a TM_{11} mode array with $dx = .5\lambda$, $dy = \lambda$

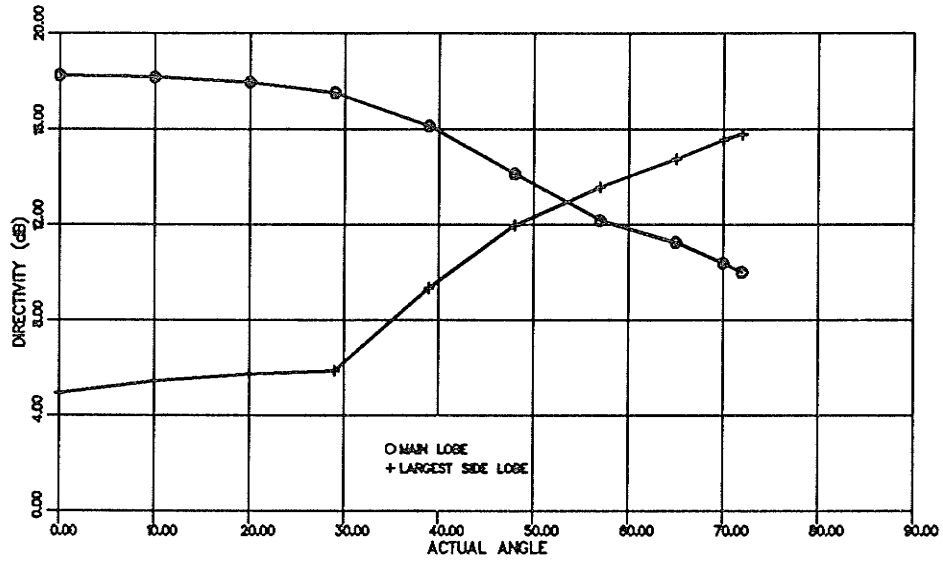

Figure 4.19: Gain versus actual steering angle for a TM_{11} mode array with $dx = .5\lambda$, $dy = .6\lambda$

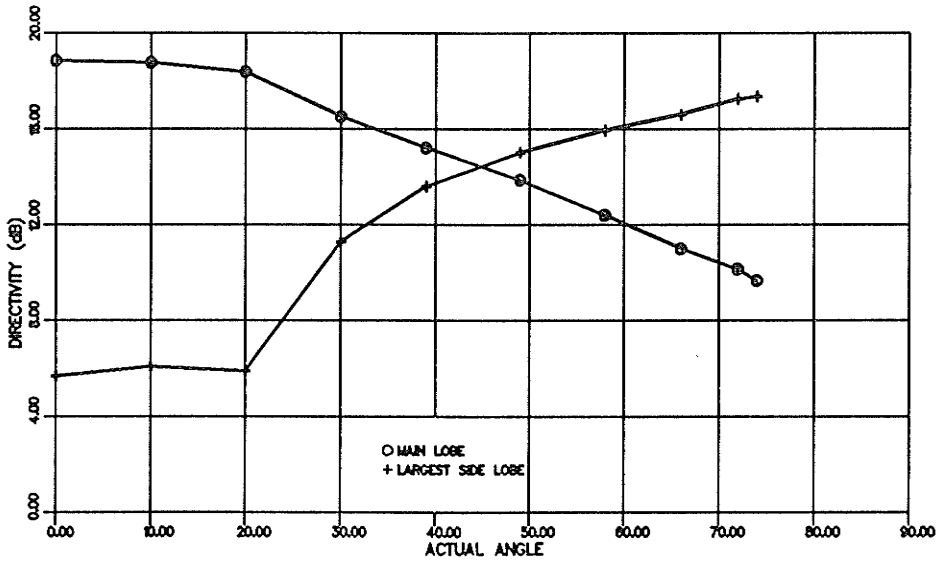

Figure 4.20: Gain versus actual steering angle for a TM_{11} mode array with $dx = .5\lambda$, $dy = .7\lambda$

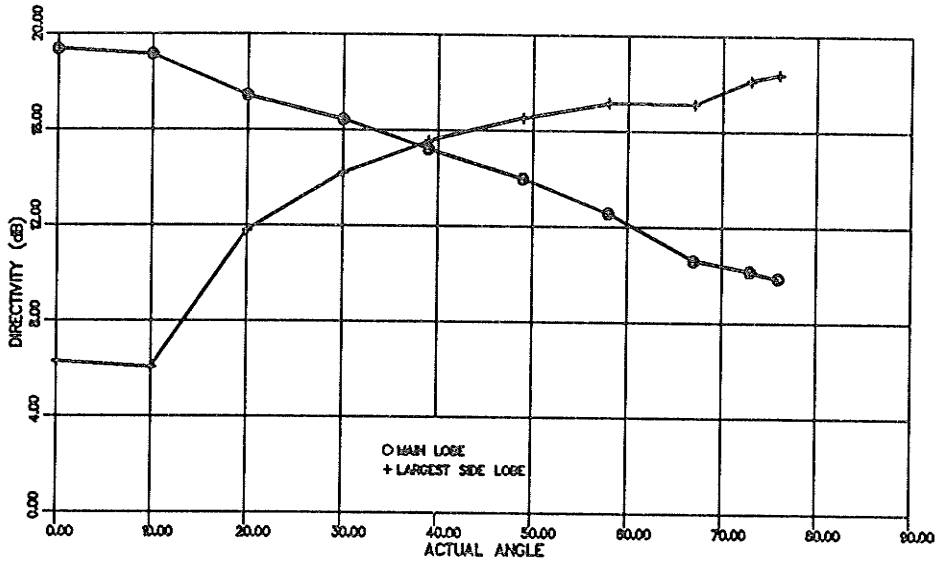

Figure 4.21: Gain versus actual steering angle for a TM_{11} mode array with $dx = .5\lambda$, $dy = .8\lambda$

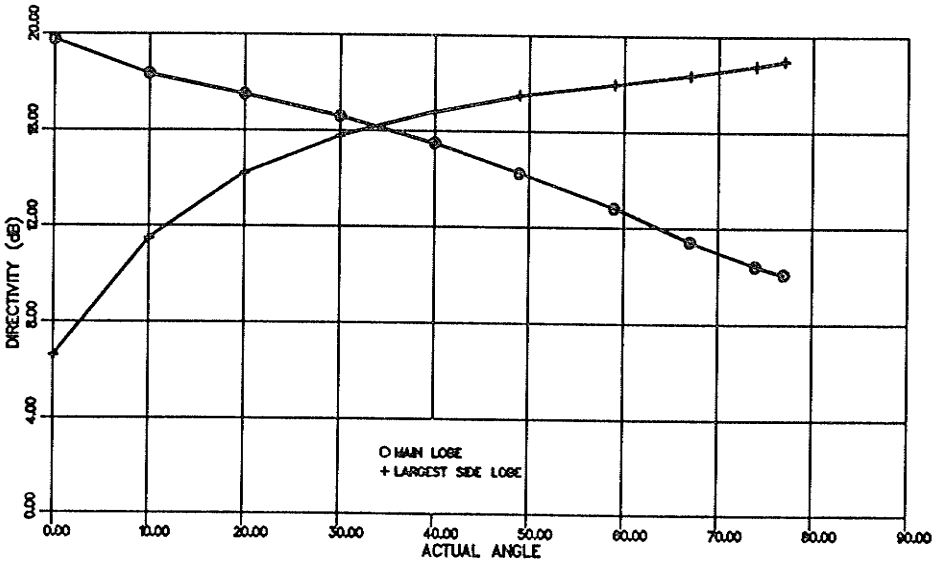

Figure 4.22: Gain versus actual steering angle for a TM_{11} mode array with $dx = .5\lambda$, $dy = .9\lambda$

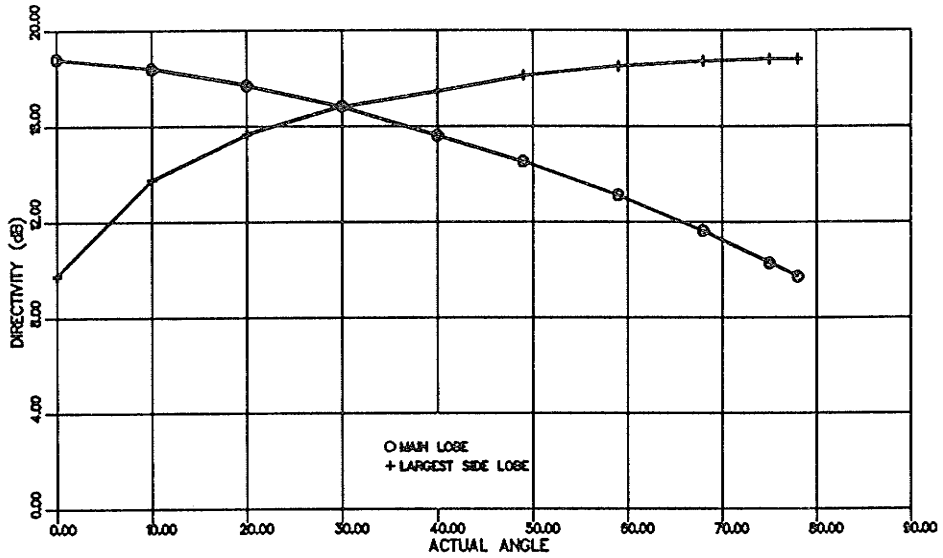

Figure 4.23: Gain versus actual steering angle for a TM_{11} mode array with $dx = .5\lambda$, $dy = \lambda$

broadside. The behavior of the array with respect to commanded angle and actual pointing angle and the gain obtained are similar to those of the TM_{11} mode. The directivity of the array decreases and grating lobes appear as the array is scanned in the endfire direction. These characteristics are much less pronounced than in the TM_{11} case as the radiation pattern of the dual mode element has less magnitude in the direction of the grating lobes.

When the spacing between elements in the y-direction is varied between $.8\lambda$ and λ, the grating lobes become more pronounced. Figures 4.33 to 4.36 show the relationship between commanded steering angle and the actual pointing angle of the array as the inter-element spacing is changed. As the separation between elements is increased the array can steer closer to the endfire direction. Figures 4.37 to 4.40 show the effect of inter-element spacing on the gain of the main and largest sidelobe of the array as the spacing is changed. As in the case of the TM_{11} mode array the sidelobe levels increase at high commanded pointing angles as the inter-element spacing is increased.

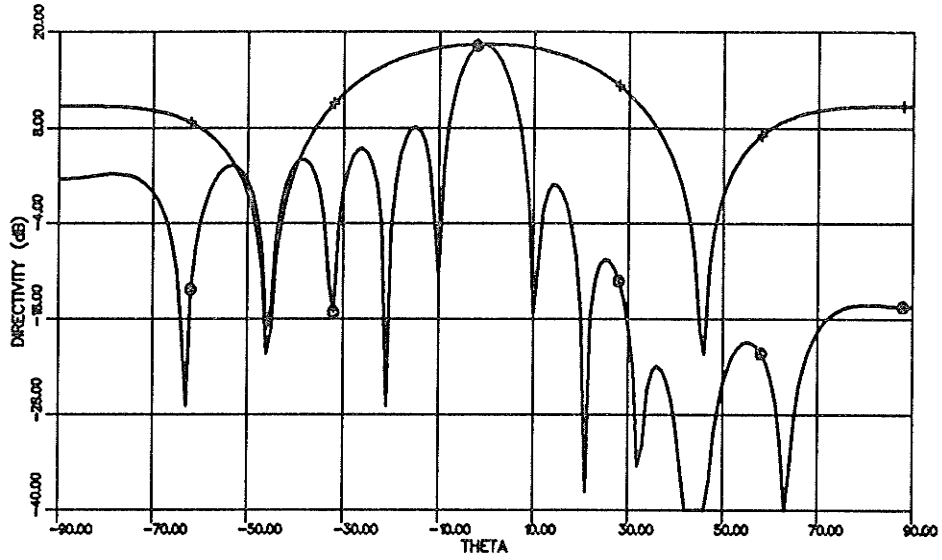

Figure 4.24: Dual mode 2×8 array scanned to $\phi = 270°$ and $\theta = 0°$ ($+$ $\phi = 0°$ *plane*, o $\phi = 90°$ *plane*)

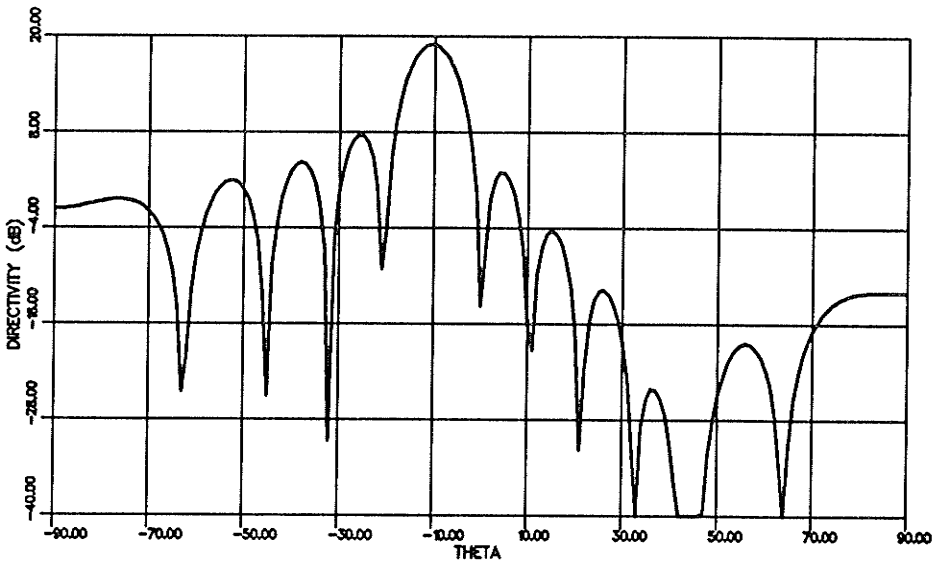

Figure 4.25: Dual mode 2×8 array scanned to $\phi = 270°$ and $\theta = 10°$ ($\phi = 90°$ *plane*)

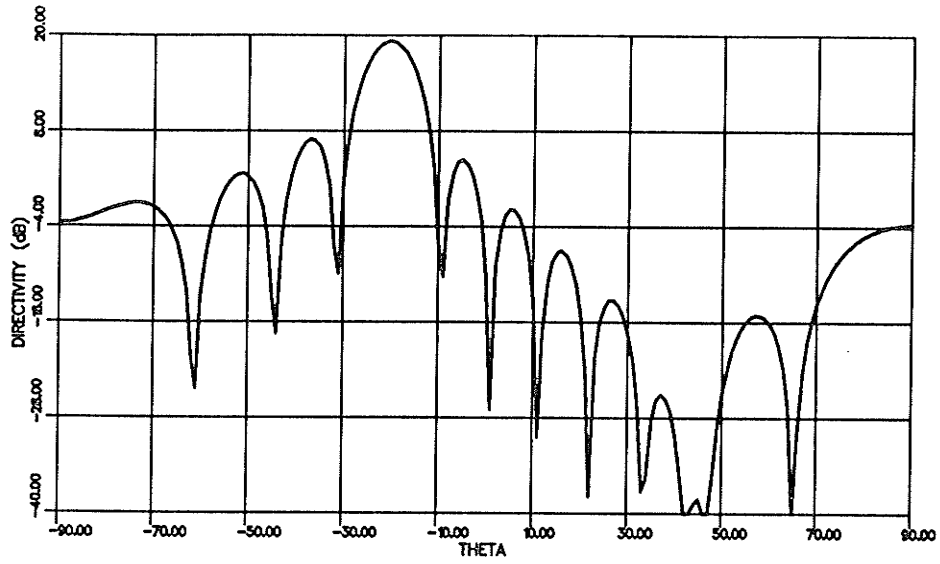

Figure 4.26: Dual mode 2×8 array scanned to $\phi = 270°$ and $\theta = 20°$ ($\phi = 90°$ *plane*)

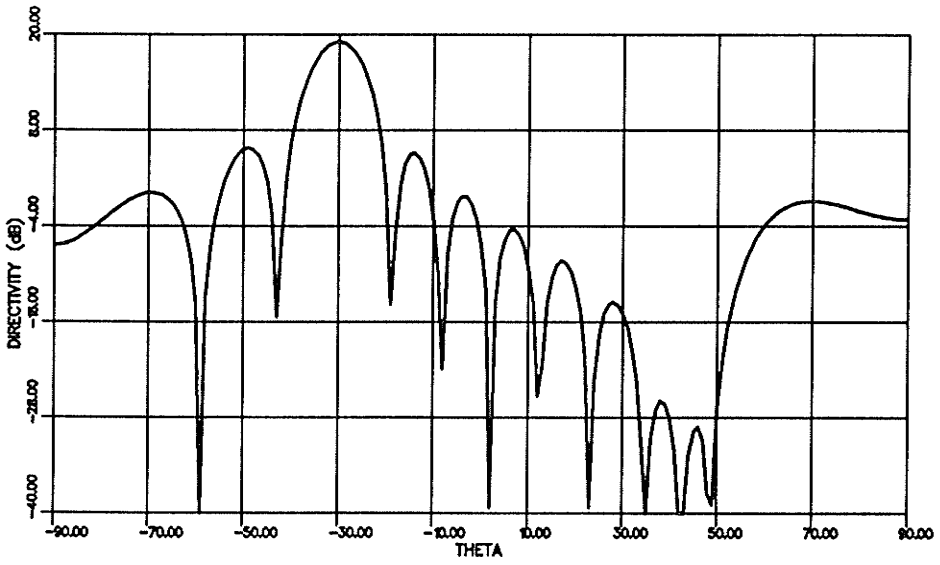

Figure 4.27: Dual mode 2×8 array scanned to $\phi = 270°$ and $\theta = 30°$ ($\phi = 90°$ *plane*)

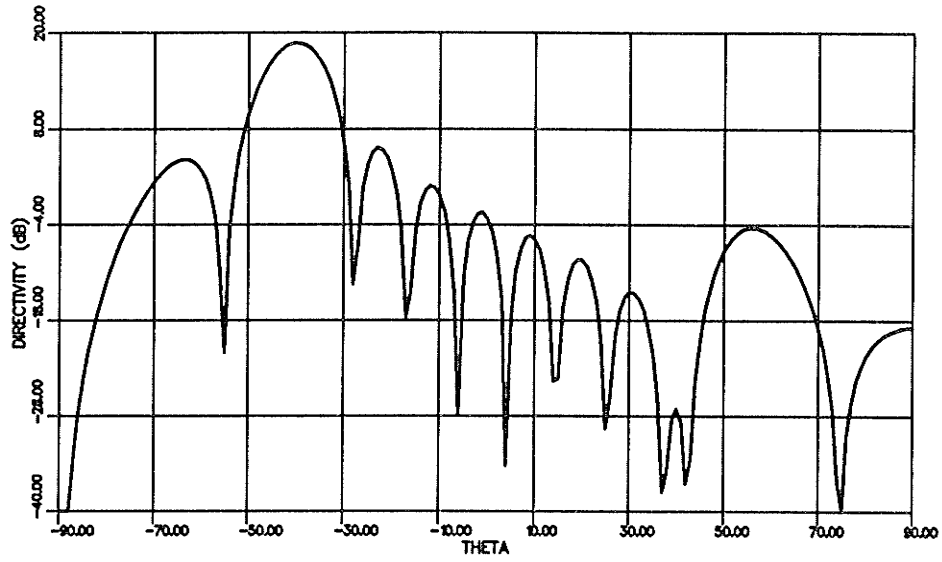

Figure 4.28: Dual mode 2×8 array scanned to $\phi = 270°$ and $\theta = 40°$ ($\phi = 90°$ *plane*)

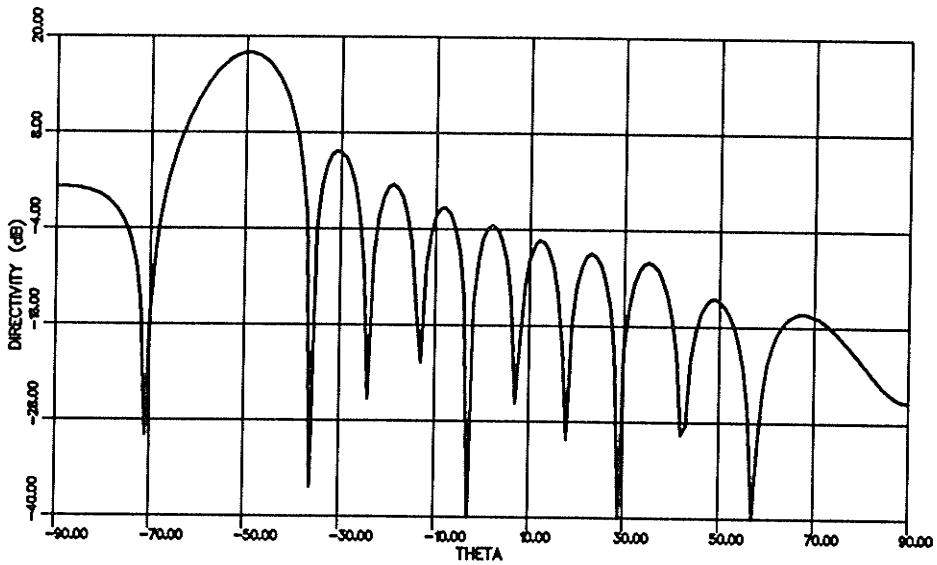

Figure 4.29: Dual mode 2×8 array scanned to $\phi = 270°$ and $\theta = 50°$ ($\phi = 90°$ *plane*)

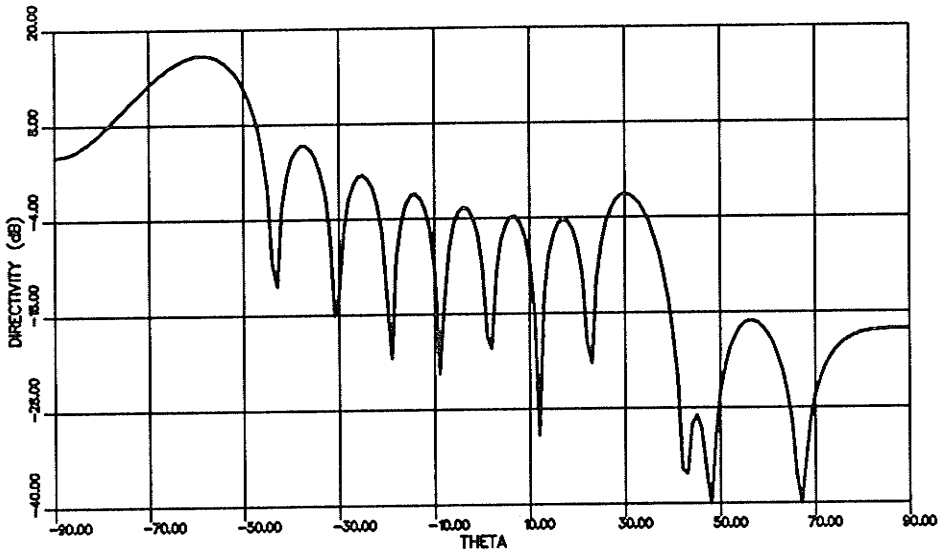

Figure 4.30: Dual mode 2×8 array scanned to $\phi = 270°$ and $\theta = 60°$ ($\phi = 90°$ *plane*)

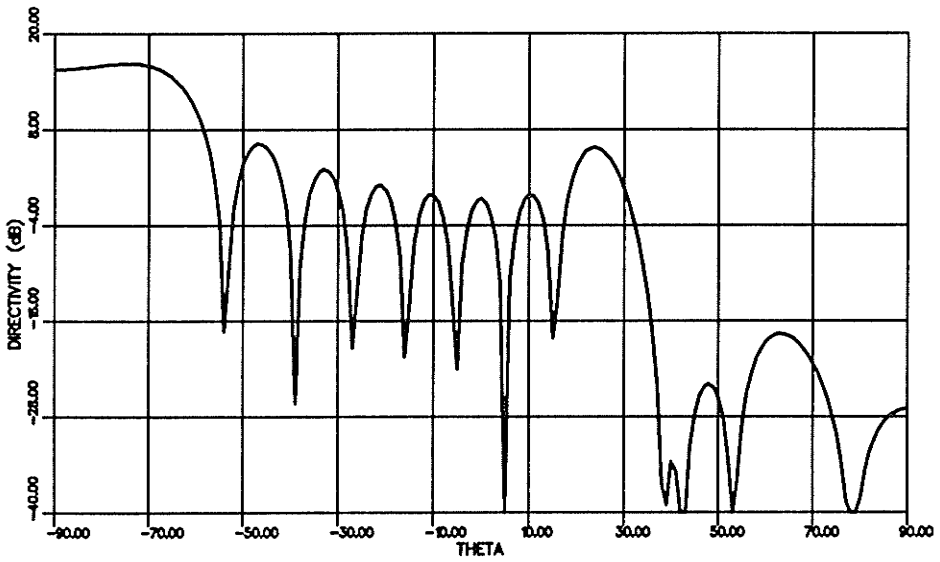

Figure 4.31: Dual mode 2×8 array scanned to $\phi = 270°$ and $\theta = 70°$ ($\phi = 90°$ *plane*)

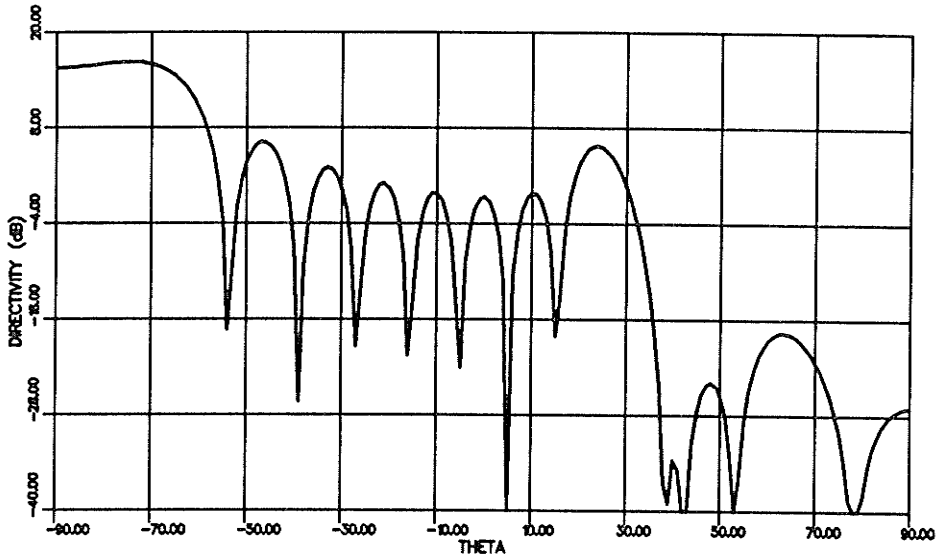

Figure 4.32: Dual mode 2×8 array scanned to $\phi = 270°$ and $\theta = 80°$ ($\phi = 90°$ *plane*)

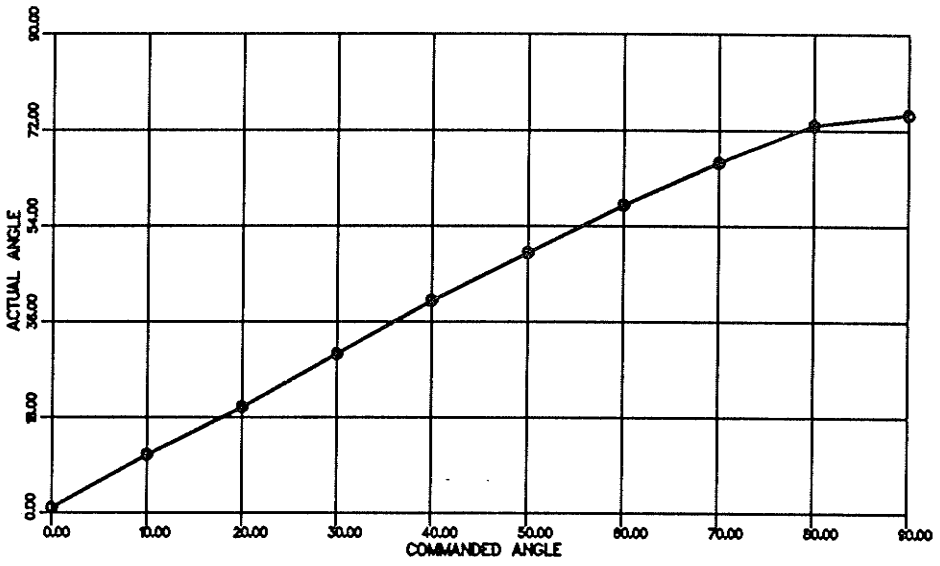

Figure 4.33: Actual versus commanded steering angle for a dual mode array with $dx = dy = .7\lambda$

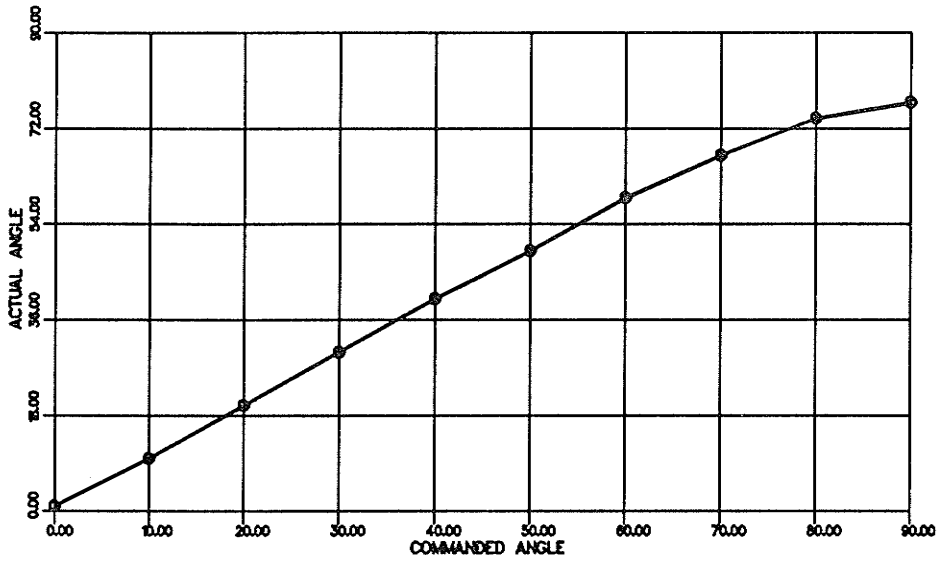

Figure 4.34: Actual versus commanded steering angle for a dual mode array with $dx = .7\lambda$, $dy = .8\lambda$

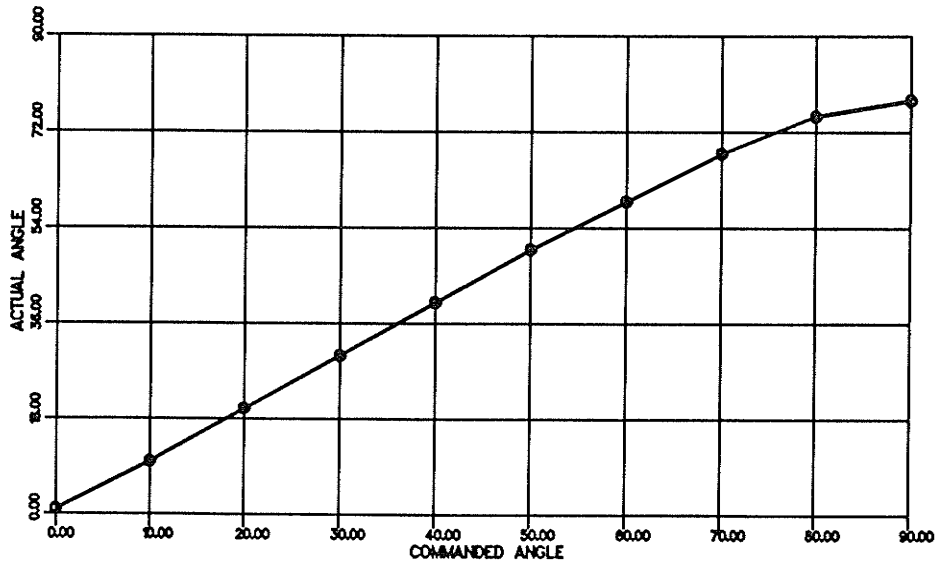

Figure 4.35: Actual versus commanded steering angle for a dual mode array with $dx = .7\lambda$, $dy = .9\lambda$

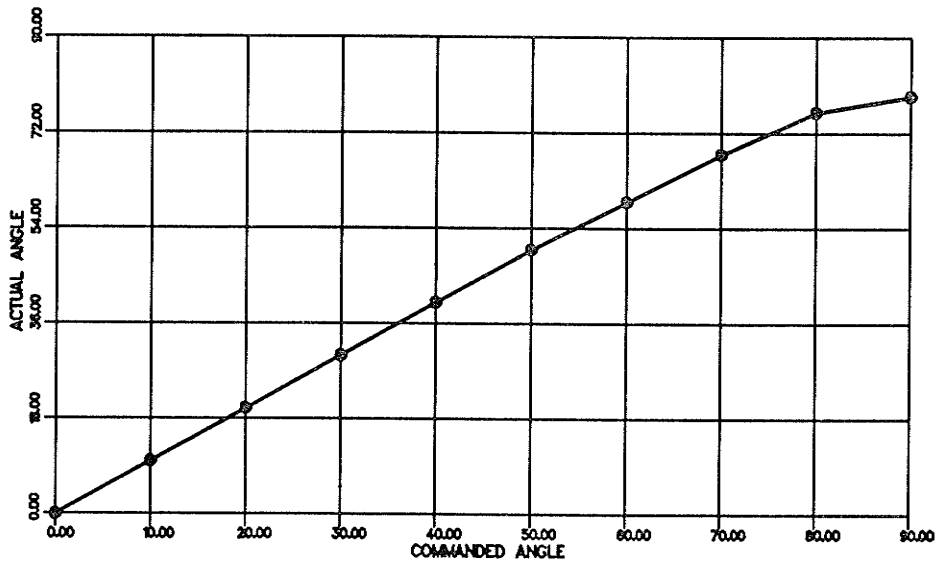

Figure 4.36: Actual versus commanded steering angle for a dual mode array with $dx = .7\lambda$, $dy = \lambda$

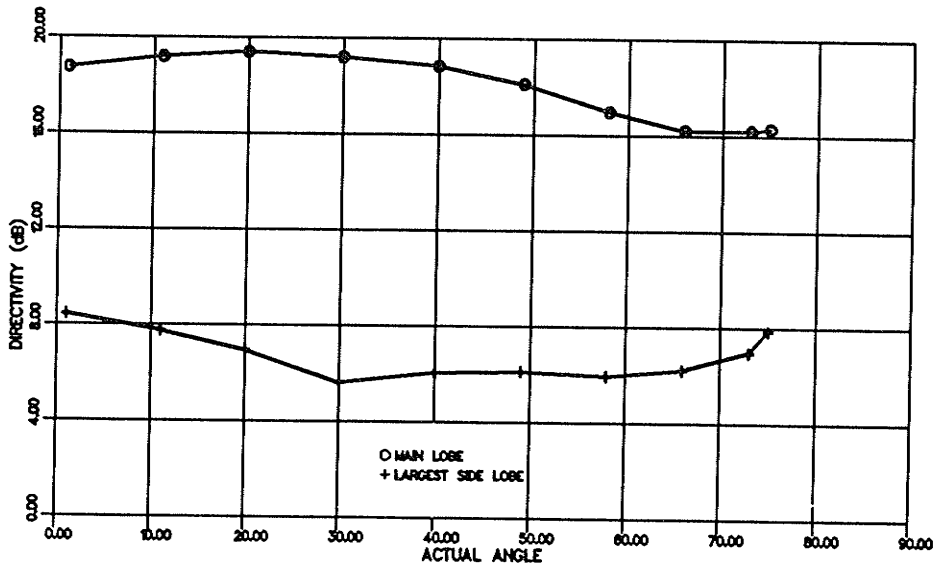

Figure 4.37: Gain versus actual steering angle for a dual mode array with $dx = dy = .7\lambda$

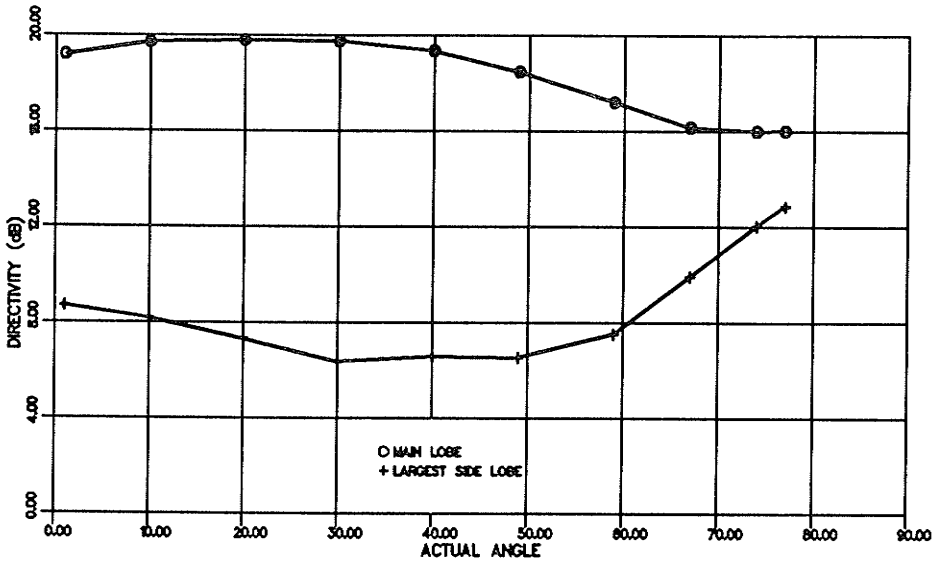

Figure 4.38: Gain versus actual steering angle for a dual mode array with $dx = .7\lambda$, $dy = .8\lambda$

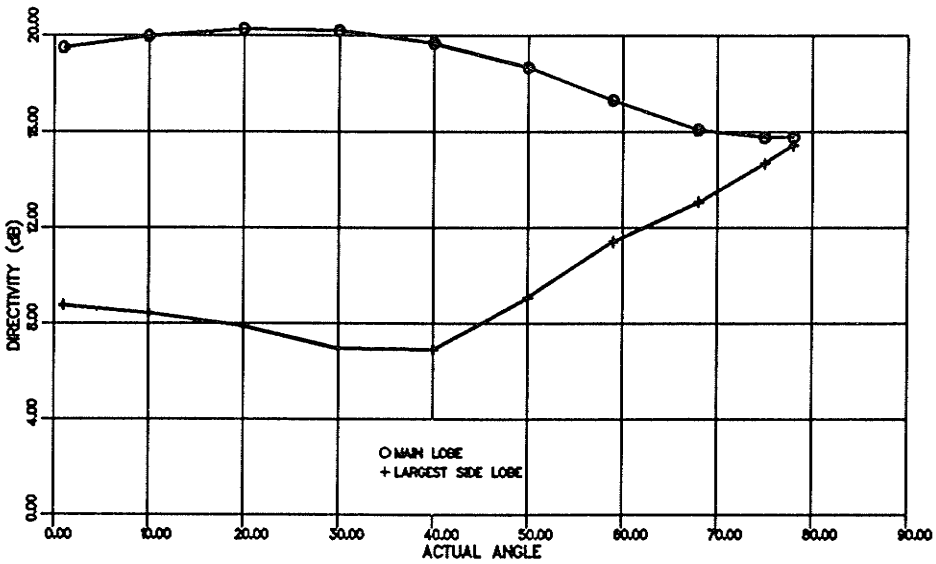

Figure 4.39: Gain versus actual steering angle for a dual mode array with $dx = .7\lambda$, $dy = .9\lambda$

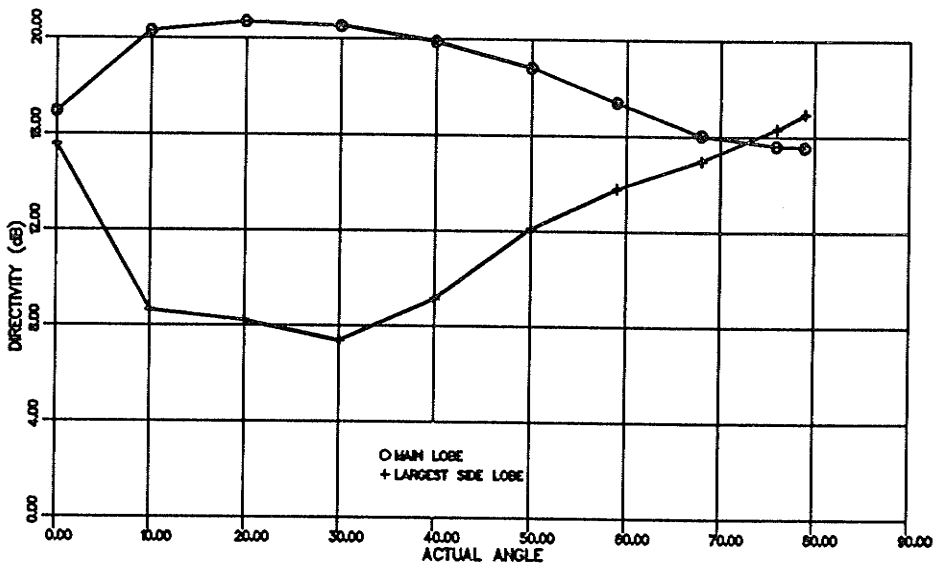

Figure 4.40: Gain versus actual steering angle for a dual mode array with $dx = .7\lambda$, $dy = \lambda$

4.3.3 TM_{11} 20 Element Configuration

The TM_{11} 2×10 configuration as shown in Figure 4.41, is similar to the TM_{11} 2×8 configuration with 2 columns of elements added at one end. The array is slightly smaller than the 2×8 dual mode array while still having a directivity similar to the 2×8 dual mode array at broadside. The scan angle and directivity characteristics of the TM_{11} 2×10 configuration are shown in Figures 4.42 and 4.43 respectively. At scan angles less than 55° the performance of this array is close to that of the dual mode array while at scan angles near endfire the dual mode array has much better performance due to its smaller grating lobes.

4.4 Array Feed Networks

4.4.1 TM_{11} Array

The TM_{11} mode 2×8 array is fed as shown in Figure 4.44. The input to the array is split 8-ways through the use of a corporate feed arrangement. The outputs of the 8-way power divider feed phase shifters which are used to control the scan angle of the array. Each phase shifter is connected to a 2-way power divider which in turn is connected to two 90° hybrids. These 90° hybrids are used to feed one column of the array consisting of two elements which are located next to each other in the x-direction. The actual gain of the 2×8 array will be approximately $3.5dB$ lower than its directivity if the losses shown in Table 4.1 are assumed. The power dividers, phase shifters and 90° hybrids can be integrated with the array and constructed on a dielectric substrate located behind the antenna elements.

The losses in the 20 element 2×10 array feed network would be slightly higher as the 10-way power divider would have higher losses than the 8-way power divider.

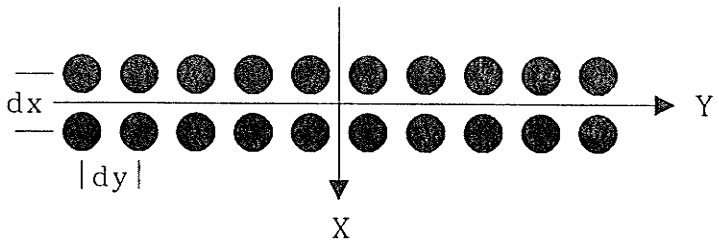

Figure 4.41: TM_{11} mode 2×10 array configuration

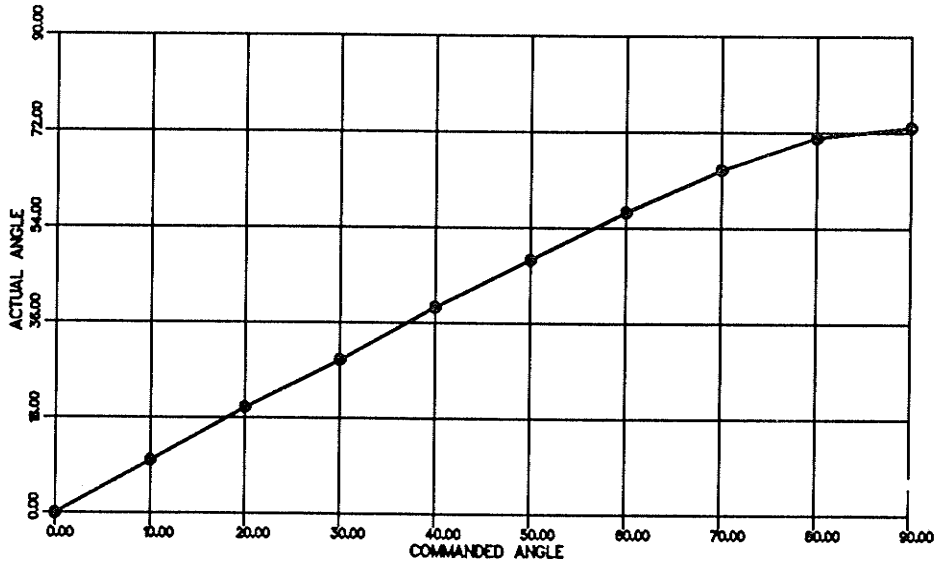

Figure 4.42: Actual versus commanded steering angle for a TM_{11} mode 2×10 array with $dx = dy = .5\lambda$

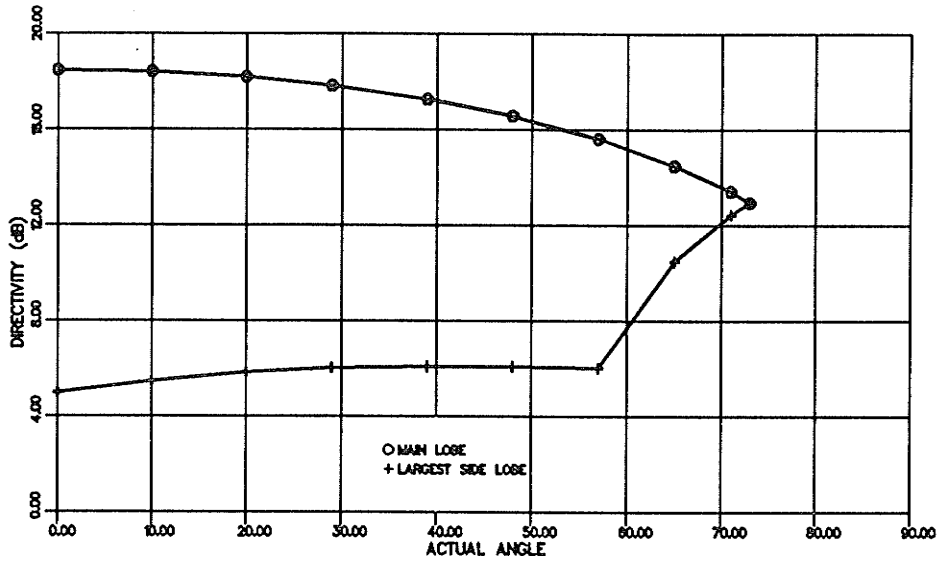

Figure 4.43: Gain versus actual steering angle for a TM_{11} mode 2×10 array with $dx = dy = .5\lambda$

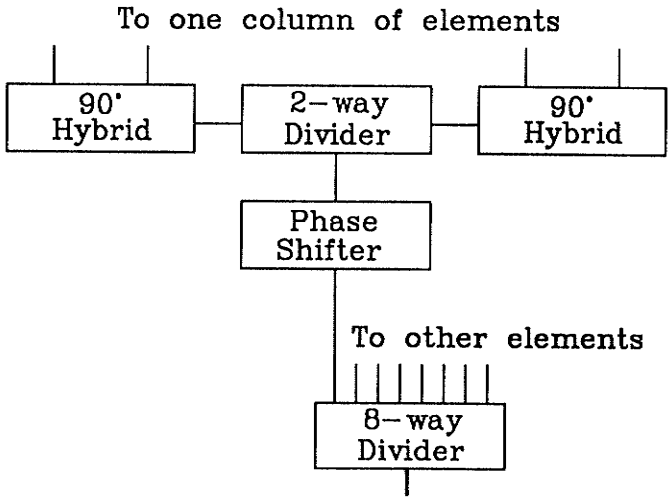

Figure 4.44: TM_{11} mode array feed network

8-way power divider	$.75dB$
Phase shifter	$2.0dB$
2-way power divider	$.5dB$
90° hybrid	$.25dB$
Total	$3.5dB$

Table 4.1: Losses in TM_{11} 2×8 array feed network

4.4.2 TM_{11} and TM_{21} 2×8 Array

The feed network for the dual mode 2×8 configuration is shown in Figure 4.45. The feed network is similar to that of the TM_{11} array where an 8-way power divider feeds phase shifters used to control the scan angle of the array. Each of these phase shifters is used to feed a 2-way power divider. One of the outputs of the power divider is connected to a phase shifter which is used to control the phase of the signal supplied to the TM_{21} mode elements. The phase shifter is switched to 0° when the antenna is steered in the $\phi = 270°$ direction and is switched to 180° when the antenna is steered in the $\phi = 0°$ direction. The remaining part of the feed network consists of 2-way power dividers and 90° hybrids which are used to feed the individual elements as in the case of the TM_{11} array. Each element pair in the TM_{11} and TM_{21} 2×8 array requires two extra 2-way power dividers, two extra 90° hybrids and an $0 - 180°$ phase shifter above that required by the TM_{11} mode array. This amounts to 5 more components for each element pair or 40 components for the TM_{11} and TM_{21} 2×8 array. The insertion loss of the dual mode array feed network would be approximately $1dB$ higher than that of the single mode feed network for a total of $4.5dB$.

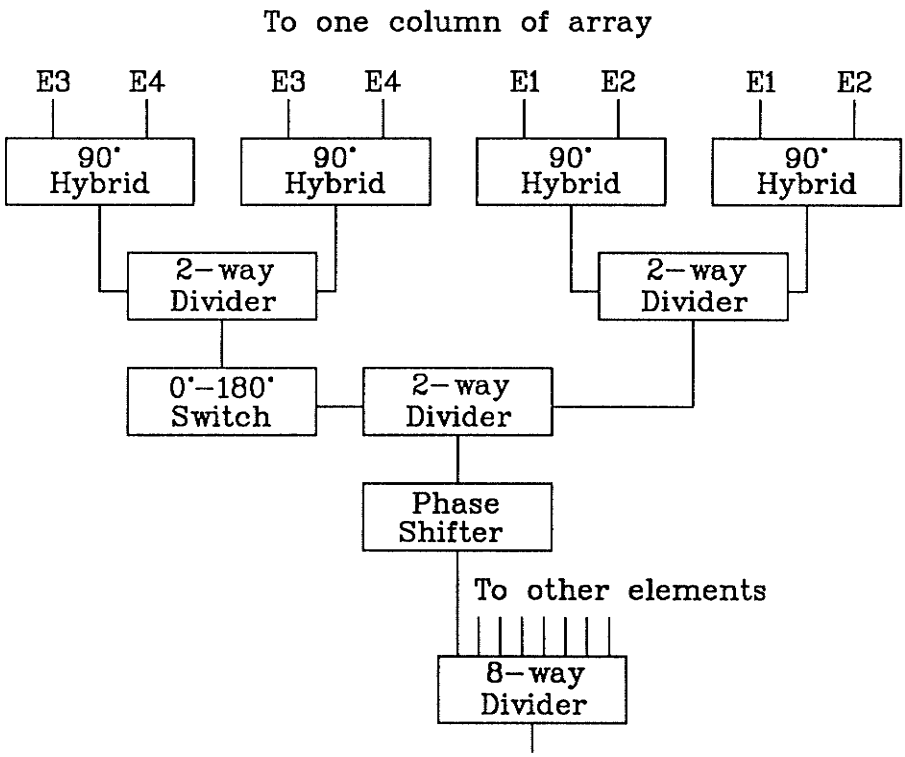

Figure 4.45: Dual mode array feed network

4.5 Array Steering Control

The main beam pointing direction is controlled by the relative phase delay inserted in the signal path to or from the elements in the array. The amount of phase delay inserted in the feed network of each element is determined by the range and resolution of phase delay available from each phase shifter and by the control logic executed by the array controller. The range of the phase shifter refers to the total phase shift available from the phase shifter. The resolution of the phase shifter refers to the smallest increment by which the phase can be varied. The arrays considered here require 17 steering positions; one at the broadside position and 8 positions on either side of the central position. The differential phase shift between adjacent elements, β, is related to the required steering angle from the endfire direction, θ_0, by;

$$\beta = -k_0 d \cos\theta_0 \tag{4.5}$$

Where k_0 is the free space wave number and d is the separation between elements in the array. Tables 4.2 and 4.3 list the steering angles available from 4-bit phase shifters with resolutions of 22.5° and 30° feeding arrays with elements spaced .5λ and .7λ respectively.

4.6 Array Size Estimates

As discussed at the beginning of this chapter the microstrip patch element analyzed in Chapter 3 does not have the directivity required to use it alone as an RPV data link antenna. In order to obtain the required gain the effective aperture of the antenna is increased by using a number of the patch elements in an array configuration. The approximate directivity of an array is related to the aperture of the array by [21]

$$G = 10log_{10}4\pi A \tag{4.6}$$

β	θ_0	β	θ_0
—	—	0.0	0.0
-22.5	82.82	22.5	97.18
-45.0	75.52	45.0	104.48
-67.5	67.98	67.5	112.02
-90.0	60.0	90.0	120.0
-112.5	51.32	112.5	128.68
-135.0	41.41	135.0	138.59
-157.5	28.96	157.5	151.04
-180.0	0.0	180.0	180.00

Table 4.2: Steering angles for an array with .5λ spacing and a 4-bit 22.5° resolution phase shifter

β	θ_0	β	θ_0
—	—	0.0	90.0
-30.0	83.16	30.0	96.84
-60.0	76.23	60.0	103.77
-90.0	69.08	90.0	110.92
-120.0	61.56	120.0	118.44
-150.0	53.47	150.0	126.53
-180.0	44.42	180.0	135.58
-210.0	33.56	210.0	146.44
-240.0	17.75	240.0	162.25

Table 4.3: Steering angles for an array with .7λ spacing and a 4-bit 30.0° resolution phase shifter

where A is the area of the array in $\lambda^2$and G is the gain of the array in dB. The approximate half-power beam width (HPBW) of an array is related to the length of the array in that direction by

$$\theta = \frac{57.3^\circ \lambda}{L} \tag{4.7}$$

where L is the length of the array in meters and θ is the HPBW of the antenna. To obtain a gain of $16dB$ as required for the RPV antenna the antenna is designed to have a directivity of $19dB$ to allow for $3dB$ of losses, therefore the effective aperture must be

$$19 = 10log_{10}4\pi A \tag{4.8}$$

$$A = 6.32 \tag{4.9}$$

If an array is built using two rows of dual mode elements spaced $.7\lambda$ apart then the vertical dimension of the array will be 1.3λ. The horizontal dimension of the array must then be at least 4.9λ in length. If the horizontal elements are also spaced $.7\lambda$ apart then a minimum of 7 horizontal elements are required. The arrays described in the previous sections had 8 or more columns to enable symmetric power splitting between the columns and to provide the extra gain required to compensate for any losses within the individual antenna elements.

Chapter 5

Experimental Results

5.1 Introduction

In order to verify the model for the dual mode circularly polarized antenna presented in Chapter 3 several antenna elements were fabricated. The impedance characteristics of the elements were measured and the elements were tuned to a common frequency. The tuning of the elements was done by modifying the radius of the radiating patch. The radiation patterns of the individual patches were measured along with the radiation patterns of a linear array of three patches.

The fabrication of these patches also provided insight into the added complexity of building the dual mode elements over that involved in building the single mode elements.

5.2 Element Design

The element design was based on the theoretical work presented in Chapter 3. The initial variables used in the design process are the desired frequency of operation f_r and the dielectric constant ϵ_r of the substrate used to fabricate

the elements. The design is carried out using the following steps;

1. The effective radius of the circular patch is given by [13];

$$a_e = \frac{k_{nm} a C}{2\pi f_r \sqrt{\epsilon_r}} \tag{5.1}$$

where the value of $k_{nm}a$ is given by Table 3.1 and C is the speed of light. Given a desired frequency of operation $f_r = 2360\ MHz$ and a substrate with a dielectric constant of $\epsilon_r = 2.5$ the effective radii of the patches are 2.356 cm and 3.908 cm for the TM_{11} and TM_{21} mode patches respectively.

2. The effective radius of the disk takes into account the fringe fields on the edge of the actual patch. The actual patch radius can be found by solving for a in the following equations[12];

$$\begin{aligned} a_e &= a(1+\Delta)^{\frac{1}{2}} \\ \Delta &= \frac{2h}{\pi \epsilon_r a}[\ln \frac{a}{2h} + 1.41\epsilon_r + 1.77 + \frac{h}{a}(.268\epsilon_r + 1.65)] \end{aligned}$$

The solution is obtained by iteratively choosing values for a and comparing the result for a_e with the one previously calculated. A new value for a is chosen by adding a correction factor based on the error in the value of a_e to the old value of a. In this case the resulting values of a are 2.209 cm and 3.750 cm for the TM_{11} and TM_{21} mode patches respectively.

3. The locations of the feed probes can be obtained using the impedance equations given in Chapter 3. To obtain an input resistance of 50 Ω the input probes would be located at radii of .47 cm and 1.4 cm for the TM_{11} and TM_{21} mode patches respectively.

The results obtained using the procedure outlined above are only approximate and provide a starting point for experimentally fine tuning the elements in the laboratory.

5.3 Element Fabrication

The elements were constructed on a sheet of 1.5875 *mm* Oak 601/GX substrate with a dielectric constant of 2.5. The TM_{11} mode elements were etched on the top surface of the laminate and identically sized patches were etched on the other side of the laminate directly under the upper patches. The outer conductors of the coaxial feeds for the TM_{11} mode elements are soldered to the patches on the rear side of the TM_{11} mode elements. These patches are used to ensure good contact with the top surface of the TM_{21} mode elements which are used as the ground plane for the TM_{11} mode elements. The TM_{21} mode elements are etched on the top surface of the substrate and the copper foil on the bottom side of the substrate is left for use as the ground plane. After the elements have been etched the individual elements are cut out and separated into sets of TM_{11} and TM_{21} mode elements for assembly. The sets of elements are aligned and holes are drilled for fasteners. The holes required for the coaxial feeds are located and drilled and the coaxial feed lines are soldered onto the antenna elements. The elements are then assembled into the completed dual mode antenna.

The fabricated patches had radii of 2.2 *cm* and 3.748 *cm* for the TM_{11} and TM_{21} mode patches respectively. The sizes of the actual patches differed slightly from the desired sizes due to inaccuracies in the photographic reduction of the artwork and in the etching process.

The TM_{11} mode feed point was located at a radius of .649 *cm* and the TM_{21} mode feed point was located at a radius of 1.85 *cm*.

5.4 Single Element

5.4.1 Input Characteristics

The input characteristics of a single element were measured using an HP8410 Network Analyzer. The approximate resonant frequencies of the radiating patches were measured as being 2421 MHz for the TM_{11} mode patch and 2373 MHz for the TM_{21} mode patch. The measured resonant frequency is slightly different from the calculated resonant frequency as the calculated value is based on the cavity resonance in the absence of feed probes. The measured resonant frequency is defined as the frequency where the antenna is best matched to a source impedance of 50 Ω.

In order to evaluate the dual mode elements a common operating frequency had to be found for all of the element feed points. It is difficult to change the resonant frequency of the TM_{21} mode elements as they are sandwiched between the two sheets of substrate. The operating frequency of the TM_{11} mode elements can be modified by changing the size of the exposed radiating patch. This is done by using copper tape to increase the size of the patch. Increasing the size of the patch lowers the resonant frequency of the patch. A common operating frequency of 2385 MHz was chosen as the operating frequency after measurements were made of all of the TM_{21} mode patch resonant frequencies.

After a series of trial and error experiments the TM_{11} mode patches were increased in size to 2.26 cm. The resulting resonant frequencies of the experimental dual mode antenna elements are shown in Table 5.1.

From this table it can be seen that the resonant frequencies of the individual inputs spanned a range from 2376 to 2389 MHz. Although the inputs of all of the elements could not be exactly tuned to 2385 MHz this frequency was still chosen as the common operating frequency. As shown in Table 5.2 all of the elements had reflection losses of at least -11.5 dB at this frequency. Figures 5.1 to 5.3 are plots of input frequency versus return loss for the three

Element Number	Input 1	Input 2	Input 3	Input 4
1	2381	2383	2381	2380
2	2376	2379	2381	2380
3	2384	2384	2388	2389

Table 5.1: Final experimental values of resonant frequency (MHz)

Element Number	Input 1	Input 2	Input 3	Input 4
1	-21.5	-19.0	-13.0	-19.5
2	-16.0	-18.0	-12.0	-15.0
3	-23.8	-18.0	-11.5	-15.0

Table 5.2: Return Loss (dB) at 2385 MHz

dual mode elements. From these figures it is evident that the TM_{11} mode patches were in general better matched than the TM_{21} mode patches. The bandwidth of the TM_{11} mode patches were also wider than that of the TM_{21} mode patches.

The variations in resonant frequency and return loss can be attributed to inaccuracies in the construction of the elements and to the placement of the feed probes. The TM_{11} mode patches were modified by covering the original etched patches with copper tape which was then cut in the shape of a circle with the aid of a sharp knife and a compass. This resulted in the new patches being slightly irregular in shape and not being perfectly circular as required. The irregular shape of the patches would cause the two inputs to the patch to have slightly different resonant frequencies. The two feed probes of each of the unmodified TM_{21} mode patches had very closely matched resonant frequencies with the differences probably due to measurement accuracy. The different values of return loss measured at the TM_{11} mode inputs are probably due to differences in feed probe location and in the quality of the feed probe

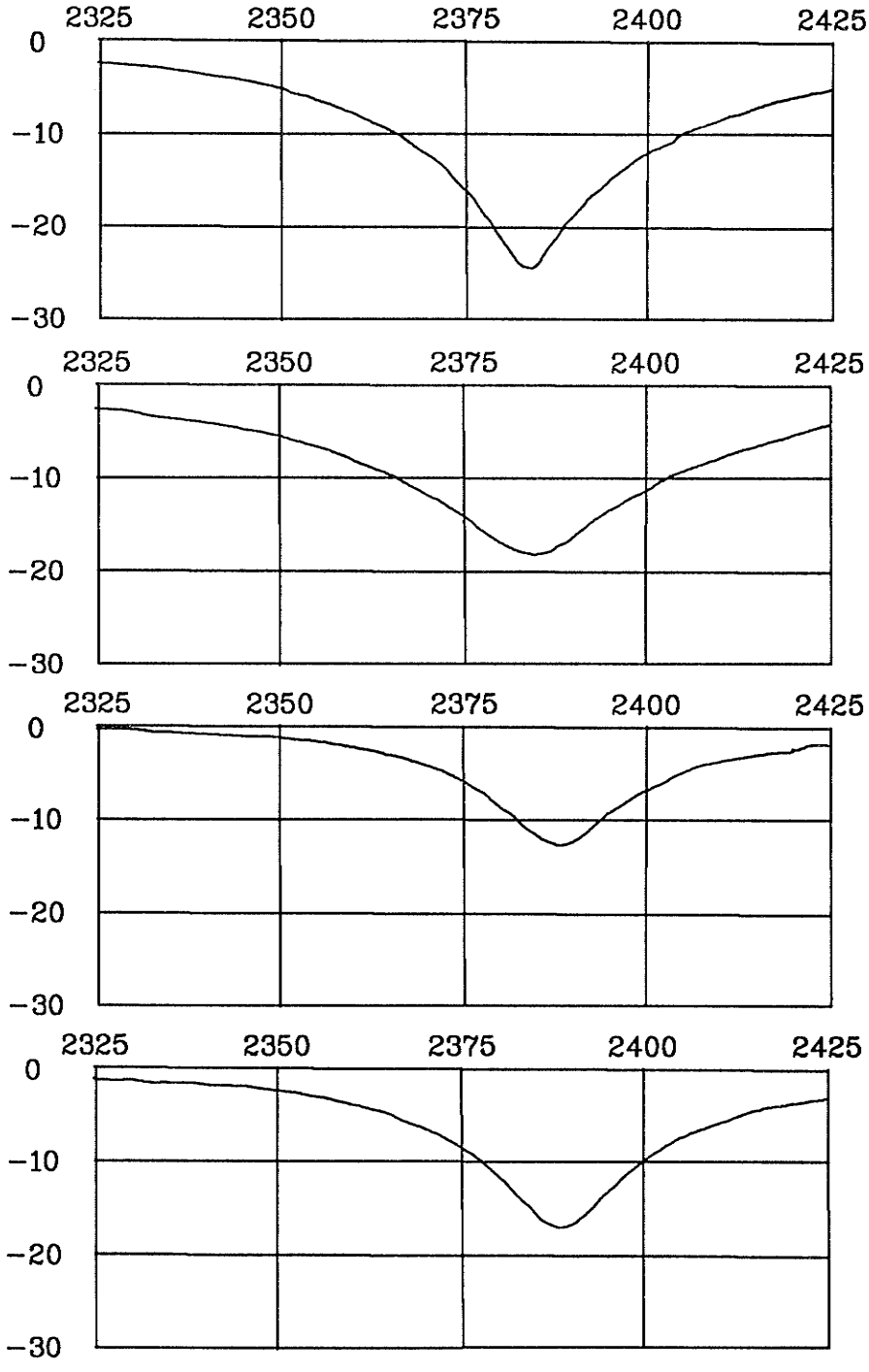

Figure 5.1: Element 1 return loss (in dB and MHz) (Inputs 1–4 from top to bottom)

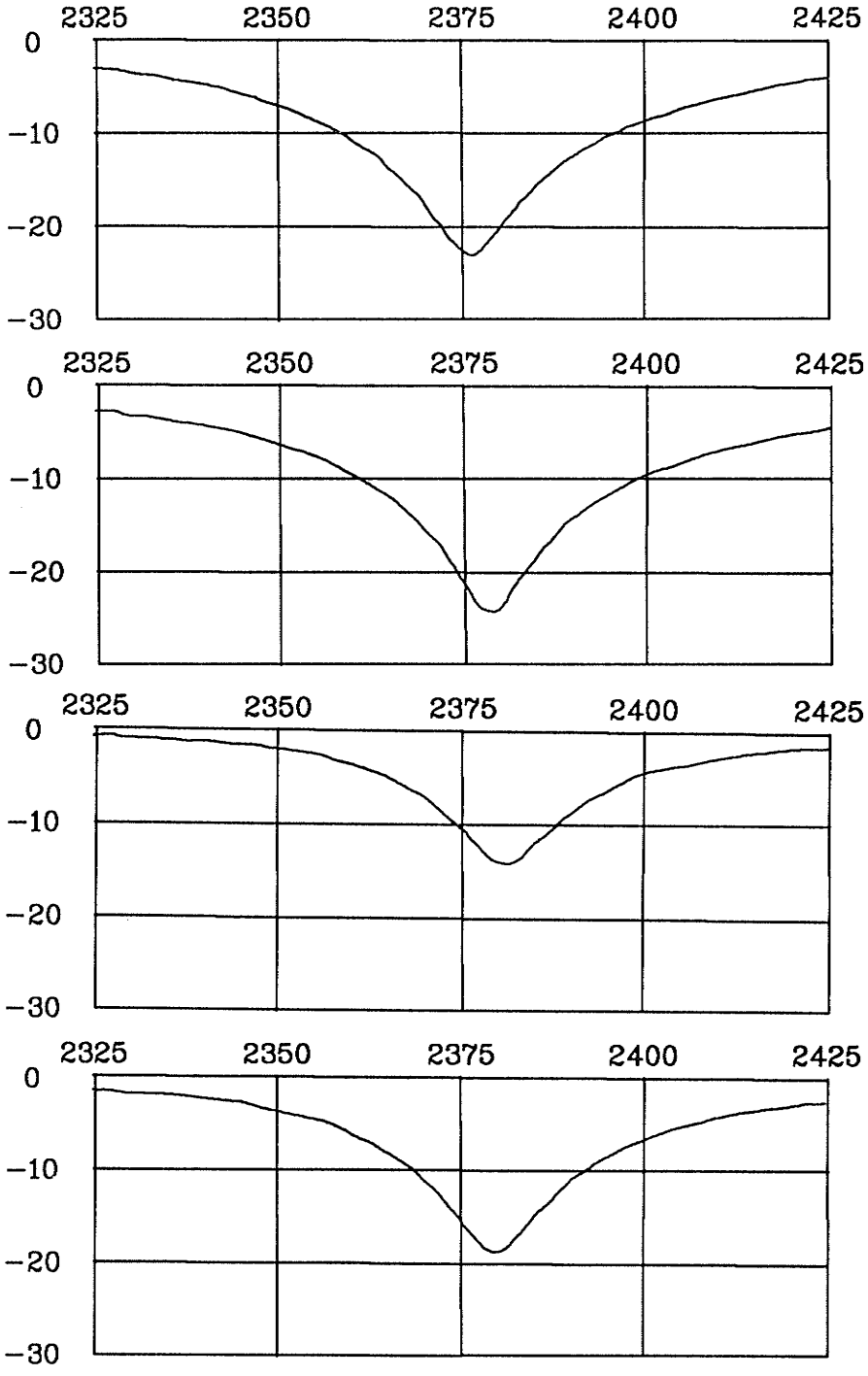

Figure 5.2: Element 2 return loss (in dB and MHz) (Inputs 1–4 from top to bottom)

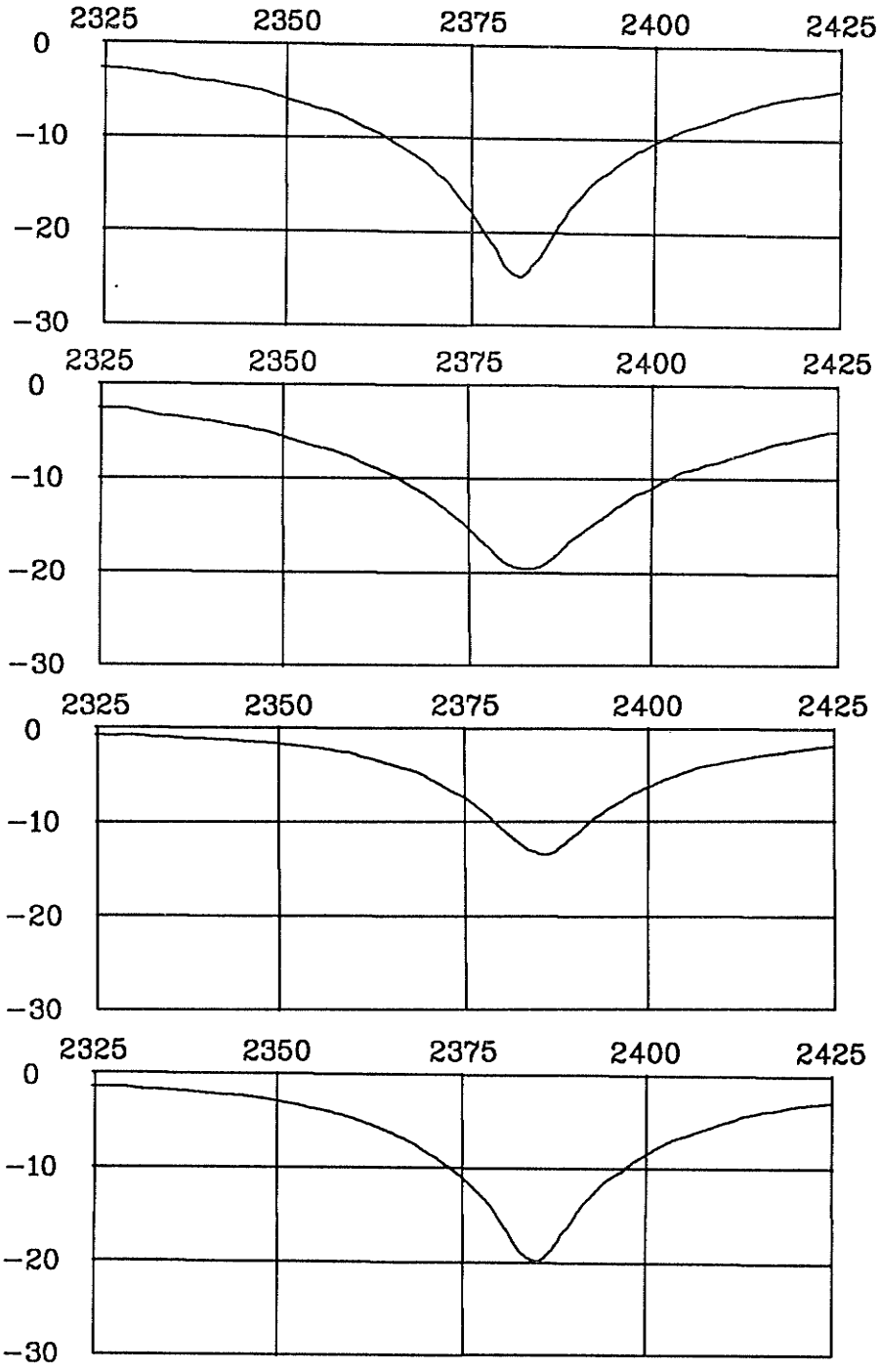

Figure 5.3: Element 3 return loss (in dB and MHz) (Inputs 1–4 from top to bottom)

Element Number	Input 1	Input 2	Input 3	Input 4
1	.031	.055	.223	.049
2	.118	.069	.283	.140
3	.018	.069	.319	.140

Table 5.3: Mismatch Loss (dB) at 2385 MHz

connection at the element. The feed probe consists of a short length of semi-rigid coax. The outer conductor of this cable is cut back to expose the centre conductor of the cable which is inserted in a hole in the element and soldered to the radiating patch. The outer conductor is soldered to the ground plane of the element. When these soldered connections are made the dielectric insulator in the cable expands and tends to push the connection apart. The break or separation in the connection causes a mismatch at the connection. This effect also exists at the connector end of the feed probe.

The larger values of return loss measured at the TM_{21} mode inputs are likely due to a poorer choice of feed probe location than in the TM_{11} mode case. Another factor may be the passage of the TM_{11} mode feed probes through the TM_{21} mode element.

The mismatch losses corresponding to the return losses shown in Table 5.2 are provided in Table 5.3. These values are used latter in this chapter to calculate the directivity of the test antennas.

5.4.2 Radiation Pattern

Radiation patterns of the individual elements were recorded in the anechoic chamber. A rotating linear element was used to illuminate the antenna under test. The resulting radiation patterns are shown in Figures 5.4 through 5.6. The measured gain of the antennas is referenced to that of a calibrated horn antenna. The recorded patterns are similar in shape to the theoretical patterns

generated in Chapter 3. Differences between the theoretical and measured patterns can be attributed to many sources some of which are, the use of a finite ground plane, and the uneven excitation of the feed probes due to poor matching. The elements have axial ratios (AR) of between 1.5 dB and 2.0 dB at the predicted beampeak position of $\theta = 32°$. The existence of these high axial ratios is to be expected for the same reasons that the measured patterns are not identical with the theoretical patterns.

The theoretical results obtained in Chapter 3 predict that the elements should have a directivity of 7.82 dB at $\theta = 32°$. The feed network used during the testing of the individual elements is shown in Figure 5.7. The directivity of the test elements can be calculated from the radiation pattern plots generated by the rotating linear antenna source antenna plus the specifications of the feed network components. The axial ratio of the test element can be read directly from the radiation pattern plot as the distance between the maximum and minimum values of the sawtooth shaped data curve at the desired angle. The maximum values of the sawtooth curve represent the major axis of the polarization ellipse which is equal to the sum of the copolar and cross-polar components of the field. The minimum values of the sawtooth curve represent the minor axis of the polarization ellipse which is equal to the difference of the copolar and cross polar components of the field. The peak gain of element 1 occurs at $\theta = 24°$ and the axial ratio at this point is approximately 2.6 dB as shown in Figure 5.4. To obtain the directivity of the antenna in terms of the right hand circular or left hand circular components the use of a polarization correction factor is necessary. The polarization correction factor is given by

$$L_{pc}(dB) = 6.02 - 20\log\left(1 + \frac{1}{AR}\right) \tag{5.2}$$

A further correction denoted by L_p of 3.01 dB must be added to the test data to compensate for the use of the linear source antenna with a circularly polarized test antenna. Table 5.4 lists the location and magnitude of the peak

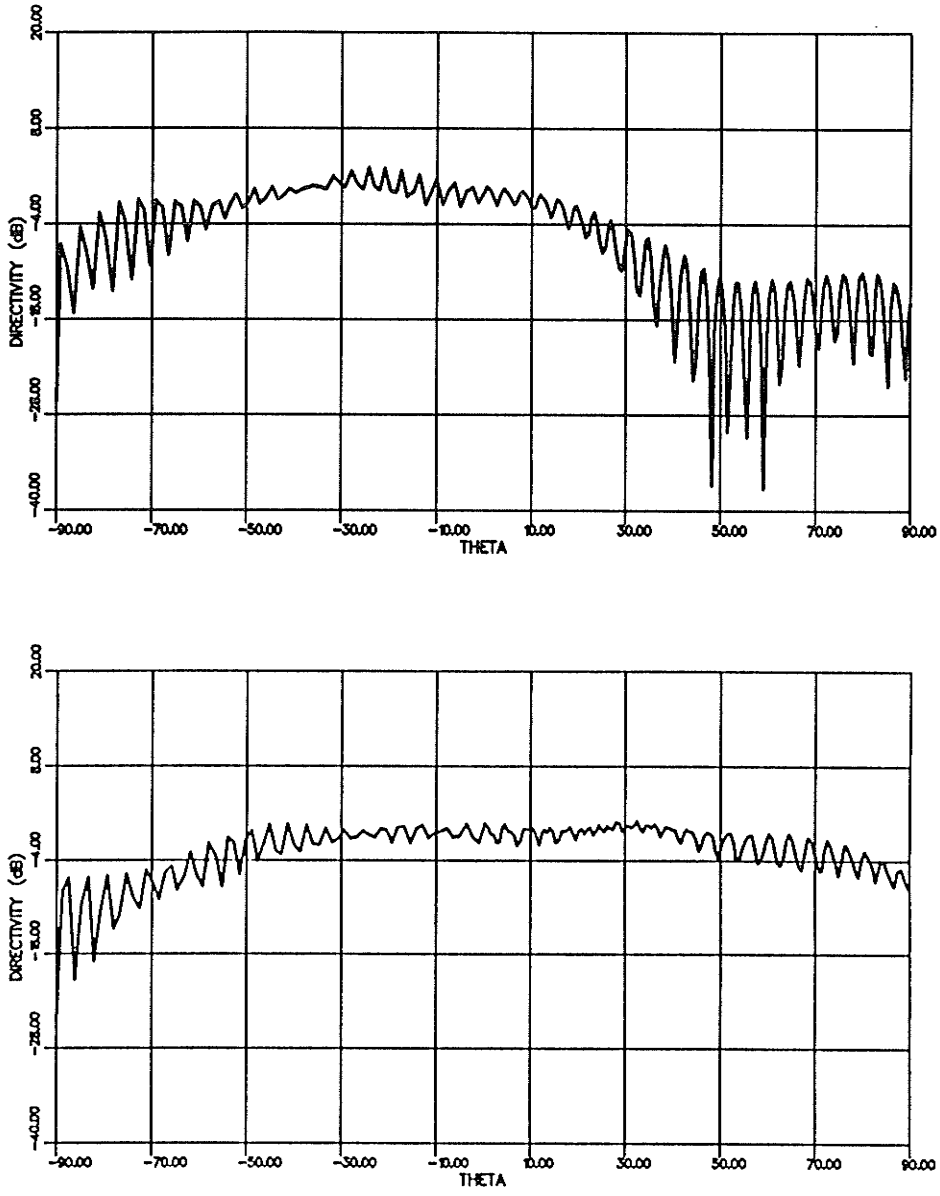

Figure 5.4: Element 1 radiation pattern, Top:$\phi = 90°$ plane, Bottom:$\phi = 0°$ plane

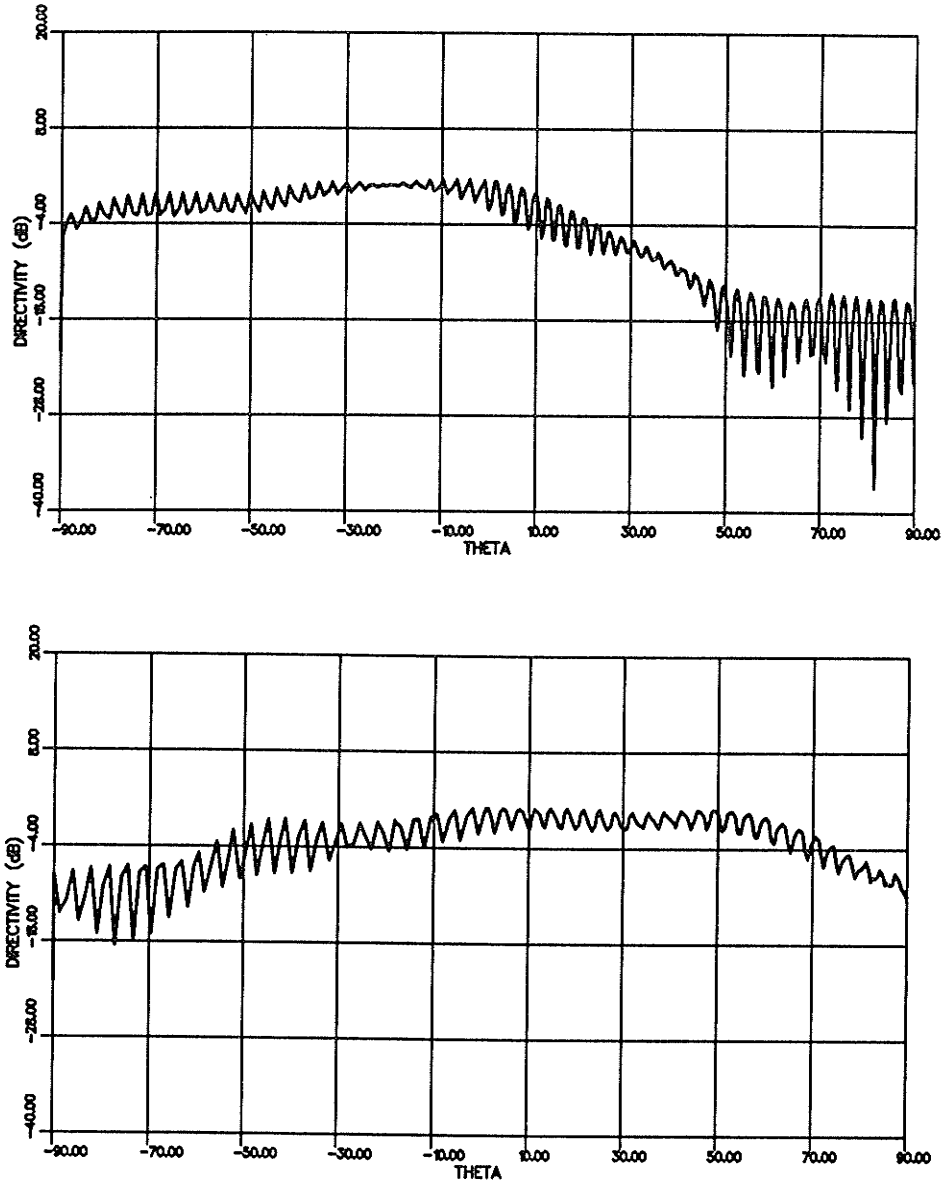

Figure 5.5: Element 2 radiation pattern, Top:$\phi = 90°$ plane, Bottom:$\phi = 0°$ plane

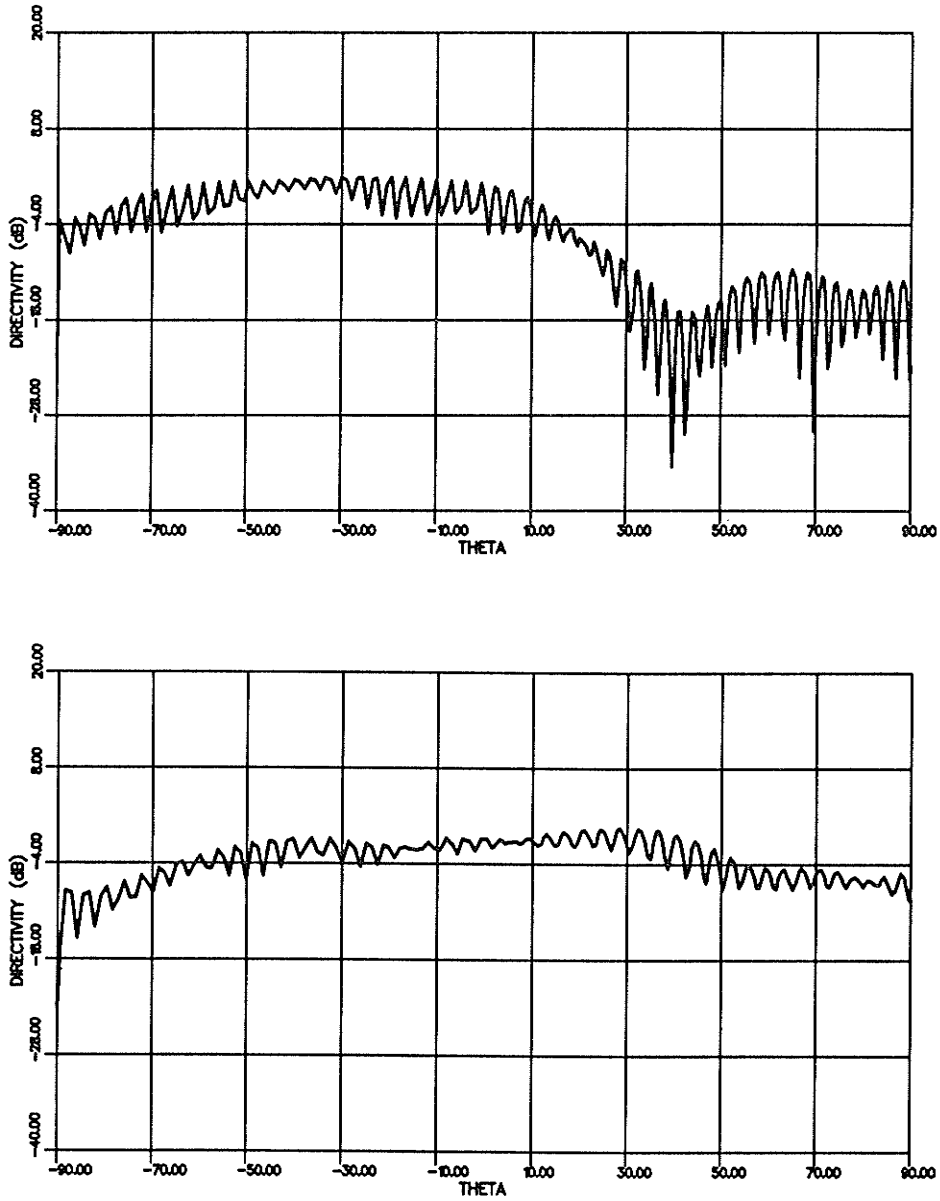

Figure 5.6: Element 3 radiation pattern, Top:$\phi = 90°$ plane, Bottom:$\phi = 0°$ plane

Element Number	Gain(dB)	$\theta°$	AR	L_{pc}
1	3.09	24	2.5	1.16
2	1.66	12	1.5	.72
3	1.96	24	2.0	.94

Table 5.4: Polarization correction factor at the peak gain position of the individual elements

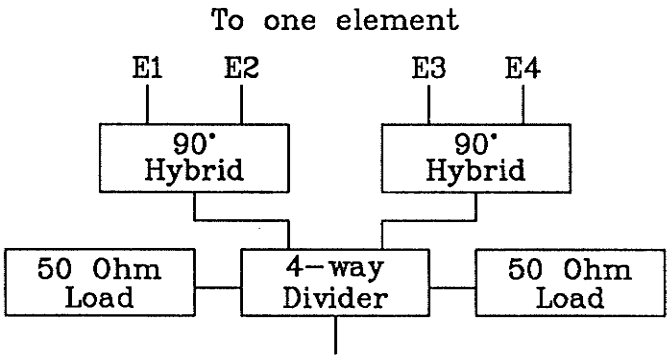

Figure 5.7: Single element feed network

gain and the corresponding axial ratio along with the polarization correction factor for each of the elements. The value of the peak gain location for element 2 is misleading as the actual test pattern has a wide almost level section from $\theta = 36°$ to $\theta = 0°$. At $\theta = 21°$ the gain of the element is less than 1 dB down from the peak with an axial ratio of nearly zero. This results in the gain being nearly equal to the peak gain when the polarization correction factor is included.

To obtain the directivity of the antenna the losses due to the feed network must also be included. The specifications of the feed network components are given in Table 5.5. The insertion loss of the feed network is approximately 1.1 dB if .1 dB is allowed for losses in the cable. A further 3 dB loss occurs as a result of substituting a 4-way power divider for the required 2-way power

Component	Manufacturer and Model	Insertion Loss
4-way Power Divider	Mini-Circuits ZA4PD-4	.50 dB
90° Hybrid	ARRA 4164-90	.25 dB

Table 5.5: Feed network component specifications

Element	Gain (dB)
1	8.78
2	7.79
3	7.87

Table 5.6: Directivity of the test elements (dB)

divider. The unused ports of the 4-way power divider were terminated in matched loads. The directivities of the test elements with all of the losses and correction factors included are shown in Table 5.6. The directivities obtained are higher than those calculated previously in Chapter 3. The increase in directivity is again likely attributable to the finite ground plane used and to distortions in the predicted pattern caused by uneven excitation at the 4 feed probes.

5.5 Array

5.5.1 Introduction

A three element linear array with an inter-element separation of .7 λ was built using the three elements described in the previous section. The array was tested in the anechoic chamber and radiation patterns were obtained with the array steered in the broadside direction and 30°, 60°, and 80° from broadside.

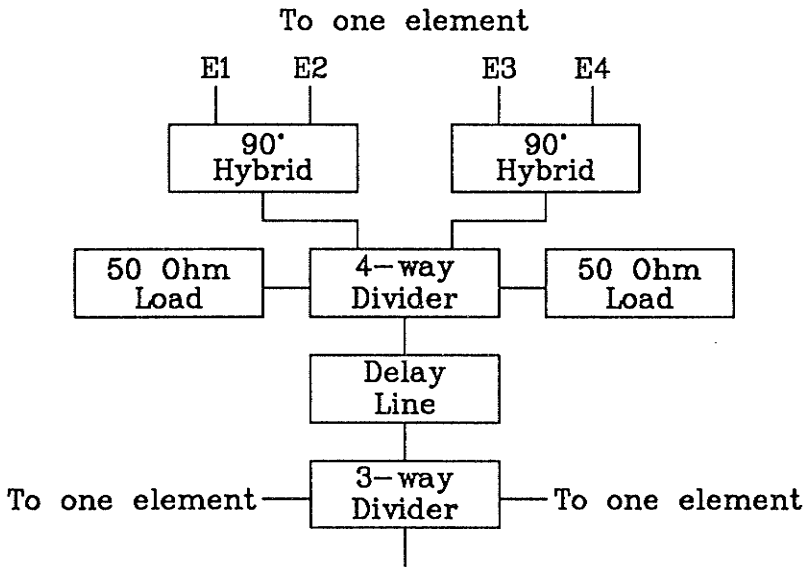

Figure 5.8: Three element array feed network

These angles were chosen to allow observation of the performance of the array over a large range of steering angles within the limited time available. The feed network used for the three element array is shown in Figure 5.8.

5.5.2 Radiation Patterns

The array was steered by introducing phase shifts into the feed paths of the individual elements as required. This was accomplished through the use of sections of semi-rigid coax which had been cut to the required length. The length of the cable required for a particular phase shift is determined by the following relationship

$$L_c = \frac{P_{hase\ shift}}{360^o} \frac{V_p\ C}{f} \tag{5.3}$$

L_c is the length of the cable required to introduce a phase shift of $P_{hase\ shift}$ degrees at a frequency equal to f. C is the speed of light and V_p is the velocity of propagation in the cable. Tables 5.7 and 5.8 list the phase shifts required

Steering Angle	Element 1	Element2	Element 3
0°	0	0	0
30°	0	126	252
60°	0	218.25	436.5
80°	0	252	504

Table 5.7: Phase shifts required to steer antenna to 30°, 60°, and 80° from broadside.

Steering Angle	Element 1	Element2	Element 3
0°	0	0	0
30°	0	3.055	6.11
60°	0	5.29	10.58
80°	0	6.11	12.22

Table 5.8: Cable lengths (cm) required to steer antenna to 30°, 60°, and 80° from broadside.

at each element and the length of cable required to steer the array to 30°, 60°, and 80° from broadside.

The calculated and measured radiation patterns of the three element array are shown in Figures 5.9 to 5.12. The overall shape of the experimental patterns matches that of the calculated patterns. The deep nulls of the theoretical patterns are not reflected in the experimental data. This effect may be due to several factors, the effects of mutual coupling between elements, the use of a finite ground plane, and the differences in pattern between the individual elements used in the array. The radiation patterns of the individual elements did not match each other or the predicted radiation pattern exactly so it is not surprising that the array patterns are not exactly as predicted.

The directivity of the array can be obtained in the same fashion as that of the individual elements. There is additional loss in the feed network due to the

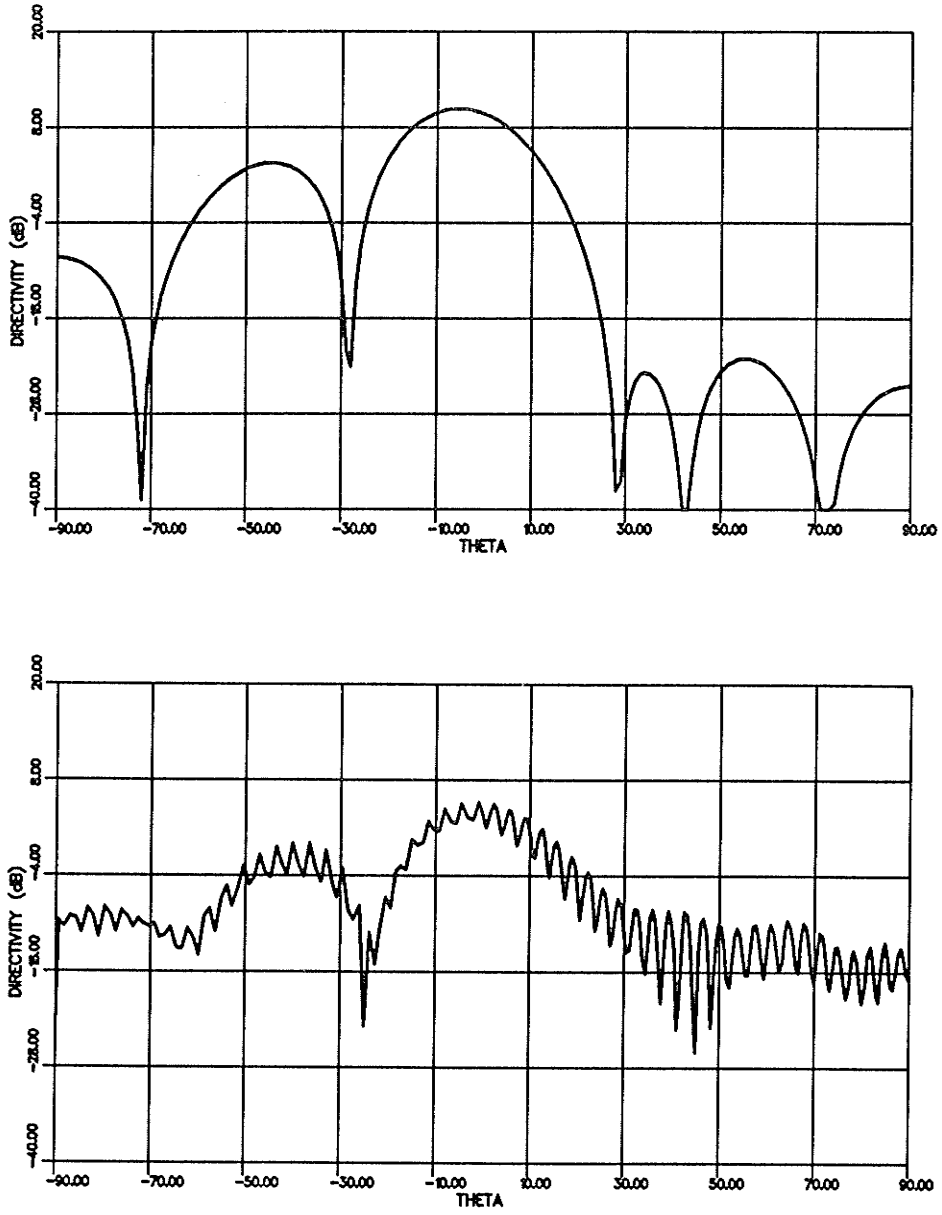

Figure 5.9: Radiation pattern of the 3 element array steered to $\phi = 270°$, $\theta = 0°$. (Top: Calculated, Bottom: Measured)

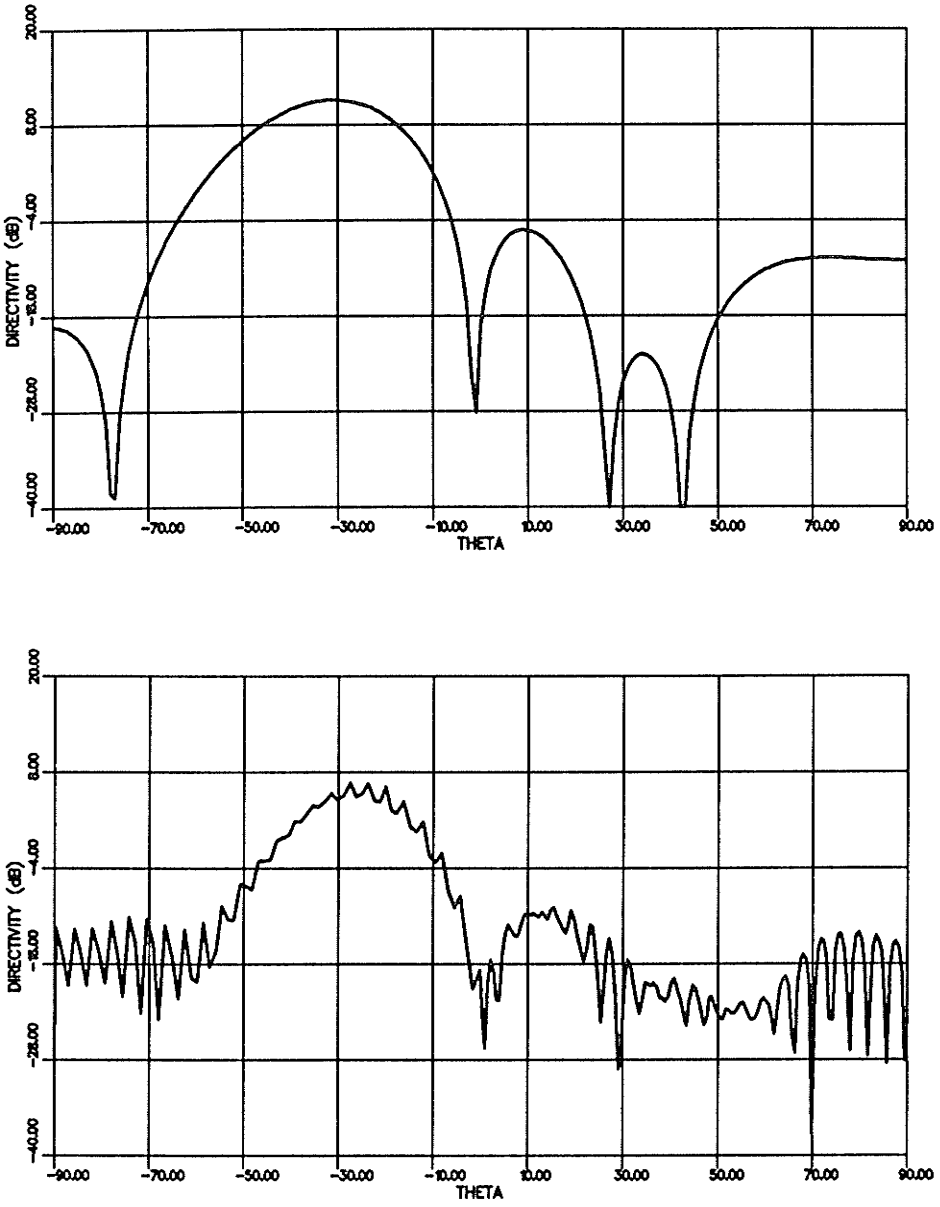

Figure 5.10: Radiation pattern of the 3 element array steered to $\phi = 270°$, $\theta = 30°$. (Top: Calculated, Bottom: Measured)

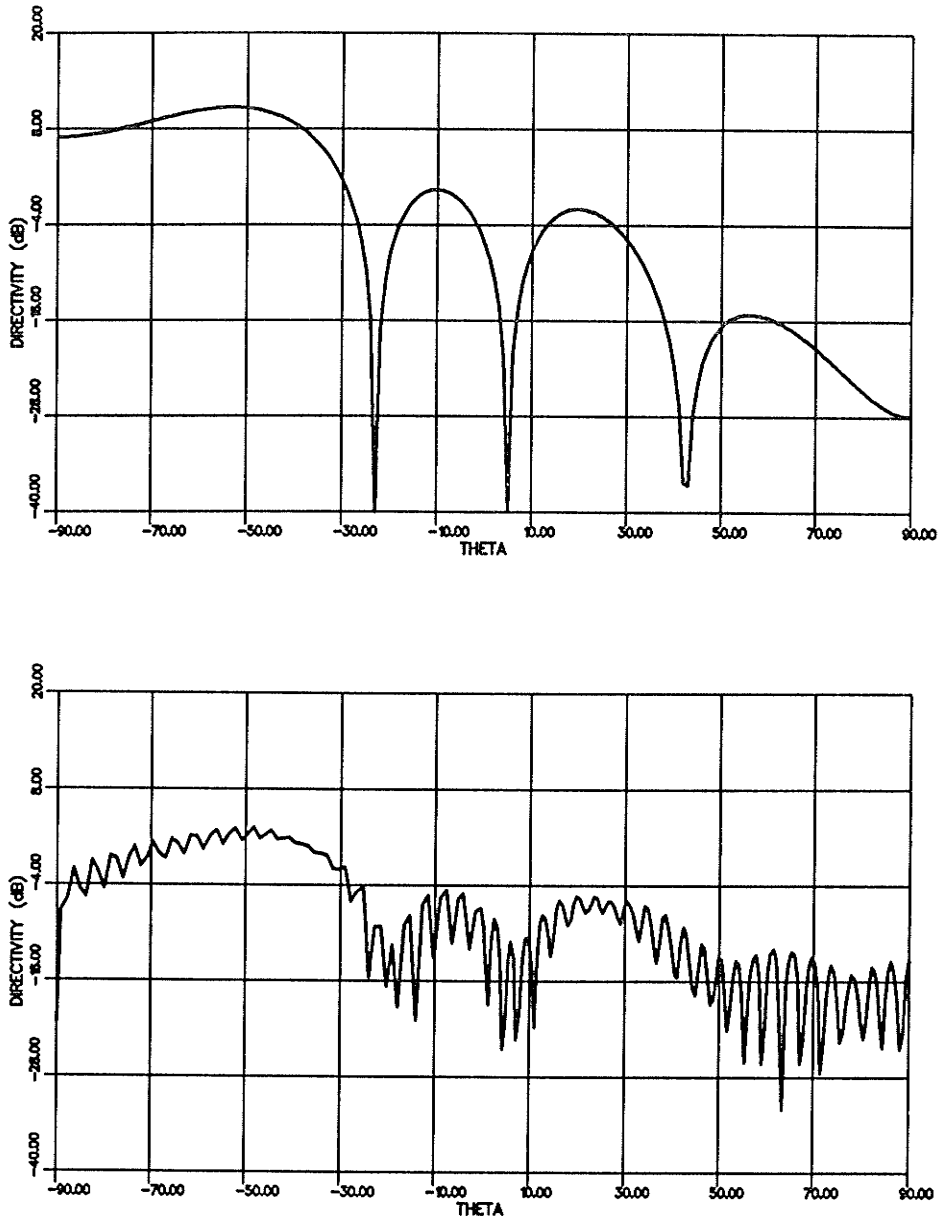

Figure 5.11: Radiation pattern of the 3 element array steered to $\phi = 270°$, $\theta = 60°$. (Top: Calculated, Bottom: Measured)

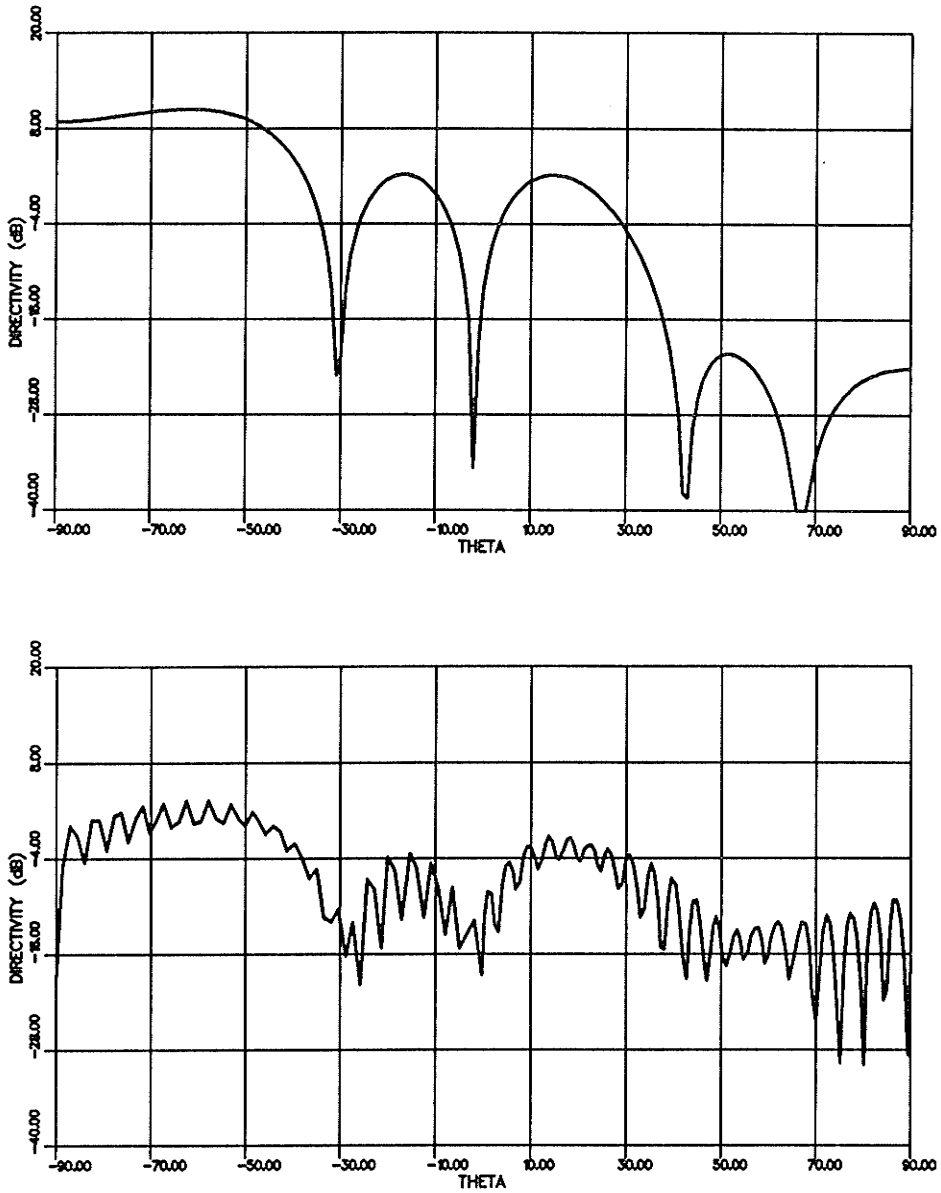

Figure 5.12: Radiation pattern of the 3 element array steered to $\phi = 270°$, $\theta = 80°$. (Top: Calculated, Bottom: Measured)

Steering Angle	Actual Angle	Directivity (dB)
0°	1	11.8
30°	28	13.4
60°	51	10.2
80°	60	9.3

Table 5.9: Commanded steering angle versus actual angle and directivity.

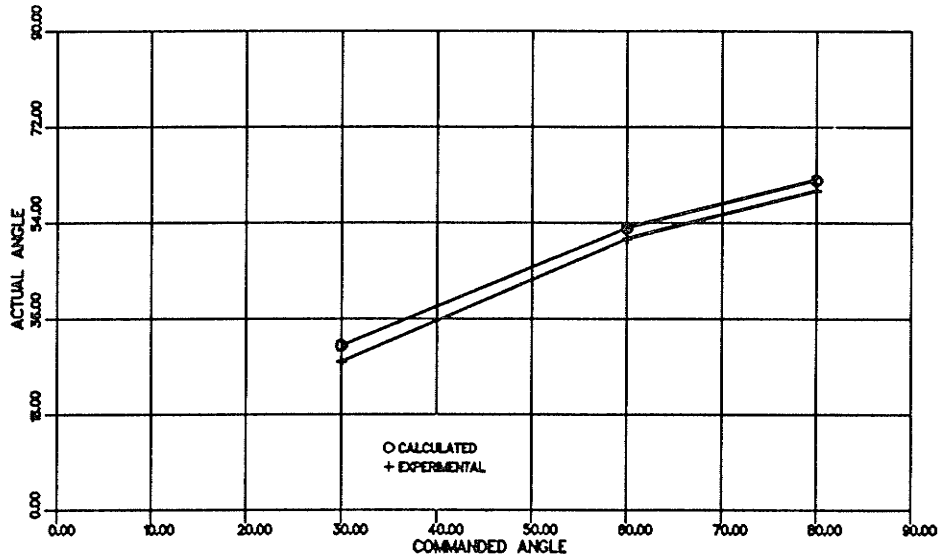

Figure 5.13: Commanded versus actual steering angle for the three element array

extra cabling and the three way power divider used in the array. The insertion loss of the three way power divider is approximately .75 dB and insertion loss of the extra cables is assumed to be .1 dB. Table 5.9 shows the commanded steering angle of the array and the actual angle and magnitude of the peak directivity. This data is also shown graphically along with the predicted values in Figures 5.13 and 5.14.

The overall performance of the experimental array is similar to that obtained theoretically.

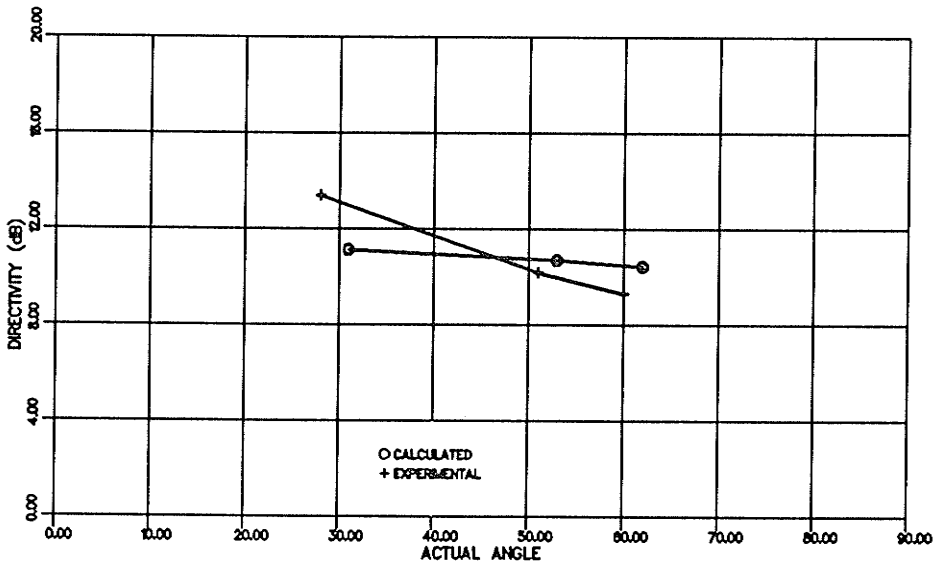

Figure 5.14: Gain versus actual steering angle for the three element array

Chapter 6

Conclusions

6.1 Summary

The first chapter presented background material on the use of RPVs. RPVs represent a large investment for many military and civilian organizations. As such they require reliable control and data links to monitor the performance of the vehicle and to obtain data from onboard sensors.

The second chapter presented the selection criteria for the RPV downlink antenna and the reasons why a microstrip array was chosen. A microstrip array was chosen as microstrip antenna elements are thin, lightweight, and can be made conformal to the fuselage of an RPV. Once designed microstrip antennas are relatively simple to fabricate and install on an RPV.

The third chapter presented analytical analyses of circular patch microstrip antennas operating in various modes and combinations of modes. The far-field radiation patterns of TM_{11}, TM_{21}, and dual mode elements were derived. Background material on polarization and directivity was presented along with equations for the input impedance of circular patch microstrip antennas.

The fourth chapter began with a short review of array theory which was then applied to three different array configurations. The performance of the

three arrays was then examined. The feed networks required for the arrays were described and the calculations used to determine the required size of arrays were presented.

The fifth chapter described the experimental work which was done in support of this project. The experimental work consisted of building three circular patch microstrip elements and testing them both individually and in a three element configuration.

6.2 Study Results

Of the three array configurations examined in Chapter 4 only the dual mode array had a directivity, not including losses, of at least $16dB$ over the entire commanded scan angle range from broadside to endfire. The directivity of the TM_{11} mode arrays fell below $16dB$ between actual scan angles of 45° to 53° when commanded to high scan angles from broadside. The directivity of the TM_{11} mode arrays could be increased by adding more elements to the arrays, however, the directivity would still drop off sharply at high scan angles due to the energy contained in the grating lobes. The use of the dual mode element in the array reduces the influence of the grating lobes as the element pattern is much lower in the direction of the grating lobes.

If endfire operation is not required and the array is only required to scan to approximately 50° from broadside then the use of TM_{11} elements in the array is desirable. The TM_{11} mode elements are much simpler to fabricate and the whole array including the feed network can be built on a single sheet of substrate material. An array utilizing dual mode elements would require two sheets of substrate material to be etched, aligned and fastened together. The more complex feed network could still be constructed on the substrates, however, feed throughs would be required to connect to the upper elements. The extra material and labor involved would make the finished antenna much

more expensive to produce than a single mode array.

The feed networks used in both the single and dual mode arrays could be greatly simplified through the use of an element which only required a single feed point to produce circularly polarized radiation. The elliptical microstrip antenna described by Shen [23] might be a suitable element. This would reduce the number of 90° hybrids required by the array.

6.3 Recommendations For Future Study

As noted in the previous section, the use of a different element should be investigated to simplify the design of the feed networks. The new element should also have a higher operational bandwidth. The bandwidth of the elements used in this thesis was suitable for this particular application, however higher bandwidths will be required in the future.

This study has not included the effects of mutual coupling or the size of the ground plane on the performance of the array. Future studies should include these effects to obtain better predictions of the performance of the array. All of the models in this thesis assumed that the array was uniformly excited. Future studies should examine the effect of tapering the excitation to improve the performance of the array.

To completely verify the performance of the dual mode array a full size model should be fabricated and tested. The array could be tested in both the laboratory and on an RPV in an operational environment. The predicted performance of the array suggests that it may be a viable antenna for use on an RPV.

Appendix A

Data Link Calculations

To determine the gain required for the RPV data link antenna it was necessary to perform a data link budget analysis. The following parameters were used to estimate the performance of the system.

Operating Frequency	f
Transmitter power	P_T
Transmitter System Losses	L_T
Transmitter Antenna Gain	G_T
Transmission Loss	L_{FS}
Multipath Loss	L_M
Receiver Antenna Gain	G_R
Receiver System Losses	L_R
Receiver System Temperature	T_S
Receiver System Bandwidth	B_{IF}
Required Signal to Noise	S/N
Boltzmann's Constant	k

The required gain is then given by

$$G_T = \frac{S/N L_T L_M k T_S B_{IF} L_S}{G_R P_T} \tag{A.1}$$

f	2360 MHz
P_T	5 Watt
L_T	1 dB
L_{FS}	138 dB
L_M	15 dB
G_R	16 dB
L_R	1 dB
T_S	25 dBK
B_{IF}	73 dBHz
S/N	15 dB
K	-198.6 dB

Table A.1: RPV system parameters

The values used for the link analysis in Equation A.1 are shown in Table A.1. The antenna gain is calculated to be $15.7dB$. The actual antenna must have a higher directivity than this to compensate for the efficiency of the antenna system.

Appendix B

Derivation of the Far Field Radiation Patterns

The electric far field patterns due to electric and magnetic current sources are calculated in the following manner [12] [20]. The geometry utilized in the derivation is shown in Figure B.1.

B.1 Vector Potentials

B.1.1 Magnetic Vector Potential

The magnetic vector potential $\bar{A}$ is given by

$$\bar{A} = \frac{\mu}{4\pi} \int_0^h \int_0^{2\pi} \bar{J} \frac{e^{-jkR}}{R} a \, d\phi' \, dz' \tag{B.1}$$

where $\bar{J}$ is an electric surface current over the surface at

$$0 \leq z \tag{B.2}$$

$$z \leq h \tag{B.3}$$

$$x'^2 + y'^2 = a^2 \tag{B.4}$$

$$\theta' = 90^\circ \tag{B.5}$$

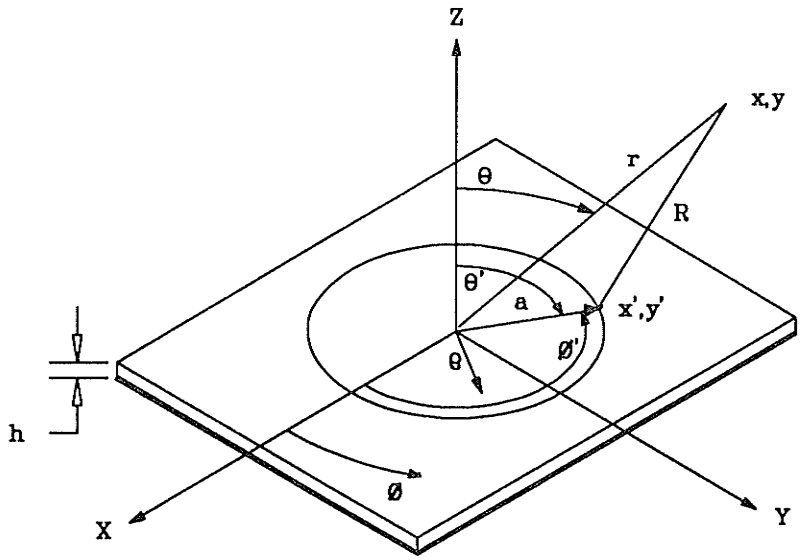

Figure B.1: Geometry of the Circular Patch Microstrip Antenna

$$|R| = \sqrt{r^2 - a^2 - 2ra\sin\theta\cos(\phi - \phi')} \tag{B.6}$$

for $r \gg a$

$$|R| \simeq \sqrt{r^2 - 2ra\sin\theta\cos(\phi - \phi')} \tag{B.7}$$

using the binomial expansion and keeping the first two terms leaves

$$|R| \simeq r - a\sin\theta\cos(\phi - \phi') \tag{B.8}$$

for phase terms and

$$|R| \simeq r \tag{B.9}$$

for amplitude terms.

The electric current source can be assumed to be approximated by a line current if $h \ll \lambda$ leaving

$$\bar{I}_a^e = 2H_\phi \hat{z} \tag{B.10}$$

where

$$H_\phi = -y_a E_a \cos n\phi' \tag{B.11}$$

The magnetic vector potential is given by

$$\bar{A} = \frac{\mu a h}{4\pi} \int_0^{2\pi} \bar{J} \frac{e^{-jkR}}{R} d\phi' \tag{B.12}$$

this current is transformed from cylindrical coordinates tc spherical coordinates using the following transformation

$$\begin{bmatrix} T_r \\ T_\theta \\ T_\phi \end{bmatrix} = \begin{bmatrix} \sin\theta\cos(\phi-\phi') & \sin\theta\sin(\phi-\phi') & \cos\theta \\ \cos\theta\cos(\phi-\phi') & \cos\theta\sin(\phi-\phi') & -\sin\theta \\ -\sin(\phi-\phi') & \cos(\phi-\phi') & 0 \end{bmatrix} \begin{bmatrix} T_x \\ T_y \\ T_z \end{bmatrix} \tag{B.13}$$

This results in a line current

$$\bar{I}_\theta^e = 2y_a E_a \sin\theta \cos n\phi' \hat{\theta} \tag{B.14}$$

Equation B.12 can be written as

$$A_\theta = \frac{\mu a h y_a E_a}{2\pi} \frac{e^{-jkr}}{r} \sin\theta \int_0^{2\pi} \cos n\phi' e^{jka\sin\theta\cos(\phi-\phi')} d\phi' \tag{B.15}$$

Using the following change of variables

$$\phi'' = \phi - \phi' \tag{B.16}$$

$$d\phi'' = -d\phi' \tag{B.17}$$

and by letting

$$C = \frac{\mu a h y_a E_a}{2\pi} \frac{e^{-jkr}}{r} \sin\theta \tag{B.18}$$

Equation B.15 becomes

$$A_\theta = -C \int_{\phi-0}^{\phi-2\pi} \cos n(\phi-\phi'') e^{jka\sin\theta\cos\phi''} d\phi'' \tag{B.19}$$

Using another change of variables,

$$\phi''' = -\phi'' \tag{B.20}$$

$$d\phi''' = -d\phi'' \tag{B.21}$$

leaves

$$A_\theta = C \int_0^{2\pi} \cos n(\phi + \phi''') e^{jka \sin\theta \cos\phi'''} \, d\phi''' \tag{B.22}$$

After using the following relationships [22]

$$\pi j^n J_n(z) = \int_o^{\pi} \cos(n\phi) e^{jz\cos\phi} \, d\phi \tag{B.23}$$

and

$$J_n(-z) = (-1)^n J_n(z) \tag{B.24}$$

the equation for A_θ becomes

$$A_\theta = j^n \mu a h y_a E_a \frac{e^{-jkr}}{r} J_n(ka \sin\theta) \sin\theta \, \text{ccs} \, n\phi \tag{B.25}$$

B.1.2 Electric Vector Potential

The magnetic current source can be assumed to be approximated by a line current if $h \ll \lambda$ leaving

$$\bar{I}_a^m = 2E_z \hat{\phi} \tag{B.26}$$

where

$$E_z = E_a \cos n\phi' \tag{B.27}$$

The electric vector potential is given by

$$\bar{F} = \frac{\epsilon a h}{4\pi} \int_0^{2\pi} \bar{M} \frac{e^{-jkR}}{R} \, d\phi' \tag{B.28}$$

This current is transformed from cylindrical coordinates to spherical coordinates using the transformation given in equation B.13. This results in the line current components given by

$$\bar{I}_\theta^m = 2E_a \cos\theta \sin(\phi - \phi') \cos n\phi' \hat{\theta} \tag{B.29}$$

and

$$\bar{I}_\phi^m = 2E_a \cos(\phi - \phi') \cos n\phi' \hat{\phi} \tag{B.30}$$

therefore

$$F_\theta = \frac{\varepsilon a h E_a}{2\pi}\frac{e^{-jkr}}{r}\cos\theta\int_0^{2\pi}\sin(\phi-\phi')\cos n\phi' e^{jka\sin\theta\cos(\phi-\phi')}\,d\phi' \quad \text{(B.31)}$$

Using the following change of variables

$$\phi'' = \phi - \phi' \quad \text{(B.32)}$$

$$d\phi'' = -d\phi' \quad \text{(B.33)}$$

and by letting

$$C = \frac{\varepsilon a h E_a}{2\pi}\frac{e^{-jkr}}{r}\cos\theta \quad \text{(B.34)}$$

Equation B.31 becomes

$$F_\theta = -C\int_{\phi-0}^{\phi-2\pi}\sin\phi''\cos n(\phi-\phi'')e^{jka\sin\theta\cos\phi''}\,d\phi'' \quad \text{(B.35)}$$

After the following change of variables

$$\phi''' = -\phi'' \quad \text{(B.36)}$$

$$d\phi''' = -d\phi'' \quad \text{(B.37)}$$

the equation for F_θ becomes

$$F_\theta = -C\int_{\phi-0}^{\phi-2\pi}\sin\phi''(\cos n\phi''\cos n\phi + \sin n\phi''\sin n\phi)e^{jka\sin\theta\cos\phi''}\,d\phi'' \quad \text{(B.38)}$$

The first term of the integral has a value of zero due to the multiplication of odd and even functions, leaving

$$F_\theta = -C\int_{\phi-0}^{\phi-2\pi}\sin\phi''\sin n\phi''\sin n\phi e^{jka\sin\theta\cos\phi''}\,d\phi'' \quad \text{(B.39)}$$

$$F_\theta = C\frac{\sin n\phi}{2}\int_0^{2\pi}(\cos(n-1)\phi'' - \cos(n+1)\phi'')e^{jka\sin\theta\cos\phi''}\,d\phi'' \quad \text{(B.40)}$$

After using the relationships in Equations B.23 and B.24 the equation for F_θ becomes

$$F_\theta = j^{n-1}\varepsilon a h\frac{E_a}{2}\frac{e^{-jkr}}{r}(J_{n-1}(ka\sin\theta) + J_{n+1}(ka\sin\theta))\cos\theta\sin n\phi \quad \text{(B.41)}$$

similarly F_ϕ is derived as follows

$$F_\phi = \frac{\varepsilon a h E_a}{2\pi} \frac{e^{-jkr}}{r} \int_0^{2\pi} \cos(\phi - \phi') \cos n\phi' e^{jka \sin\theta \cos(\phi - \phi')} \, d\phi' \tag{B.42}$$

Changing variables

$$\phi'' = \phi - \phi' \tag{B.43}$$

$$d\phi'' = -d\phi' \tag{B.44}$$

and letting

$$C = \frac{\varepsilon a h E_a}{2\pi} \frac{e^{-jkr}}{r} \tag{B.45}$$

leaves

$$F_\phi = -C \int_{\phi-0}^{\phi-2\pi} \cos\phi'' \cos n(\phi - \phi'') e^{jka \sin\theta \cos\phi''} \, d\phi'' \tag{B.46}$$

Using another change of variables

$$\phi''' = -\phi'' \tag{B.47}$$

$$d\phi''' = -d\phi'' \tag{B.48}$$

leaves

$$F_\phi = C \int_0^{2\pi} \cos\phi'''(\cos n\phi''' \cos n\phi - \sin n\phi''' \sin n\phi) e^{jka \sin\theta \cos\phi'''} \, d\phi''' \tag{B.49}$$

The second term of the integral has a value of zero due to the multiplication of odd and even functions, leaving

$$F_\phi = C \int_0^{\pi} \cos\phi''' \cos n\phi''' \cos n\phi e^{jka \sin\theta \cos\phi'''} \, d\phi''' \tag{B.50}$$

$$F_\phi = C \frac{\cos n\phi}{2} \int_0^{2\pi} (\cos(n-1)\phi''' + \cos(n+1)\phi''') e^{jka \sin\theta \cos\phi''} \, d\phi'' \tag{B.51}$$

After using the following relationships in Equations B.23 and B.24

$$F_\phi = j^{n-1} \varepsilon a h \frac{E_a}{2} \frac{e^{-jkr}}{r} (J_{n-1}(ka \sin\theta) - J_{n+1}(ka \sin\theta)) \cos n\phi \tag{B.52}$$

Bibliography

[1] Taylor, John W.R, *Janes Pocket Book of RPVs: Robot Aircraft Today*, MacDonald and Janes Publishers Limited, London, 1977.

[2] Flinn, E., and A. Smith, *RPV/Drones/Targets Worldwide Market Study & Forecast*, Defence Marketing Services, 1984.

[3] Carver, K.R., and J.W. Mink, *Microstrip Antenna Technology*, IEEE Transactions on Antennas and Propogation, Vol. AP-29, No. 1, pp. 2–24, Jan. 1981.

[4] Deschamps, G.A., *Microstrip Microwave Antennas*, presented at the 3rd USAF Symp. on Antennas, 1953.

[5] Gutton, H., and G. Baissinot, *Flat Aerial for Ultra High Frequencies*, French Patent No. 703113, 1955.

[6] Munson, R.E., *Single Slot Cavity Antennas Assembly*, U.S. Patent No. 3713162, Jan. 23, 1973.

[7] Munson, R.E., *Conformal Microstrip Antennas and Microstrip Phased Arrays*, IEEE Transactions on Antennas and Propagation, Vol. AP-22, No. 1, pp. 74–77, Jan. 1974.

[8] Sanford, G.S., *Conformal Microstrip Phased Array for Aircraft Tests with ATS-6*, IEEE Transactions on Antennas and Propagation, Vol. AP-26,

No. 5, pp. 642–646, Sept. 1978.

[9] Yee, J.S., and W.J. Furlong, *An Extremely Lightweight Fuselage-Integrated Phased Array For Airborne Applications*, Proceedings of the Workshop on Printed Circuit Antenna Technology, Oct. 17–19, 1979, New Mexico State University, pp. 15.1–15.12.

[10] Murphy, L.R., *SEASAT and SIR-A Microstrip Antennas*, Proceedings of the Workshop on Printed Circuit Antenna Technology, Oct. 17–19, 1979, New Mexico State University, pp. 18.1–18.20.

[11] Shafai, L., and G. Kumar, *Microstrip Antennas as a Candidate for MSAT Vehicular Application*, TR84-1, Department of Electrical Engineering, University of Manitoba, May 1984.

[12] Shafai, L., A. Bhattacharyya, G. Kumar, and B. Tabachnik, *Performance of Planar Microstrip Arrays Including Mutual Coupling "MSAT Application"*, TR87-1, Department of Electrical Engineering, University of Manitoba, Jan. 1, 1987.

[13] Bahl, I.J., and P. Bhartia, *Microstrip Antennas*, Dedham: Artech House, 1982.

[14] Foster, P.R., and N. Williams, *Antennas for RPV's Final Report Pt.1: Literature Survey and Review*, RF Technology Centre, Electrical Research Association, Leatherhead, Surrey, June 1978.

[15] Myint-U, T., *Partial Differential Equations of Mathematical Physics*, New York: North-Holland, 1980.

[16] Balanis, C.A., *Antenna Theory Analysis and Design*, New York: Harper & Row, Publishers, Inc, 1982.

[17] Elliot, R.S., *Antenna Theory and Design*, New Jersey: Prentice-Hall, Inc., 1981.

[18] Milligan, T.A., *Modern Antenna Design*, New York: McGraw-Hill Book Company, 1985.

[19] Antoszkiewicz, K., L. Shafai, and E. Bridges, *Impedance Characteristics of Circular Microstrip Patches*, ANTEM Conference Proceedings, August 10–12, 1988, Winnipeg.

[20] Harrington, R.F., *Time-Harmonic Electromagnetic Fields*, New York: McGraw-Hill Book Company, 1987.

[21] Kraus, J.D., *Electromagnetics*, London: McGraw-Hill International Book Company, 1984.

[22] Abramowitz, M., I.A. Stegun. *Handbook of Mathematical Functions with Formulas, Graphs, and Mathematical Tables*, New York: Dover Publications, Inc., 1965.

[23] Shen, L.C., *The Elliptical Microstrip Antenna with Circular Polarization*, IEEE Transactions on Antennas and Propogation, Vol. AP-29, No. 1, pp. 90–94, Jan. 1981.